Process Engineering, Characterization and Self-Healing Assessment of Toughened Calcium Phosphate Silicate Composite Bone Cements

by

Azadeh Goudarzi

A THESIS SUBMITTED IN PARTIAL FULFILLMENT OF

THE REQUIREMENTS FOR THE DEGREE OF

Doctor of Philosophy

in

The Faculty of Graduate Studies

(Materials Engineering)

THE UNIVERSITY OF BRITISH COLUMBIA

(Vancouver)

December 2013

Abstract

Self-healing, the ability to repair defects without external assistance, is one of the most magnificent characteristics of natural tissues. Achieving similar characteristics in biomaterials substituting natural tissues is highly desirable. As ceramic bone cements are designed to substitute bone tissues, the knowledge of their self-healing processes and characteristics is of vital importance for the advancement of bioceramics in orthopedic applications. In this work we have studied self-healing mechanisms of polyvinyl alcohol (PVA) fiber toughened Tri-Calcium Silicate (C_3S) cements, with and without calcium phosphate additions. The C_3S-PVA samples were partially fractured in three-point-bending, and then soaked in Simulated Body Fluid (SBF) for 7 days at 37°C. The variations in the morphology and width of the healed cracks were tracked by optical and electron microscopy. Chemical composition and phase analysis were determined using EDX, XRD and FTIR. The energy absorbed before the failure of C_3S-PVA samples, determined through the area under load-displacement curves, was nearly two orders of magnitudes higher than the pure C_3S samples. Most of the cracks in the previously fractured C_3S-PVA samples soaked in SBF were visually eliminated in 7 days, also resulting in partial restoration of their load-carrying capacity. Based on the EDX, XRD and FTIR results, a healing mechanism was proposed, including preferential precipitation of calcium phosphates and calcium carbonate phases within the cracks. The same healing treatment was applied to the new composite cement, wherein the C_3S matrix included 10wt% of Mono Calcium Phosphate (MCP) for improved cement biocompatibility and bioactivity. The toughness of C_3S-10MCP-PVA samples was also almost two orders of magnitudes higher than the pure C_3S-10MCP. C_3S-10MCP-PVA samples had higher damage tolerance (deflection at maximum load) than C_3S-PVA samples. Self-healing studies of the C_3S-10MCP-PVA showed better restoration of the load-

carrying capacity than C_3S-PVA. Such evidence emphasizes the effective role of calcium phosphate in the healing process of the toughened bioceramic cements. While such successful SBF-induced healing does not guarantee similar mechanisms operating *in vivo*, this pioneering research opens up avenues for further improvements of the cementitious ceramic composites in medical applications, as well as in broader engineering applications, e.g. in construction industry.

Preface

This dissertation is original, unpublished, and independent work by the author. None of the text is taken directly from previously published articles. -A. Goudarzi.

Table of Contents

List of Tables

List of Figures

Lists of Abbreviations

C_3S Tricalcium Silicate - $3CaO.SiO_2$

C_2S Dicalcium Silicate $2CaO.SiO_2$

CSC Calcium Silicate Cement

CPC Calcium Phosphate Cement

CaP Calcium Phosphate

MCP Mono Calcium Phosphate anhydrite - $Ca(H_2PO_4)_2.H_2O$

CPSC Calcium Phosphate Silicate Cement

ECC Engineered Cementious Composite

SBF Simulated Body Fluid

XRD X-Ray Diffraction

SEM Scanning Electron Microscopy

PVA Poly Vinyl Alcohol

FTIR Fourier transform infrared

HA Hydroxyapatite

PMMA Poly Methyl Meta Acrylate - IUPAC name: Poly(methyl 2-methylpropenoate)

Acknowledgments

I offer my enduring gratitude to the faculty, staff at the materials engineering department of UBC, who have been helpful, considerate and kind to me, specially Michelle Tierney, Mary Jansepar, and Fiona Webster. I highly appreciate my dear supervisory committee: Dr. Rizhi Wang, Dr. Goran Fernuld and Dr. Frank Ko for their time and interest in my project. I owe particular thanks to my kind supervisor, Dr. Tom Troczynski, whose great knowledge and experience taught me how to change my point of view in research, question more deeply and find coherent answers. He showed me how great a teacher can be and I hope I can use his example someday. I thank Dr. Dorin Ruse for letting me use his lab facilities, and his thoughtful insights. Many thanks are owed to my dear colleagues: Shuxin Zhou, Taesik Chae, Rahul Lodha, Matteo Pernechele for their advices and help. Very special thanks to my dear friends in the office Hamidreza Zargar, Ali Shafei and Carmen Oprea for outstanding kindness and support. I thank Nasim Sahraei, Nazanin Shaebani, Arian Amirkeyvan, Leyla Farhang, Nina Rajabinasab, Nasim Bakhshizadeh, Fatemeh Soltani for their friendship, and their advices on refworks, softwares, solid state physics, and characterization. Sahar Edelkhani, Shadi Taghavi and Fahime Sheikhzadeh, my lovely friends: without your extensive support, love and patience finishing this dissertation was impossible. Superior appreciations are owed to my love and dearest friend, Pooya Jaferain, for technical computer support, extensive proof readings, and extreme kindness and positive energy.

I owe everything I do and I am to my beloved family. Many thanks for their understanding, patience and love throughout my years of education; in the last few years, although they have been physically distant, but much closer in heart to me.

Dedication

To my Dad Hassan and my Mom Tooran:

Hearing your voice from thousands of miles away, feeling your unconditional love and faith, always kept me going. I'm so lucky and proud to be your daughter. Everything I am and I have is because of you.

To my love, Pooya:

You made me a stronger version of me and brightened my dreams. Your patience and love was the backbone of this dissertation.

1. Introduction

Defects can occur in natural material structures and alter their performance. Natural materials can repair the defects with a self-assembly process. They use available substances around them such as CO_2, water, minerals from soil, amino acids from their diet etc. to heal themselves, which makes them "maintenance-free". Some examples of such systems are: a) Biological regeneration of limbs, such as salamander's ability to reproduce its tail or limb after amputation [1]; b) Tissue regeneration, such as repair of the skin after cutting or healing of a cracked bone after falling. However even biological self-healing is limited, for example in human beings biological regeneration of a limb is not possible or if the bone defect is too large, the body cannot repair it by itself.

Similar self-healing properties are of great fundamental interest in any engineered structure. In construction industry, several studies suggested the possibility of self-healing of Engineered Cementitious Composite (ECC) [2-10]. ECCs can repair micro-cracks in their structures, without any external assistant and through intrinsic properties of the composite matrix, which mainly consists of Tri-Calcium Silicate (C_3S). The applications of such systems in construction industry include coupling beams in high-rise buildings, bridge deck link slabs, and repair materials for damaged dams [11,12]. The urge to mimic self-healing for biomaterials increases, as they are to substitute natural materials. Failure of a biomaterial would lead to the patient's revision surgery and in some cases, death. Therefore, the ability of any biomaterial to self-heal defects in its structure is of great practical importance. A paste-like biomaterial, which can be fitted into complicated shapes of bone defects and consequently become solid, is called 'Bone Cement'. It can be used either for fixation of a metallic implant or as a filler for small bone defects and

sometimes in minimally invasive surgeries as an injectable paste. Self-healing of bone cements has been studied for a specific type of the bone cement, poly-methyl meta-acrylate (PMMA) [13]. The results were not promising, as the encapsulated healing agents consisted of polymer monomers/initiators. This increased complications associated with monomer release from the PMMA bone cements [14]. There are no reports on studying self-healing of non-PMMA bone cements, in particular bioceramic cements, to our best knowledge.

C_3S has been studied as a possible bone substitute and bone cement. Its bioactivity has been shown by *in vitro* tests [15,16], which indicates it will produce Hydroxyapatite (HA) on its surface upon soaking in Simulated Body Fluid (SBF)[17]. We therefore hypothesized the possibility of self-healing ability of the C_3S based cements in SBF environment through HA deposition in damaged cement (within cracks). As C_3S is a brittle material, upon load exceeding failure limit, the material is catastrophically fragmented, which eliminates any possibility of studying the self-healing within cracked specimen. Thus, Poly Vinyl Alcohol (PVA) microfibers were used to increase C_3S toughness and stabilize the cracks. PVA fibers form chemical bond with the cementitious materials, due to the presence of hydroxyl groups in their molecular structure [4] and provide significant toughening of the composite. We hypothesised that the stable cracks would cause the un-hydrated portion of the C_3S particles (available homogeneously throughout the bulk of the sample) become accessible to SBF, which consequently induce HA precipitation within the cracks. Therefore, healing ability of such composite in SBF should be accelerated by addition of the HA precipitation mechanism inside of the cracks. To validate such hypothesis of self-healing, microstructural and load-bearing capability analyses are performed.

2. Literature Review

2.1. Bone problems and necessity for bone cements

Bone diseases and trauma can result in partial or total disability of the patient and increase the risk of damage to the internal parts of the body such as the brain, heart and spinal cord. Osteoporosis is the most prevalent bone disease [18], causing osteoporosis-induced fractures (OIF) by lowering the density, and thus the mechanical strength of the bones. A prevalent type of OIF is vertebral fracture, which approximately has 700,000 new cases per year in the United States [19]. Naturally, bones have self-healing ability, unless the defect is relatively large (e.g. due to crash trauma), or the patient body is not performing on its natural basis (elderly people or specific diseases). In order to accelerate the healing process or simply to replace the function of the bone tissue, replacing material is required. Materials used in bone site to augment or replace the function of the tissue are called bone grafts [20]. The use of natural bone grafts involves some issues. An autograft (a tissue from one part of the body implanted to the other part) requires double surgery and the available tissue is limited and may contain the same disease [21]. Allografts (e.g. from a human to a human) and heterografts (e.g. from an animal to a human) have issues such as: sterility, disease transfer, and possible genetic interactions [22]. Therefore, often a synthetic material is selected as an alternative bone graft or bone substitute. Among synthetic bone grafts, many types of engineering materials have been used. A paste-like material to substitute bone tissues and become solid/rigid afterward, was introduced more than a century before. It was named “bone cement” later. A brief history and review of the bone cements can be found in the next chapter.

2.2. Bone cements

2.2.1. History and types of bone cements

In 1891 Gluck used a paste-like material as a filler for bone defects [23] followed in 1892 [24] by fabrication of Plaster of Paris, calcium sulphate semi-hydrate ($CaSO_4.1/2H_2O$), which sets when combined with water to form calcium sulphate di-hydrate ($CaSO_4 \times 2H_2O$). However, the name "bone cement" was first given to Poly Methyl Methacrylate paste (PMMA – IUPAC name: Poly(methyl 2-methylpropenoate), chemical formula: $(C_5O_2H_8)_n$), which was used in 1959 by Sir John Charnley to fix a metallic implant in hip replacement surgery. This was a revolution in hip surgery, and five years later clinical reports on 455 patients using PMMA cement in their hip and knee surgeries was published [25].

Bone cements were found to act as easy handling, "finger fitted" pastes to fill small bone defects. The shapes of the small bone defects are typically irregular and different from person to person (like in vertebrae, maxillofacial bones, etc.). Therefore, shape adaptive cement filling is a viable and effective solution to address these problems [26]. Bone cements generally are divided into the three major categories: i) PMMA and polymer based cements; ii) Calcium-based bone cements (calcium phosphate, sulphate, silicate, etc.); iii) Other bone cements (composites, bioglass, glass ionomer and magnesium based bone cements) [26,27].

PMMA cements have been extensively used since 1959 to fix metallic implants. In 1987 Galibert and Deramond used PMMA cement into a fractured vertebral body to stabilize and relief pain [28]. This was a breakthrough for the patients with osteoporosis induced vertebra fractures to skip surgery with its all well-known risks and draw backs, specifically total body anaesthesia. This procedure is a minimally invasive surgery and is called percutaneous

Vertebroplasty (VP). Similar procedure, in which an inflatable balloon is applied prior to cement injection to restore the height of the crushed vertebra, is called Kyphoplasty (KP). However, PMMA have some limitations and complications such as exothermic setting reaction, toxic monomer release [29]. These drawbacks are affecting the success rate of VP and KP procedures, as mentioned by Lewis [30]. He compiled the optimum required properties of a bone cement to assure the best results in VP and/or KP [30]. The most important factors are the optimum biological and mechanical properties of the cements, i.e. mechanical properties (such as stiffness, strength and fracture toughness) should be as close as possible to the natural bone in the implanted bone site. In the following sections, the mechanical and biological requirements of bone cements will be reviewed.

2.2.2. Requirements of a bone cement

2.2.2.1. Mechanical Requirements

The mechanical properties of bone have been reviewed in Table 2-1 [20]. Since bone is "the intended tissue" to be repaired or augmented [31], the cement should mimic the mechanical properties of the replacing bone as closely as possible. In engineering structures, most concern is to exceed the minimum required load bearing capacity, but for the bone systems it is important to be within the required range, not too weak to fail during the performance of the bone substitute; not too stiff to cause stress shielding (the biomaterial will be responsible for the greater portion of the load, leaving the remaining or adjunct natural bone tissues stress-free or stress-deficient). During bone remodelling, activation of osteobalsts and osteoclasts are directly induced by external mechanical loads. Huiskes et. al. have reported both "*the frequency and the amplitude*" of the external loads are necessary to stimulate bone cells activation [32]. Therefore it is

important to avoid stress shielding, which is caused by application of materials with much higher stiffness than the bone.

There are three mechanical requirements for acrylic bone cements as described by Lee [33] and ISO Standard 5833 (2002): Minimum compressive strength of 70 MPa and bending modulus (stiffness) of 1.8 GPa and bending strength of 50 MPa. Strength is tested on cylindrical samples of bone cement after 24 hours of forming and storage in dry air [33,34]. Permanent bone cements such as PMMA remain in the body for long period of time, e.g. clinical experiences of more than thirty years been reported [33]. Therefore, long-term mechanical properties including creep and fatigue behaviour, are also important. Fracture toughness indicates the resistance to crack growth in materials and is a suitable parameter to assess functional performance of the cement. Wang and Pilliar [35] compared and reported fracture toughness of two commercial acrylic bone cements. They showed K_{IC} of Simplex-P varies between 1.01-1.26 MPa√m depending on the preparation method, while Zimmer LVC varies between 0.98-1.03 MPa√m. These values decrease by aging the cement for 60 days. Table 2-2 reviews typical mechanical properties of some commercial bone cements.

Table 2-1- Mechanical properties of bone[1] [20,27,36].

	Tensile Strength	Compressive Strength	Flexural Strength	Young's Modules	K_{IC}	Strain to failure
Bone type	MPa	MPa	MPa	GPa	MPa√m	%
Cortical	50-150	170-230	100-225	7-30	2-12	1-3
Cancellous	10-20	7-10	4.5	0.05-0.5	NA	5-7

Table 2-2- Mechanical properties of typical commercial bone cements [30,33-35].

	Compressive Strength	Flexural Strength	Young's Modules	K_{IC}
Bone cement type	MPa	MPa	GPa	MPa√m
Sipmlex	67.7-96.1	72.6	2.2-2.6	0.88-1.6
Norian®SRC	50	0.47	NA	0.06–0.14
BoneSource™	26	NA	NA	NA
Cortoss	210	NA	NA	NA
Bis-GMA reinforced with Sr-HAp	139.6	9.3	2.2	NA
Palacos	73.6-100.3	NA	2.3-2.8	NA

2.2.2.2. Biological requirements

The combination of non-toxicity, osteoconductivity, osteoinductivity, biocompatibility and bioactivity are considered as a set of desirable biological properties for biomaterials [37-39]. To unify the terminologies, Table 2-3 shows a brief definition of these terms. Biocompatibility testing protocols are designed by professional and regulatory organizations[2]. Biocompatibility and osteoconductivity are usually assessed simultaneously by *in vitro* osteoblast cell culture. Biocompatibility is evaluated using different methods and protocols such as SEM imaging with

[1] –Complications in reporting mechanical properties of the bone. Testing whole bone or beam, one simple osteon, preparing the test specimen, dry or wet measurement, in addition to the bone density, age, degree of mineralization

[2] - American Society for Testing and Materials (ASTM), the American Dental Association (ADA), the International Standards Organization (ISO), the National Institutes of Health (NIH), and the Food and Drug Administration (FDA), Health Canada (HI).

trypan blue protocol and MTT assay [20]. However, the assessment of the material/tissue interaction is more accurate by *in vivo* tests. Cells behave differently *in vivo* due to the presence of "*other cell types, numerous cell signaling factors, the extracellular matrix and physiological differences"* in mechanical stress and blood flow [20]. For *in vitro* tests, the cell type should be carefully selected to form a meaningful relation to the *in vivo* test results [20]. There are two methods to evaluate osteoinductivity: (1) un-differentiated cell culture i.e. stem cells, and (2) implantation of the cement in a non-skeletal site to study the formation of the bone tissue (e.g. intramuscular implantation of brushite and monetite by Habibovic et. al. demonstrated that they are both osteoinductive [20]).

Table 2-3- Definitions of biomaterials and biological properties of bone substitutes.

Term	Definition
Biomaterial	"Any material or combination of materials used to replace, augment, or restore function of damaged or diseased tissues" [3] [40]
Biocompatibility	Biological performance (interaction between materials and living system) in a specific application that is judged suitable for that situation [38]
Osteoconductivity	Able to induce new bone formation in skeletal sites [31]
Osteoinductivity	Able to induce new bone formation in extra skeletal sites [31]
Bioactivity	Ability to have direct bonding with living tissue

[3] - Biomaterials are considered as a sub-part of medical devices by the definition of a medical device in FDA:
"an instrument, apparatus, implement, machine, contrivance, implant, *in vitro* reagent, or other similar or related article, including a component part, or accessory which is (1) intended for use in the diagnosis of disease or other conditions, or in the cure, mitigation, treatment, or prevention of disease, in man or other animals, or
(2) intended to affect the structure or any function of the body of man or other animals, and which does not achieve any of its primary intended purposes through chemical action within or on the body of man or other animals and which is not dependent upon being metabolized for the achievement of any of its primary intended purposes" [53]

"Bioactivity" of a material is often associated with the formation of Hydroxyapatite (HA) on its surface when submerged in Simulated Body Fluid (SBF) [15,41-44]. The concept of evaluating bioactivity by this method was first suggested by Kokubo et. al. in 1991 [45]. If a layer of HA formed on the surface of a material, then it could bond with bone cells in the body and would thus be declared "bioactive" [17]. Despite some ambiguity surrounding this evaluation of bioactivity, its simplicity has led to its extensive use and the method [17]. Later, Bohner and Lemaitr reported some false negative and false positives conclusions compared with the *in vivo* results, indicating that this simple method is not sufficient to describe a material as bioactive [46]. Pan et. al. stated that bioactivity tests are only "*viable to test using osteoblasts, whether in vivo or in vitro*" [47]. However, bioactivity is still widely evaluated by the evidence of HA formation in the SBF [43,48,49].

Evaluation of biological properties of PMMA can be related to a long time ago, when the PMMA cockpit windshields shattered in World War II; the pilots who carried PMMA shrapnels in their bodies unknowingly took part in the first *in vivo* experiments [26]. However, when the polymer is polymerized in-situ, the generated heat of the reaction can lead to "*protein denaturation, cell necrosis and nerve ablation*", which may partially explain the pain relief after vertebroplasty [14]. Although PMMA is bioinert, its monomer MMA ($CH_2=C(CH_3)COOCH_3$) is neither inert nor biocompatible; it is rather toxic. Even inhalation of MMA monomers by medical personnel in high amounts can cause "*liver necrosis, pulmonary edema, pulmonary emphysema, interalveolar congestion and hemorrhage*" [29]. Exposure to low levels of MMA vapor can cause less dramatic effects such as nausea, lack of appetite, potential allergenic sensitization, local reactions with skin, chronic cough, and increased airway resistance [29,50]. MMA monomer was "constantly found in blood samples" taken during hip replacement surgery.

Released MMA in the circulation system may cause some adverse general reaction [50]. There are reports of passing fat emboli, which was entrapped in the lungs after Vertebroplasty. It is hypothesized to be the result of "*stimulation of the sensory nerve endings by the MMA monomer*" [50]. However, despite all these negative effects, PMMA-based bone cements are still in widespread and almost exclusive use in medicine.

Alternatively, the second most commonly used type of bone cements, Calcium Phosphate Cements (CPC) or more precisely, Calcium Orthophosphates, are highly bioactive, osteoconductive, osteoinductive due to their chemistry and crystal structure [51]. CPCs are made up with the same ions of natural bone mineral phase. Most of them form bonelike apatite on their surfaces after implantation, which is implied to suggest their bioactivity and the ability to bond directly to the bone cells on bone sites [17]. Apatite layer has some specific characteristics; its spatial orientation of calcium ions is complementary to calcium ions in the structure of osteocalcin, which is the bone's most abundant non-collagenous protein. It has the ability to bind to hydroxyapatite and function in cell signaling and activation of osteoclasts and osteoblasts. Hoang et. al. have hypothesized that Osteocalcin's "*negatively charged surface coordinates five calcium ions*" would fit to the HAp crystal structure [52]. Based on the final product of the cement after setting reaction, there are two main types of CPCs: apatitic and brushite. Nakano et. al. have published a paper on clinical application of CPC to vertebroplasty on 86 patients in two groups: i) osteoporotic burst fracture or pseudoarthrosis; ii) osteoporotic compression fractures. They used an apatitic CPC (Biopex) [53] and showed very good results obtained up to two years follow-up. However, the chemical and structural similarity advantages of CPC are balanced by their insufficient mechanical properties (see Table 2-2).

In Summary, PMMA cements generate heat during polymerization, which could cause tissue necrosis, release toxic monomers and decrease mechanical properties in long-term applications. Calcium phosphate bone cements with good biological properties have insufficient mechanical properties, specifically low fracture toughness. Much research is ongoing to address these limitations in CPCs [21,54,55]. Canal et. al published a review paper on fiber reinforced CPCs (refer to section 2.4.2) [56]. However, further research is required to address such limitations and complications. In the next section, another type of bone cement is reviewed that recently has become attractive: Calcium Silicate Cement (CSC) and combination of CSC and calcium phosphates, or Calcium Phosphate Silicate Cement (CPSC).

2.3. Review of calcium silicate based composite cements

There are two types of calcium silicate based composites reviewed in this Section: i) Calcium Silicate Cement (CSC); ii) Calcium Phosphate Silicate Cement (CPSC).

2.3.1. Calcium silicate cement

One of the first calcium silicates cements (CSC) introduced as biomaterial was Mineral Trioxide Aggregate (MTA), a mixture of Di-Calcium Silicate (C_2S) and Tri-Calcium Silicate (C_3S), bismuth oxide, and trace amounts of other oxides [42,57-59]. The calcium silicates react with water and produce Calcium Silicate Hydrate (C-S-H) gel and calcium hydroxide. MTA cements have compressive strength of 45 MPa after setting for 24 hours, which increases to 70 MPa after 28 days. However, MTA has some limitation in root canal therapy applications, such as very slow hydration and setting rate (e.g. initial setting time of 40-70 min and final setting time of 140-175 min) [60]. MTA was first introduced in 1993 [61] and five years later became FDA-approved for clinical endodontic use [58]. MTA produces a high pH environment (approximately 12) after setting, which gives an antibacterial effect to the cement in endodontic

applications [58]. However, recently two review papers have published some complications related to MTA applications due to its long-term maintenance of high pH [62,63]. There are other types of root canal sealers, most of them based on calcium silicates, which are in the market or currently undergoing clinical assessments (AH plus, iRoot SP, EndoSequence BC Sealer) [64-66].

A fundamental advantage of CSC relates to the positive effect of Si ion in promoting bone growth and osteogenesis (as also found in Bioglass ceramics) [67-70]. However some studies suggest that the high concentration of Si might show toxic effects [71]. Shie et. al. reported that the presence of Si in certain concentration (2 and 4 mM) enhances osteoblast activity, but at high concentrations (>4 mM) can cause decrease in cell proliferation. An appropriate Si ion concentration (e.g. 4 mM), promoted osteoblast proliferation in three hours and did not lead to death of the cells [71]. They claim their results are aligned with Keeting et. al. findings [72], in which they show Si containing solutions are "mitogenic for bone cells" [72].

In 2005, Chang et. al. reported bioactivity of a beta-dicalcium silicate/poly(d,l-lactic acid) scaffold [73]. Their results also indicated that addition of C_2S increased the hydrophilicity of the PLLA composite [73]. Later, the same group published a paper on promising properties of C_3S as an injectable bone cement [74]. They predicted that stimulation of cell proliferation and gene expression by C_3S is possible. The compressive strength of this cement is reported as 6.4 MPa and 20.2 MPa after two and 28 days of setting, respectively [74]. The other advantage of C_3S is better injectability, since it does not have any filter pressing effect during extruding out of the syringe [74]. Later, they showed that the osteoblast-like cell attachment and proliferation on the surface of calcium silicate ($CaSiO_2$) is better than β-TCP. They have concluded that silicon might be important for "*bone metabolism*" [75]. Zhao et. al. also studied the biodegradation of

C_3S and reported that it will degrade much faster than HAp. They have showed osteoblast-like cell proliferation on C_3S [15], although "further *in vivo* studies" are required to guarantee the application of this ceramics [15]. C_3S is the main component of the Portland cement and MTA. The hydration process of C_3S is a classical reaction and has been well known for decades [76]:

$Ca_3SiO_5 + zH_2O \rightarrow CaxSi(OH)y.nH_2O(C\text{-}S\text{-}H) + (3\text{-}x)\ Ca(OH)_2$ Equation 2-1 [76]

$3Cao.SiO_2 + (3+m\text{-}n)H_2O \rightarrow nCaO.SiO_2.mH_2O$ (C-S-H gel) + $(3\text{-}n)\ Ca(OH)_2$ Equation 2-2 [77]

The hydration reaction of C_3S results in formation of C-S-H gel and $Ca(OH)_2$. Zhao et. al. suggested that C_3S paste and its hydration product are bioactive and C-S-H gel, is "dissolvable in SBF" [74], although no quantitative data were provided. Combination of C_3S with other materials has been studied, such as anti-washout chitosan and C_3S composite [48] and C_3S-calcium carbonate [78].

2.3.2. Calcium phosphate silicate cement

Calcium Phosphate Silicate Cement (CPSC) is any combination of calcium silicates and calcium phosphates; the matrix (or the continuous phase) of such cement can be either CPC or CSC. One of the examples of CPSCs is the combination of C_3S and Mono Calcium Phosphate Monohydrate (MCPM) [79] or C_3S and calcium phosphate monobasic (anhydride) [80]. The rationale behind adding Calcium Phosphate (CaP) to C_3S is: i) calcium phosphates are known for their biological properties due to sharing the same ions as the natural bone. Zhou et .al. showed higher biocompatibility of CPCSs than CSCs [81]; ii) the thermodynamics of calcium phosphates [82-85] states the most stable form of CaP in pH>6.5 in room temperature is HAp; Therefore, if a CaP phase is present in high pH environment, it will transform into HAp (if kinetics allow). If the Ca/P ratio of the CaP is lower than the ratio of HAp (wherein Ca/P=1.67), it will react with

the $Ca(OH)_2$ to produce HAp. In C_3S hydration, calcium hydroxide is a hydration by-product and produces high pH>12 environment in contact with aqueous solutions [76].

Hydration products of C_3S are C-S-H and $Ca(OH)_2$. C-S-H is the strengthening phase or "*the main 'glue' that holds concrete together*" [86], and is composed of nano-sized solid-phase and nano-sized pores [63]. On the other hand, $Ca(OH)_2$ is the weak by-product of the reaction and is responsible for pH increase during and after cement setting. By adding a new phase to the system, i.e. Calcium Phosphate Monobasic (MCP, $3Ca(H_2PO_4)_2$), theoretically, some of the $Ca(OH)_2$ should react with calcium phosphate to produce HAp and water. Huang and Chang [79] investigated the hydration of C_3S to C-S-H gel in the presence of Calcium Phosphate Monobasic Monohydrate (MCPM). They have suggested the following reactions [62]:

$$3Ca(H_2PO_4)_2.H_2O + 3Ca(OH)_2 \rightarrow 6CaHPO_4.2H_2O + 3H_2O \qquad \text{Equation 2-3}$$

$$6CaHPO_4.2H_2O + 3Ca(OH)_2 \rightarrow Ca_{10}(PO_4)_6.(OH)_2 + 18H_2O \qquad \text{Equation 2-4}$$

As the reaction progresses, it is producing 18 water molecules per six $Ca(OH)_2$ molecules. Release of water molecules in Equation 2-4 can further progress the reactions in Equations 2-1 or Equation 2-2. This could be of paramount significance for cements, which set within environment poor in water, e.g. in confined spaces such as dental root canals.

Huang and Chang work indicates that the composite CPSC has the ability to bond to bone tissue *in vivo*. However, to confirm the hypothesis further *in vivo* studies are required [79]. Recently they have directly used brushite ($CaHPO_4.2H_2O$) instead of MCPM to precede one step forward towards the *in situ* formation of HAp in the composite cement [87]. Li et. al. reported a novel calcium silicate/calcium phosphate (HAp, TCP) composite cement [88]. In this cement, chitosan in the liquid phase was used to increase the injectability, 3.8 wt% PVA to enhance the

initial strength, and 19 wt% mannitol as porogen[4]. They have shown their cement is degradable and bioactive in the SBF [88].

Ding et. al. described the use of a sol-gel method to produce C_3S. Then, they added brushite as the second phase [39]. Their results showed that the simultaneous formation of apatite and C-H-S reduced the setting time to few minutes and enhanced the osteoconductivity, which was revealed by osteoblastic gene sequence studies [39]. Other examples of CPSCs are commercial dental cements, including premixed calcium phosphate silicate‑based sealer EndoSequence BC Sealer and iRoot SP [64-66].

In construction industry CPSCs are not available. However, Naus et. al. investigated the adverse effects of the phosphates in the concrete degradation to evaluate if there ought to be a limit to the maximum allowable phosphate concentration in the regulatory system auditions. They concluded that there is no adverse degradation effect from phosphate salts, based on studies on concrete infrastructures [89].

2.4. Fiber reinforcement of calcium silicate/calcium phosphate cements

2.4.1. Fiber-reinforced ceramic composites

Fiber reinforcement is a conventional method to increase fracture toughness of materials, especially ceramic matrix composites. Kim and Mai [90] have mentioned that every system in a fiber-reinforced composites has its own and "unique" properties. These properties largely depend on the fiber-matrix interactions, in particular bonding. Fiber-matrix interface bonding can be formed by: (i) molecular interactions; (ii) electrostatic attraction; (iii) inter-diffusion of elements; (iv) chemical reactions; (v) mechanical interlocking. For ceramic matrix composites, usually the

[4] - Combination of the two words: Porosity - Generator

toughening mechanism is mechanical interlocking. Therefore surface treatment of the fibers to modify the surface roughness is an important improvement measure [90]. In general, incorporation of the short fibers into a brittle matrix can increase the composite's fracture toughness by several different mechanisms [90]. Four principle mechanisms of toughening as schematically illustrated in the Figure 2-1 include: (i) fiber bridging; (ii) fiber pull-out; (iii) crack deflection; (iv) Microcracking. Mostly, more than one mechanism is operative, but usually only one mechanism dominates, depending on the matrix-fiber interfacial properties [91]. The important factors to influence effectiveness of fiber-reinforcement in improving toughness of the composite are: i) amount of fibers; ii) fiber-matrix bond; iii) homogenous dispersion of the fibers in the matrix [90]. Figure 2-2 shows different behaviour of cements according to their stress-strain characteristics.

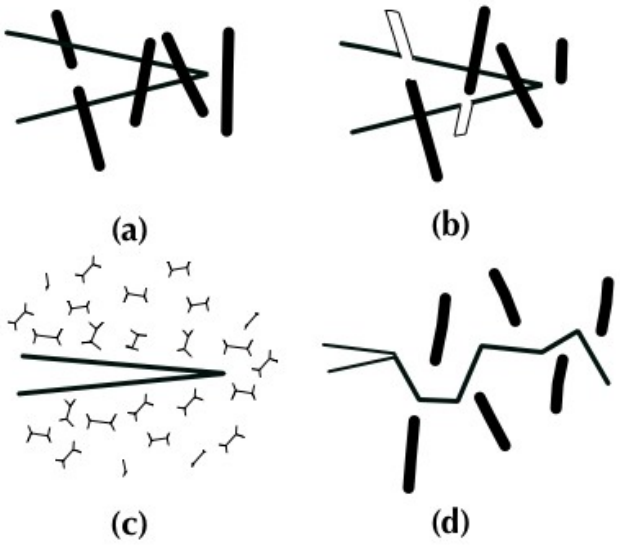

Figure 2-1- Toughening mechanisms of fiber reinforced ceramic matrix composites (a) fiber bridging; (b) fiber pull out; (c) microcracking; (d) crack deflection (with kind permission from Springer) [91].

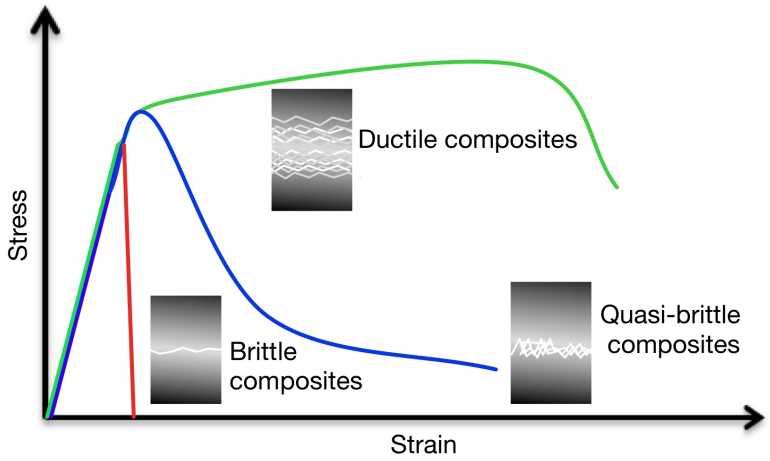

Figure 2-2- Typical stress-strain curves for brittle cement (e.g. CPC) and fiber reinforced cementitious composites showing either quasi-brittle (tension softening) or ductile (strain hardening behaviour), redrawn from [90].

2.4.2. Fiber reinforced CPCs

CPCs fracture toughness is significantly lower than PMMA (i.e. < 0.2 MPa√m compared to 0.8-1.6 MPa√m for PMMA). To address this problem, Chow [92] used Chitosan for forming non-rigid elastomeric CPC matrices. By incorporating chitosan lactate (up to 20 wt%) into CPC, the strength increased four to six times, and work-of-fracture (toughness) increased by an order of magnitude [92]. Gorst et. al. have used resorbable sutures (polyglactin fibre, d= 0.30–0.349 mm) in a brushite cement to improve its flexural strength and maximize fiber-matrix interfacial interactions. In addition, resorbable suture degraded in the body and produced interconnected porosity [93]. Santos et. al. used Poly-amide fibers (Nylon66, 0.1 mm diameter) in α-TCP matrix; they reported that the fibers did not have "good" bonding with the matrix [94]. Due to recent progress and success in the fiber reinforced CPC in load bearing applications *in vivo*, Krüger and Groll [95] in their review paper suggest the promising future for such research. They have also mentioned: "degradability is generally aimed for the composites", based on the

characteristics of the CPCs. However, in patients with less capability for bone regeneration, such as elderly patients with osteoporosis, the use of non/slowly resorbable cements can be justified. Table 2-4 presents some of the fiber reinforcements used in the CPC matrix.

Table 2-4- Fiber reinforced CPCs (adapted from [56,95]).

Fiber Type	**Fiber diameter**	**CPC matrix**	**Ref**
Nylon66	100 µm	α-TCP	[94]
Aramide	15 µm	DCPA-TTCP	[96]
CNTs	60-100nm	DCPA-TTCP	[97]
CNTs	30-50nm	β-TCP-DCPA	[98]
Bioactive glass	< 20 µm	DCPD-TTCP	[99]
Wollastonite $Ca_3[Si_3O_9]$	10-20 µm	TTCP, poly(acrylic-co-itaconic) acid	[100]
β -SiC whisker	0.1-3 µm		[101]
HA whiskers	< 20 µm	TTCP, DCPA	[102]
Polypropylene	16.3 µm	α-TCP	[103]
PLLA	1-2 µm	α-TCP, DCPA, CaCO3	[104]
PGA /PLA	322 µm	DCPA-TTCP	[105-107]
PGA /PLA	322 µm	β-TCP	[93]
PGA/PLA (15% Chitosan as liquid phase)	322 µm	DCPA-TTCP	[108-110]
PCL	1.1-1.9 µm	α-TCP, DCPA, $CaCO_3$, PHA	[104]

2.4.3. CSC and CPSC fiber reinforcement

According to Banfill et. al., since 1960s extensive research on fibre reinforced cement matrices were all focusing on the mortar samples rather than paste, including fracture toughness enhancement and increase in electrical conduction of the cement [111]. Hassain and Sakai explain that carbon fibres increase fracture toughness of Portland cement due to the bridging effect of fibres, and crack tip plasticity mechanisms [112]. Banthia and Sheng studied toughness and strength improvements of micro-fiber reinforced Portland cement by fibers comprised of

carbon (d=18 μm, l=6 mm), steel (25x5 μm cross section, 3 mm long), and polypropylene (*d*= 4μm, *l*=6 mm) [113]. They reached a K_{IC} as high as 2.33 MPa√m for a paste sample with 3 wt% carbon fibers [113].

A very important group of fiber-reinforced CSCs are the Engineered Cementitious Composites (ECCs). ECCs are micromechanically designed composites, also known as bendable concrete with 3-7% strain capacity (compare to 0.1% in ordinary Portland cement). Li et. al. have been working extensively on ECCs [3-5,11,114-117]. Most of the recent works on ECCs, especially on self-healing behaviour of them have been performed on the PVA fiber-reinforced ECCs. Self-healing of the ECCs will be reviewed in Section 2.5.

To our knowledge, no study has been reported on fiber-reinforcement of the CPSCs so far. Because of the potential advantages of the new CPSC bone cements, it is crucial to study their toughness improvement mechanisms. Until now, there are few published works reporting on using fibers along with calcium silicate and phosphate, but none referred to mechanical properties and fracture toughness of the samples. Li et. al. have reported using PVA (not fibers, polymer solution), chitosan, methyl cellulose in a $CaSiO_3$-HAp-βTCP system, but their main goal was injectability and cohesiveness of the paste [88]. For CPSCs where the calcium silicate phase was C_3S, no report on fiber reinforcement was found.

2.5. Self-healing materials and cements

As mentioned in section 2.2.2, many factors control bone cement functions. Another cement property of great practical importance is self-healing; it leads to the damage tolerance; the ability to withstand defects and crack formation without failing, and to repair them using materials available in their vicinity (e.g. CO_2, water molecules, ions and proteins available in the

body fluids). Therefore, we are presenting literature review on self-healing materials and cements (Sections 2.5.1 and 2.5.2) and the self-healing of bone cements (Section 2.5.3).

One of the most outstanding properties of biological materials, which makes them superior to synthetic materials, is their "*evolutionarily optimised functional systems*"; their ability to self-heal and regenerate their functions upon being damaged by external loads [118]. Self-healing materials attracted interest in materials science. The first conference on self-healing materials was held in April 2007 in The Netherlands. Van der Zwaag described the impact of the self-healing in materials science: in the last 20 centuries, all strength and reliability improvement strategies were based on "*the paradigm of damage prevention*" [119]. The broad definition of damage is the formation of defects and cracks, which were not present originally [119]. Damage levels in any material can either remain constant or increase. Van der Zwaag further suggested "*damage management*" to increase materials strength and reliability, i.e. development of materials with built-in capability to repair the damage as they are performing their functions [119]. In such materials cracks may form, but the material is capable of repairing them and thus, restoring the material functionality. In natural tissues (e.g. bone and skin), "lifelong" performance is gained through their ability to repair/heal damages. A self-healing material is more "a system" rather than a material. It should: i) yield the desired performance; ii) sense the damage (healing trigger); iii) repair the damage [119]. In summary, self-healing expands the lifetime of the materials and increases economic and human safety qualities [119,120].

2.5.1. Self-healing polymeric cements

In polymeric materials the integrity of the structure is compromised, when cracks form. The concept of self-repair was reported in 1981 [121]. Lin et. al. showed that ethanol can assist to repair cracks in PMMA in less than 30 min [122]. White et. al. reported an autonomic self-

healing of polymers in natural materials [123]. In their system, a microencapsulated healing agent was released by crack intrusion. Then, upon contact with an embedded catalyst (Grubbs' catalyst) through a ring opening metathesis polymerization (ROMP), healing agent was polymerized to bond the crack faces together. As a result, the healed materials regained 75% of their fracture toughness [123-125]. Another reported technique uses hollow fibers, containing healing agents, which "bleeds" into the cracks by mechanical stimulus (e.g. fracture of the fibers) [126,127]. Later, Kalista et. al. reported that bullet holes in a plastic plate would heal up nearly instantly and reseal faster than the eye could see in several poly(ethylene-co-methacrylic acid) copolymers [128]. Blaiszik et. al. reported the production of controlled thickness of microcapsules from 300 nm to 300 μm [124]. In 2011, an article in Nature reported the optical self-healing in polymers, in which healing was activated by ultra-violet light [129].

In terms of self-healing of bone cements, few studies were performed on PMMA cement. Aseptic loosening, one of the main reasons for failure of cemented arthroplasties is caused by induced inflammation from debris particles formed as a result of cement fatigue failure. This can lead to bone destruction and loosening of the prosthesis [125]. This justifies the self-healing PMMA bone cement studies. Biggs et. al. reported the self-healing of a PMMA bone cement (Simplex®P) by using Grubbs' catalyst [130]. Healing agent was dicyclopentadiene encapsulated in poly (urea-formaldehyde) microspheres (diameter = 226 ± 51 μm). They showed a decrease in the cross-sectional area of the Grubbs' catalyst crystals, resulting in a significant increase in the polymerization rate of healing agent. They have also mentioned that the prospect of using such composite as self-healing biomaterial should be postponed upon evaluation of the biocompatibility of dicyclopentadiene and Grubbs' catalyst [130]. Wilson et. al. studied free-radical polymerization-based self-healing of PMMA and showed one of the encapsulated

initiators, exhibited 80% healing efficiency [125]. Although such examples could have extensive applications in polymer industry, but due to the toxic effects of monomer/initiators, their applications in bone cements has not been approved so far.

A few studies were performed on combining the polymer healing agents with concrete and cementitious materials. Dry et. al. have used hollow polypropylene (PP) fibers, filled with methyl methacrylate (MMA) monomer inside concrete to reduce permeability (by MMA bleeding) and showed that the material can be "repaired" [131,132]. Li et al. used hollow glass tubes, filled with ethyl cyanoacrylate (superglue) as a healing agent to seal the tensile cracks in cementitious composites [133]. There were no follow-up on this research, maybe due to the toxicity or cost of the materials or simply because there were simpler, more intrinsic healing mechanisms available for the calcium-silicate based cementitious materials (these will be reviewed in the next section).

2.5.2. Self-healing cementitious materials

A well-known ancient example of self-healing is the mortar used in the Romans buildings [119]. The mortar has held the stones and bricks together for over 20 centuries. Such outstanding durability is the result of spontaneous closure of micro-cracks through a dissolution-precipitation reaction between the mortar and the available moisture [119]. This is the intrinsic property of the calcium silicates in cementitious materials. Most types of concrete (even at older age) contain, some unhydrated cement particles that can be considered as “micro-reservoirs”, filled with healing agent. They can undergo further hydration upon reacting with the “ingress water” (through the cracks) and lead to partial or complete self-healing of the cracks [134].

Special type of composites called Engineered Cementitious Composites (ECC) have been intensively studied due to their significantly improved strength and toughness, compared to other types of cementitious composites [4,114,115,117,135-140]. Self-healing abilities of ECC were thoroughly investigated and demonstrated [5,6,9,10]. The four suggested mechanisms (Figure 2-3a-d) of such healing includes: a) Calcium carbonate precipitates within the cracks and thus "heals" the cracks, due to the dissolution of CO_2 in water into H_2CO_3, followed with reaction of H_2CO_3 with calcium hydroxide; b) Blocking the cracks by loose particles resulting from "*crack spalling*"; c) Crack makes the interior part of the cement water-accessible, causing further hydration of unreacted cement; d) Expansion of the hydrated matrix (through swelling of the Calcium-Silicate-Hydrate gel, C–S–H gel) [9]. It has been reported that through these "self-healing" mechanisms, ECCs are able to stabilize the crack width less than 60 μm [12,136,137,141]. Another reference indicates that such cracks should be typically below 100 μm [142]. Sisomphon et. al. has recently shown that cracks up to 400 μm wide can still be healed by addition of calcium sulfo-aluminate-based expansive additives (CSA) and crystalline additives (CA) [143]. This indicates the possibility of improvement and increasing the limit of crack healing size in ECCs by further studies of the effects of different compounds.

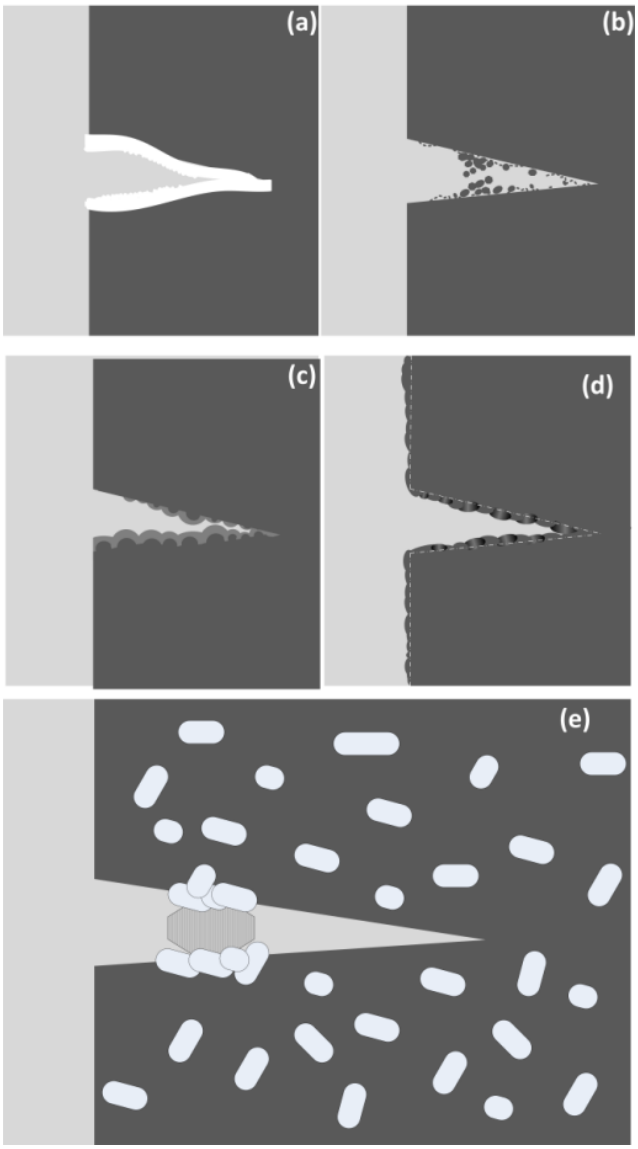

Figure 2-3- Schematic of self-healing of ECCs (a)-(d) redrawn from [9] and (e) redrawn from [2] (a) calcium carbonate deposition; (b) spalling particles filling the crack; (c) further hydration of remnant C_3S; (d) swelling of the matrix; (e) bacterial activation to produce calcium carbonate.

Boquet et. al. in 1973 showed that many bacteria (in soil media, as well as marine bacteria) are capable of calcium carbonate precipitating. They concluded "crustal formation" is a function of the composition of the medium [144]. In case of cementitious materials, some studies have suggested to use such crystal precipitation ability as a crack sealing measure for corrosion

protection of the concrete [145] or self-healing measure in construction industry [2,134,146-149]. Bacterial activity is reported to affect healing through enzymatic hydrolysis of urea, resulting in pH increase and calcite precipitation [2]. In some studies, bacteria have been applied manually on surfaces of cracked concrete structures, in order to repair the cracks [145,150]. Although this appears as an amazing natural method to heal engineered materials, some researchers claim that it cannot be categorized as self-healing [147,149], as it needs external assistance (e.g. manual application of the bacteria). However, we could assume that the bacteria are viable and available on the site of the application (e.g. in soil). This seems as a reliable assumption, considering the above statement of the Boquet et. al. [144]. Therefore, these methods also can be considered as self-healing. Following this route, Jonker et al. added spores of specific alkali-resistant bacteria (related to the genus Bacillus) to the concrete mixtures as a self-healing agent; this appeared to work successfully in healing of the cracks but the bacteria were viable for relatively short time (7 days to two months) [151]. Later on, to increase the viability period, they used porous expanded clay particles to surround and immobilize the bacterial spores and the precursor compound, and then added the whole "package" to the concrete mixture [147]. They described the mechanism of such healing to be as follows: "the germination of the spores" is activated by crack ingress water and acts as a catalyst to convert calcium lactate into calcium carbonate based minerals, which will accordingly fill the cracks. Active metabolic conversion of calcium lactate by the present bacteria can be written as follows:

$$Ca(C_3H5O_2)_2 + 7O_2 \rightarrow CaCO_3 + 5CO_2 + 5H_2O \qquad \text{Equation 2-5}$$

However, the authors did not study the effects addition of calcium lactate alone (i.e. without bacterial spores) [147] on crack healing; Calcium lactate could provide a source for Ca

ions and CO_2, even without the presence of the bacteria and upon the contact with water containing O_2.

De Muynck et. al. also used the bacteria externally [148] and showed self-healing in Portland cement. They however, used the bacteria along with the culture media, which itself consist of urea, $NaHCO_3$, ammonium chloride, and nutrient broth. However, the reference effect of the liquid phase alone should also be studied to provide a thorough understanding of the reactions happening in such healing process. De Muynck et. al. in their review paper have extensively described the mechanisms of how bacteria can assist in calcium carbonate precipitation. The primary role of the bacteria appears related to their ability to create a high-alkali environment, through different pathways involving either sulphur cycle or nitrogen cycle [149]. The effect through nitrogen cycle specifically includes: (i) Amino acid oxidative deamination in aerobiosis; (ii) Nitrate reduction in anaerobiosis or microaerophily; (iii) Urea or uric acid degradation in aerobiosis.

Due to the presence of several negatively charged groups on the cell walls, at a neutral pH, positively charged metal ions (e.g. Ca^{2+}) can be bound on bacterial surfaces and may subsequently react with anions (e.g. carbonate) to form an insoluble salt (e.g. calcium carbonate) [149]. So the cell membrane provides a nucleation site, while the anion itself (e.g. carbonate) may be a product of the bacterial metabolism. It has been demonstrated that specific bacterial outer structures play an essential role in the morphology and mineralogy of bacterially-induced carbonate precipitation [149]. Such assumption might be extended to eukaryote cells as well (including human cells). [JB asked to add ref, but this is my assumption]

2.5.3. Self-healing bone cements

Although self-healing bone cements are of great practical importance, only a very limited number of data in the literature are available on the healing ability of "bone cement". They are focused on PMMA bone cements (as mentioned in 2.5.1). Biocompatibility studies of PMMA self-healing systems, which contain either dicyclopentadiene (DCPD)-Grubbs' catalyst or peroxide initiators, are not provided. To our best knowledge, no study currently exists on self-healing ability of bioceramic bone cements (self-healing of nano-hyroxyapatite coating [152] and scratch self-healing of TiO_2 coating [153] was reported previously, but not for bone cements).

As mentioned in Section 2.5.2, several studies provided evidence of the self-healing ability of the Portland cement based composites, ECCs. Tri-Calcium Silicate (C_3S) is the main component of ECCs (more than 60 wt%) and as mentioned in Section 2.3.1, it is a bioactive bone cement [16,74]. As C_3S has the intrinsic self-healing properties, then if crack size within the set C_3S samples could be maintained within the self-healing limit of ECCs (~60 μm), we anticipate that it should also self-heal. The major hypothesis we put forward here is that its apatite forming ability in SBF might add a new healing mechanism for such systems in SBF (hence also in human body): cracks filling through precipitation of HAp inside of them. Fiber reinforcement increases C_3S-based cements tolerance toward cracks and thus, should enable producing stable cracked specimens suitable for studying the novel self-healing mechanisms of the fiber-reinforced composites. To our best knowledge, self-healing of C_3S-fiber reinforced composites, as well as self-healing of any bioceramic bone cement has not been studied before, although the concept draws on the similarities of this system to ECCs.

3. Scope and Objectives

Natural tissues have the self-healing ability to repair their structural defects without external assistance. Achieving the same characteristics in biomaterials could prevent revision surgeries and thus reduce pain, time and money, and ultimately increase the patient's quality of life. However, only a few studies investigated self-healing characteristic of bone cement and focused on polymeric bone cements (PMMA). To our knowledge, no research on self-healing abilities of bioceramic bone cements has been reported. On the other hand, there are reports on self-healing ability of chemically similar Engineered Cementitious Composites (ECC) construction materials, where the matrix consists mainly of Tri-Calcium Silicate (C_3S). C_3S cement has been determined to be osteoconductive, bioactive and osetoinductive [15]. The principal hypothesis of this work is that self-healing can be identified and promoted in bioceramic cements consisting of C_3S-based fiber-reinforced composites exposed to Simulated Body Fluid (SBF). The principal focus and the broad objective of the present dissertation is therefore to demonstrate and investigate the mineral-deposit assisted self-healing abilities of the C_3S-PVA composite cements, through exposure to SBF.

According to the recent reports, combination of C_3S with 10wt% of Mono Calcium Phosphate (MCP) results in superior compressive strength of such Calcium Phosphate Silicate Cement (CPSC) [154]. The biocompatibility and bioactivity of CPSCs increases by increasing the calcium phosphate content in the cement [81]. As the self-healing processes in these cements relate to their bioactivity, it was further hypothesized that inclusion of calcium phosphate in the cements could improve their self-healing abilities. Based on these observations, we have selected

C_3S-10MCP cement (i.e. C_3S with 10wt% MCP addition) as representative of CPSCs, with the expected better biocompatibility than C_3S composites. The pure C_3S composite cements were tested in parallel, to set the reference state for the effects of MCP additive on their self-healing abilities. Another set of reference samples included both C_3S composite cement and C_3S-10MCP composite cement exposed to distilled water instead of SBF. This set of comparative experiments aimed at determining the effects of the environment (i.e. SBF vs water) on the self-healing processes.

The process engineering and preparation methods of the composite cements were studied in detail. In the preliminary study it was determined that the self-healing ability of these cements is limited to defects (cracks) width lower than ~100 μm. Therefore, fiber reinforcement had to be implemented to increase toughness of the cement samples to sufficiently high level to achieve fracture stability (i.e. crack tolerance) without losing the overall integrity of the samples. To study the details of the self-healing process, the reinforced samples were loaded in three-point-bending (3PB) over their maximum load bearing capacity to produce stable cracks. Then, various healing treatments were performed by soaking the samples in either water or Simulated Body Fluid (SBF) at 37°C. Post-healing mechanical tests in 3PB were repeated on the same samples to determine restoration of the load-bearing capacity due to the healing process. Crack elimination due to healing was examined in the macrostructure and microstructure level, through optical and electron microscopy. XRD and FTIR spectroscopy was used to study phase composition of the healed cement samples.

The specific objectives of this dissertation are:

- **To study process engineering of fiber-reinforced ceramic cementitious composites**, with the goal of finding a practical and simple method to prepare toughened C_3S and C_3S-10MCP based composites; to determine fiber-reinforcement effects using carbon fibers and PVA fibers; to study the effects of fiber reinforcement on the compressive strength, load capacity and energy absorbed before failure in three-point-bending of C_3S and C_3S-10MCP based composite.
- **To develop controlled-fracture methodology** in order to produce samples of C_3S and C_3S-10MCP based composites with stable micro cracks within the specific crack width range of 50-100 μm.
- **To demonstrate and investigate the self-healing abilities** of the partially-damaged fiber reinforced C_3S based and C_3S-10MCP based composite cements, through exposure to distilled water and SBF at 37°C; to perform macro and microstructure analyses of the effects of self-healing treatments on cracks morphology and cracks elimination; to determine restoration of the load-bearing capacity of the cements subject to the healing treatments.
- **To study and identify the healing mechanisms** that lead to the restoration of the load-bearing capacity of the cements; to explain the dependency of the healing process and characteristics on the crack width; to suggest improved methods towards accelerated healing of calcium silicate based cementitious composites.
- **To investigate the effects of calcium phosphate addition** to the C_3S-fiber reinforced bioceramic cements on the mechanical properties and self-healing abilities of such modified Calcium Phosphate Silicate Cement (CPSC) composites.

4. Materials and Methods

4.1. Materials, synthesis and preparation methods

In this Section, details on the materials manufacturers, methodology of preparation and synthesis of the samples are presented.

4.1.1. Preparation of Tri-Calcium Silicate (C_3S) Powder

The C_3S preparation method was similar to Zhao et. al. work [74] with minor alterations. Tetra-Ethyl-Ortho-Silicate (TEOS, Sigma Aldrich) solution was used as a source of high-surface area (active) silica, with proper amount of calcium nitrate to provide Ca/Si molar ratio of three. 10cc of 1 molar nitric acid was used as catalyst in one litre of solution. The initially formed sol was stirred for three days to form a viscous gel. The gel was dried at 140˚C for 24 hours. The obtained powder was fired at 1000˚C for two hours and then at 1450˚C for another two hours. The powder was ball milled 3 times, each time for 20 min in the planetary ball mill (Fritsch Pulveristee5, Quebec, Canada) to obtain particle size of about 5-20μm, as determined through SEM observations. The XRD phase analysis confirmed that the obtained powder was C_3S (Figure 4-1).

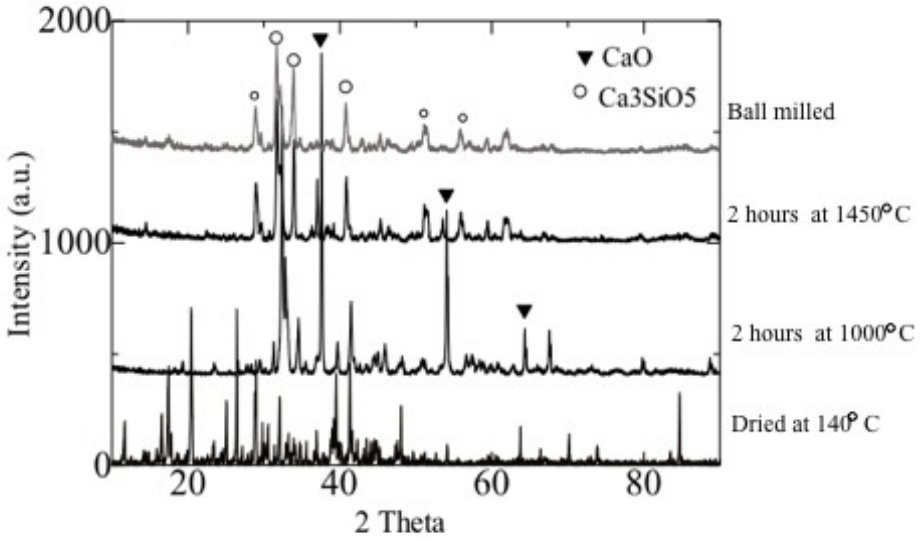

Figure 4-1- XRD patterns of powders from different stages of C_3S synthesis.

4.1.2. Preparation of SBF

The Simulated Body Fluid (SBF) was prepared based on chemical composition of SBF-JL2 in Bohner and Lemaitr paper [46]. This type of SBF was selected because it does not contain K^+, Mg^{2+}, SO_4^{2-} [46]. Also, as the calcium and phosphate are dissolved in two separate solutions, this disables the precipitation of calcium phosphates from supersaturated solution (e.g. as opposed to single solution recipes of SBF). Thus by this method, storage of the SBF is possible for longer times comparing the single solution recipes of SBF. The chemical composition is reviewed in Table 4-1 (All materials from Fisher Scientific, reagent grade).

Table 4-1- Chemical composition of the SBF.

	Solution A	**Solution B**
NaCl (g/l)	6.129	6.129
$NaHCO_3$ (g/l)	5.890	-
Na_2HPO_4. $2H_2O$ (g/l)	0.498	-
$CaCl_2$ (g/l)	-	0.540
Volume of HCl 1.00 M solution (ml/l)	0.934	0.934

4.1.3. Fibers details

Carbon fibers were pitched based (Zoltek- PANEX®), with 6 mm length and 7μm diameter. High molecular weight polyvinyl alcohol (PVA) fibers (Nycon RECS07), with 6 mm length and 24 μm diameter were used. Critical length (L_c), as the minimum perfectly aligned fiber dimension to transfer maximum stress [155], could be calculated for such fiber dimensions using simplified formula ($L_c = \sigma_f d/2\tau$, where σ_f is fiber tensile strength, d is fiber diameter, and τ is interfacial shear bond strength between the fiber and matrix) [155]. Assuming τ is approximately similar to that of ECCs for PVA fibers (τ=3.7 MPa, σ_f=*1640 MPa*) [156], L_c will be 5.2 mm. PVA fibers were used to reinforce the cement at 2.2 wt% (equivalent to approximately 5 vol% of the fibers in set cement matrix). By using higher PVA fiber content, fibers were not distributed homogenously and their mechanical properties had significant variations (see Appendix I). For carbon fibers, the highest amount that could be added to the paste was 3 wt% (equivalent to about 5 vol%) by hand-mixing without dispersants. Figure 4-2 shows SEM images of the carbon fibers and PVA fibers.

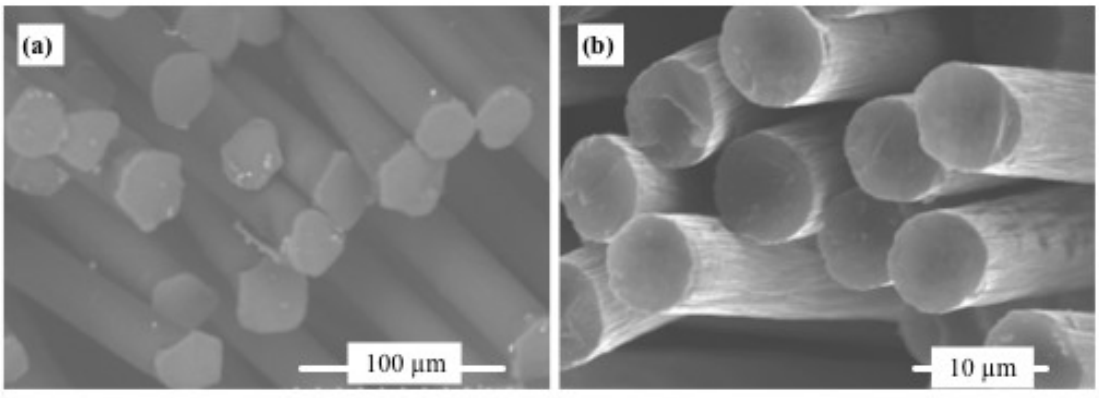

Figure 4-2- SEM images of the PVA fibers (a), and carbon fibers (b).

4.1.4. Cement and sample preparation

All cement samples were hydrated using Liquid/Powder (L/P) ratio of ~0.4 (attained through trial and error). Liquid phase was distilled water, Methylcellulose solution or PEG solution. The PEG solution was solution of distilled water/5wt% Poly Ethylene Glycol (PEG) (Fisher Scientific, Mw=200 g/mol). The Methylcellulose solution (The Dow chemical company) was prepared according to the manufacturers description.

To prepare the cement, the required amount of powder was split in half. The first half was mixed with spatula and whole amount of the liquid phase, after mixing for 1-2 min the other half of the powder was added. Then the moulds were filled with the paste using a spatula. Both surfaces were covered by glass sheets and griped by a metal paper clip. The moulds, glass sheets and clips were put in a plastic bag, filled with distilled water and kept at 37˚C. They were de-moulded after 1 or 3 days, transferred to a smaller plastic bag, filled with distilled water and placed back to the bath for pre-determined hydration time, i.e. for 1hr to 28 days.

For samples containing fibers, the procedure was slightly different. Fibers were added with liquid phase in the mortar and pestle. They were mixed to ensure separation of the fiber bundles, and then the powder was added and the rest of the procedure was similar to the above paragraph. This method was the result of trial and error to find a way to mix the fibers in such small scale. We used a primary method to semi-quantify the homogeneity of the fibers (see Appendix I). An example of a homogeneous and a non- homogeneous distribution of the fibers can be seen in Figure 4-3. In some cases the fibers were visibly remain in the form a bundle, thus the paste was not castable.

Liquid phase choices: We made the samples by casting the paste into a HMWPE mould. For brittle samples, one of the challenges were to de-mould samples without breaking them. It was almost impossible to de-mould the C_3S-10MCP samples with methylcellulose solution as liquid phase (brittleness was confirmed by NTP test result: $K_{IC}< 0.01$ MPa.$m^{0.5}$). The focus of this research was on calcium phosphate silicate toughening. Therefore, in order to study the effect of PVA fibers, it was essential to be able to produce control samples. As discussed, control samples of C_3S-10MCP-methyl cellulose were too brittle to be de-moulded. Therefore, another method was required to mix PVA fibers by hand, so that the un-reinforced control samples would be available for comparison. We used 5wt% PEG200 in distilled water solution (which in total composites will be less than 2wt%).

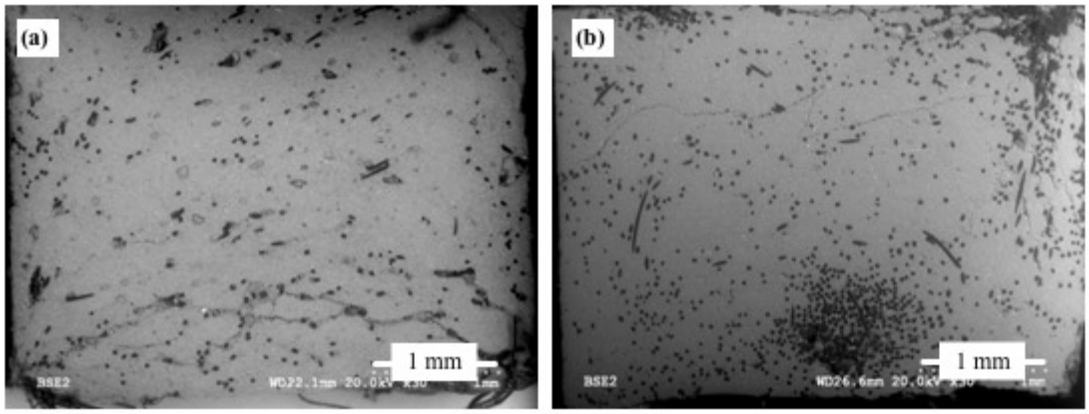

Figure 4-3- Examples of different distribution of fibers in cross section of the samples.

4.2. Analysis methods

4.2.1. Phase analysis

For analysing crystal structures of different phases, X-Ray Diffraction with Cu-Kα (λ=1.5418Å) was used in a standard mode (Instrument: Rigaku Model MultiFlex). The machine was set to run at 40 kV, 20 mA with the scan range of 10-70° and step size of 2 degree/min. The Jade software is used to identify the peaks in the XRD patterns. We used powder XRD and in case of set samples, we used mortar and pestle to grind the samples and used a sample holder that needed ~1-1.5g of sample. In some cases, amount of available sample was not enough to run the test with such setup. For the precipitates from the surfaces maximum ~0.2g of sample could be obtained. Therefore, we used another XRD machine, which could run analysis on samples as low as ~0.1g powder: (Instrument: Bruker D8 Focus Bragg-Brentano diffractometer equipped with a Fe monochromator foil), Co-Kα (λ=1.7889Å). The samples were grounded into fine powder with an alumina mortar, and smeared with ethanol to form a paint-like material, which was then applied on to a zero-diffraction quartz plate.

To study the chemical elements present in the compositions, during SEM imaging, EDX was used to map the elements or determine the chemical elements present. EDX could only give qualitative or semi-quantitative information about the amount of available chemical elements.

In order to obtain information of the available functional groups in the samples, a Perkin Elmer spectrum 100 - FTIR machine was used and the test was performed by Attenuated total reflectance (ATR) method, using Tl-Br-I plate (diamond coated). We used agate mortar and pestle to grind ~0.25 g of the samples. The background spectrum was scanned and the machine was calibrated. The transmission percentage was scanned over the range of 275-4000 cm^{-1}.

Pressure applied to secure the sample on top of diamond window was an automatic slip-clutch screw.

4.2.2. Microscopy and microstructure analysis

A Hitachi S-570 SEM with a tungsten filament was used. The fractured toughness sample surfaces are examined in both variable pressure and high vacuum mode. For high vacuum samples, they were gold-palladium or carbon coated for 30 second using a sputtering machine. For macro-structure analysis, a Nikon ECLIPSE MA200 light microscope was used, by. We used Nikon DS-Fi1 digital microscope camera head and NIS Element software to capture pictures.

4.2.3. Mechanical properties analysis

Compressive and three point bend tests were performed by Instron 3369 (hydraulic, Buckinghamshire, UK) and NTP tests by Instron model 4301.

4.2.3.1. *Compressive Strength*

Compressive strength was determined on cylindrical samples (6mm diameter, 12mm height). Average compressive strength is reported based on the results for at least three samples. A 50kN load cell was used with cross head speed set to 0.2mm/min. In order to decrease the effect of friction between cross head and the platform with the sample, we used copper foil (In the vicinity of the compression faces the local strain rate is reduced and plastic deformation is no longer homogenous [157]), shown in Figure 4-4.

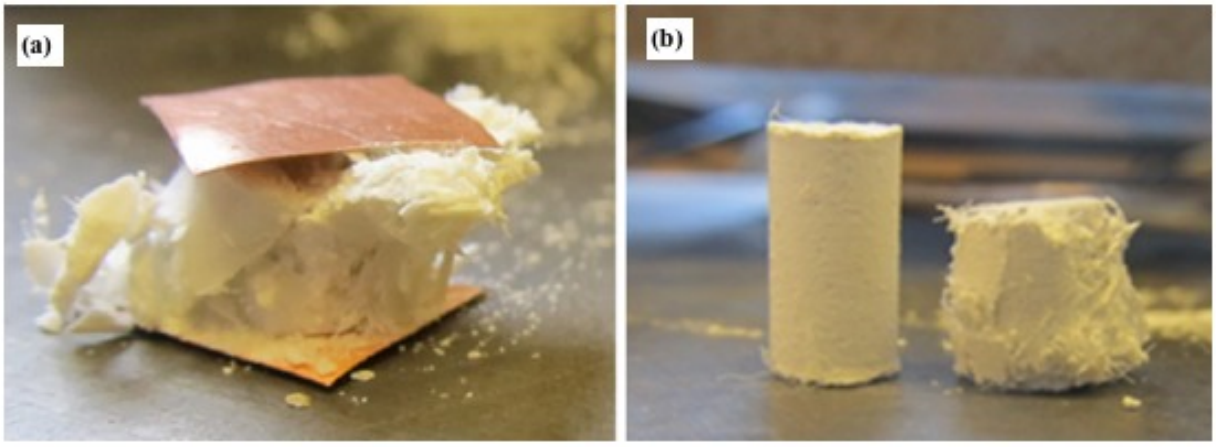

Figure 4-4 (a) The compression sample after the test with copper gasket on both sides; (b) comparison between as received sample and the compression tested sample.

4.2.3.2. *Notchless Triangle Prism (NTP) test*

To measure toughness, moulds were designed to produce a prism (6x6x6mm triangle in cross section and 12 mm height). We used a novel technique designed by Ruse et. al. [158]. The rationale of this test is to solve the problem of sample preparation for brittle materials in Chevron Notched Short Rod (CNSR) test. The triangle prism sample can be easily produced from cements by moulding. To calculate the fracture toughness, they have used same formula as CNSR and modified the values of Y*min based on the specific configurations of the NTP test:

$$K_{IC} = \frac{P_{max}}{DW^{0.5}} Y^*_{min} \qquad \text{Equation 4-1}$$

Where P_{max} is the maximum load recorded during testing, D is specimen diameter (12mm), W is specimen length (10.5mm) and Y^*_{min} is the minimum value of dimensionless stress intensity factor coefficient, which Ruse e. al. calculated it for the NTP test configuration as 28 (with estimation of uncertainty of extrapolation to be 10%) [4].

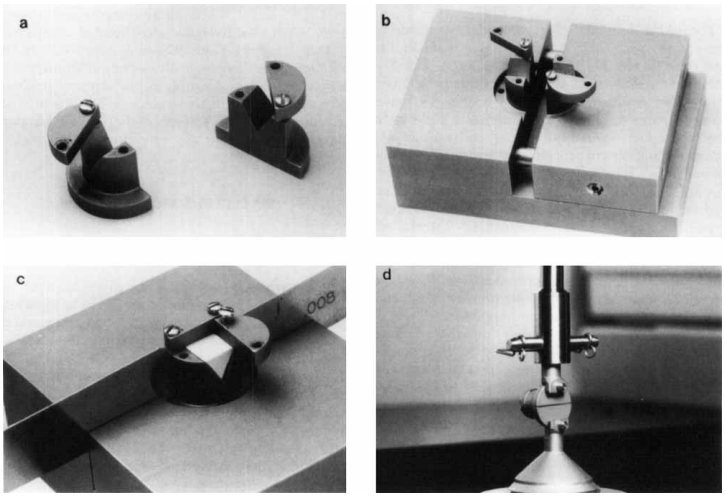

Figure 4-5-(a) Holder for the NTP specimen (b) Mounting block with specimen holder; (c) Mounting block with specimen holder, NTP sample, and spacer blade; (d) Custom-designed grips securing the holder and an NTP specimen (with kind permission of Wiley) [158].

4.2.3.3. *Three-point-bend test*

Three point bending tests were performed on rectangular prism samples with following dimensions: width b=3 mm ± 0.1 mm, height d= 4 mm ± 0.1 mm, and span length L= 25 mm. For concrete and fiber reinforced concrete samples, the span/thickness ratio should be higher than three [159]. On the other hand, for flexural strength measurements of PMMA bone cements the samples are smaller and the ratio is higher than seven [160]. For calcium phosphates different sizes are reported, with span/thickness ratios as high as 15 [161]. Our sample size was used due to availability of the moulds and the span/thickness ratio is more than 8. Although the results are not standard, they are viable for comparison. The cross-head speed of 0.05 mm/min was applied. The maximum bending stress in such samples can be calculated from the following formula: flexural strength= $3fl/2bd^2$ (Equation 5-1). Average and standard deviation are reported based on the results for at least three samples.

The area under the load-deflection curves was calculated for the three-point-bending tests, in which the loading was carried out all the way to reach the loads as low as 5N. This area is associated with the energy absorbed in the deformation processes. The stiffness of our samples were two orders of magnitude lower than the machine frame stiffness, therefore we concluded the effect of machine deflection on the total displacement read is negligible.

4.2.3.4. Three-point-bending as a tool to pre-crack samples

To study the self-healing, we needed to pre-crack the samples and study the crack behaviour in various healing treatments. Therefore, the three-point-bending test on the same geometry specimens was carried out, but stopped loading after reaching the maximum load, and before sample failure was completed. Fiber-reinforced samples have multiple peaks in their load-displacement curves, so it was not possible to define a threshold for the machine, e.g. to stop the load after 10% drop in the max load. In order to make sure that the sample has passed the maximum load we needed to look for the load-bearing capacity to be decreasing continually. Also, visible cracks were a good sign to make sure the sample has passed the maximum load. Therefore, we stopped the test manually, after making sure that it had passed the maximum load (the stop criteria will be discussed in Section 6.1.1 and 6.1.2).

Heavily cracked and deformed samples were kept at 37˚C in water or SBF in "as-cracked" state or were re-aligned using Poly Vinyl Chloride (PVC) rod "splints" to partially close the cracks (Figure 4-6) and then kept at 37˚C in water or SBF "with splint". Time of soaking was from one hour to 28 days to evaluate self-healing process. The three-point-bending test was performed on the samples soaked 7 days and 28 days in SBF and water.

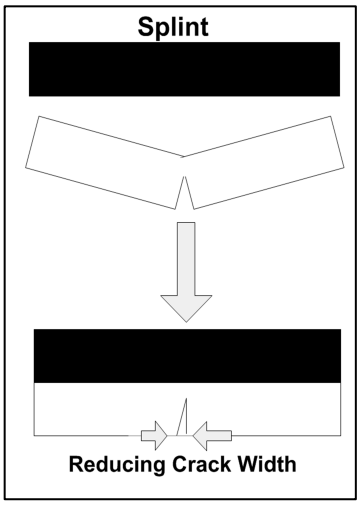

Figure 4-6- Schematic of the effect of splint on closing the mouth of the crack.

4.2.4. Details of pH measurements

An Omega PHB-209 - pH/mV Bench Meter with the resolution of 0.01 pH was used to measure the pH. A double junction, plastic body, gel-filled electrode was used. pH readings were performed in two methods: i) Set sample soaking: the 10-days-set samples were soaked in 50cc SBF or distilled water and the pH was measured in times up to one week; ii) Paste soaking: after mixing the powder with the liquid phase, the paste was moulded in the lid of the glass tube. 6cc SBF or distilled water was used in contact with the paste immediately. We wanted to use the minimum amount of liquid possible to measure the pH and stimulate the confined space inside of the crack, where the small amount of liquid is in contact with fresh C_3S. Due to available instrumentation and probe size, 6cc was the minimum amount of liquid that could fully soak the probe. The pH was measured in different times up to 7days.

5. Mechanical Properties and Microstructure Analysis of Fiber-Reinforced C_3S and C_3S-10MCP Composites

As mentioned in the literature review, Calcium Silicate Cements (CSC) and Calcium Phosphate Silicate Cements (CPSC) offer new prospects as bone cements. However, their brittle nature is an obstacle to be overcome before these cements can be considered for load-bearing applications. One of the most well-known methods of toughening ceramics is fiber-reinforcement. In this chapter, the effects of fiber-reinforcement on mechanical properties of one member of the CSC family (C_3S) and one member of the CPSC family (C_3S-10MCP) is presented. To the best of our knowledge, fiber-reinforced CPSC has not been reported before. Our objective was to investigate the possibility of toughening CSC and CPSC to allow us to produce stable cracks in the samples, without compromising their structural integrity (i.e. causing them to shatter). Such tough fiber-reinforced CSC and CPSC will be used in Chapter 2 and 3 for self-healing analysis.

5.1. Fracture toughness of the composite cements

To evaluate fracture toughness of the samples, we used Notchless Triangular Prism (NTP) method [158]. As mentioned in Section 4.2.3.2, the rationale of using this test is to simplify sample preparations for brittle materials in Chevron Notched Short Rod (CNSR) test. The results of NTP test are reviewed in this section.

5.1.1. NTP test results

Figure 5-1 and Table 5-1 show the results of the NTP tests for C_3S and C_3S-10MCP based composites and their plain matrix. We used carbon fibers and PVA fibers as reinforcement, with either distilled water (W) or methylcellulose (MC) solution as the liquid phase (as mentioned in the Section 4.1.3, the mixing of PVA fibers with distilled water was not possible).

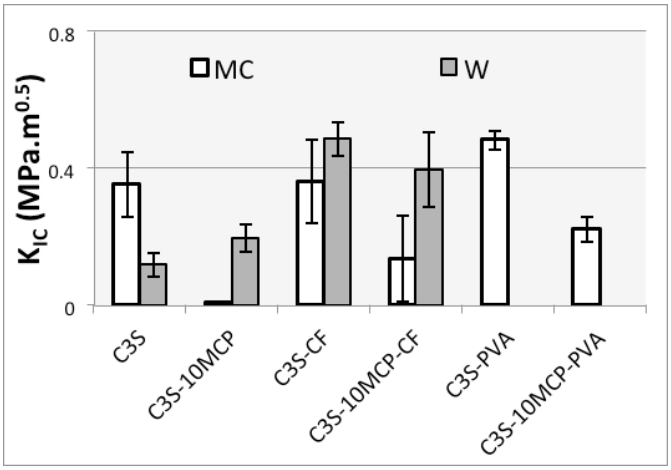

Figure 5-1- Fracture toughness results of NTP test.

Table 5-1- Fracture toughness results obtained by NTP test.

Liquid Phase:	Methylcellulose		Distilled Water	
Sample name	K_{IC} (MPa√m)	SD	K_{IC} (MPa√m)	SD
C_3S	0.35	0.01	0.12	0.04
C_3S-10MCP	0.01		0.20	0.04
C_3S-CF	0.36	0.12	0.49	0.05
C_3S-10MCP-CF	0.14	0.13	0.40	0.11
C_3S-PVA	0.48	0.03	N/A	N/A
C_3S-10MCP-PVA	0.22	0.04	N/A	N/A

As Table 5-1 shows for C_3S samples, when water was used as liquid phase, adding carbon fibers quadrupled the fracture toughness (from 0.12 to 0.49 MPa√m). When methylcellulose was used as liquid phase, fracture toughness of un-reinforced matrix increased to

0.35 MPa√m. Methylcellulose is used to help the dispersion of carbon fibers in cement [162]. However, using carbon fibers to reinforce C_3S with methylcellulose as the liquid phase did not significantly change its fracture toughness (from 0.35 to 0.36 MPa√m).

For C_3S-10MCP samples, Table 5-1 shows that using methylcellulose solution as the liquid phase instead of distilled water causes the samples to become exceptionally brittle (0.01 MPa√m compared to 0.20 MPa√m). The dramatic decrease in K_{IC} values using methylcellulose liquid phase can be improved by carbon and PVA fiber reinforcement. However, the reinforced values are still less than half of the values obtained for their C_3S counterparts. The K_{IC} value for C_3S-10MCP-CF (0.14 MPa√m) is less than half of the K_{IC} value for C_3S-CF (0.36 MPa√m) and the same for C_3S-10MCP-PVA (0.22 MPa√m) compared to C_3S-PVA (0.48 MPa√m).

K_{IC} of the C_3S-10MCP is higher than C_3S samples with water as the liquid phase (0.20 MPa√m compared to 0.12 MPa√m). Toughness of all the other C_3S-10MCP based samples was lower than their C_3S counterpart samples. In order to understand and explain the mechanisms ruling such behaviour we studied macro and microstructures of the fractured samples by SEM (see Section 5.1.2).

5.1.2. Microstructure analysis of fractured surfaces of NTP samples

In this subsection, we study the macro and microstructure of the fracture surfaces of NTP test samples via scanning electron microscope.

5.1.2.1. *Microstructure analysis of unreinforced matrix*

To better understand the effect of the reinforcements, we initially examined the plain matrix microstructure. Figure 5-2 shows the fracture surface of C_3S sample, set for 10 days in water at 37°C and fractured in NTP test. In this sample, 120-180 μm sized macro defects are

observed. These defects are filled with thin hexagonal platelets with the following dimensions: 30-100μm width and 2-6μm thickness (Figure 5-2c,d). The EDX of all these platelets (Figure 5-2e) shows the only chemical elements present are calcium and oxygen (hydrogen cannot be detected by EDX). This observation is consistent with the literature on hydration products of C_3S [76,77] and suggests that the phase is calcium hydroxide. Figure 5-3 shows microstructure of the sample's surface, with relevant EDXs of the phases. As shown before, the platelet phase is calcium hydroxide (Figure 5-3a). The sub-micron fibrous phase is calcium silicate hydrate gel, showing calcium, silicon and oxygen in its EDX determined composition (Figure 5-3b). There is a significant amount of remnant C_3S particles available in the matrix (i.e. only 40% of C_3S hydrates after two weeks, according to the hydration graph presented in the literature [76,77,163]. In a crack-free 10-day-set sample, the C_3S particles are covered with a layer of the hydration products and are not exposed to the aqueous environment. However, the EDX has a penetration depth of ~5μm, therefore EDX performed on the sub-micron fibrous phase (Figure 5-3b) also includes counts for the underneath layer. This can explain higher Ca/Si ratio rather than C-S-H gel range (Ca/Si ratio in C-S-H gel is 0.8-2.1 [164], while Ca/Si ratio of C_3S is three).

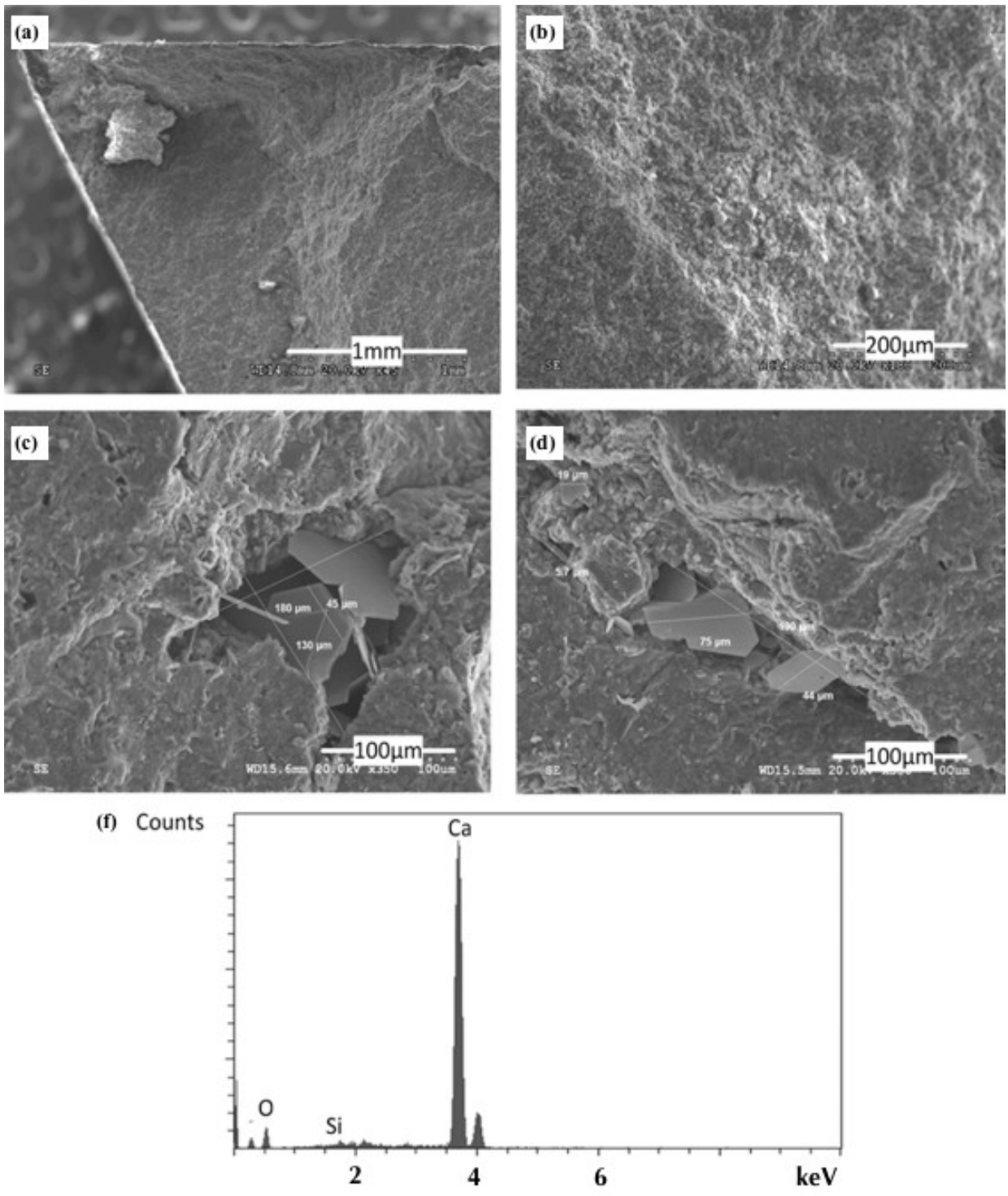

Figure 5-2- SEM images of fractured surface of notched triangular prism (NTP) of C_3S sample set for 10 days in water at 37°C (a-d), EDX result of the platelet-like phase (f).

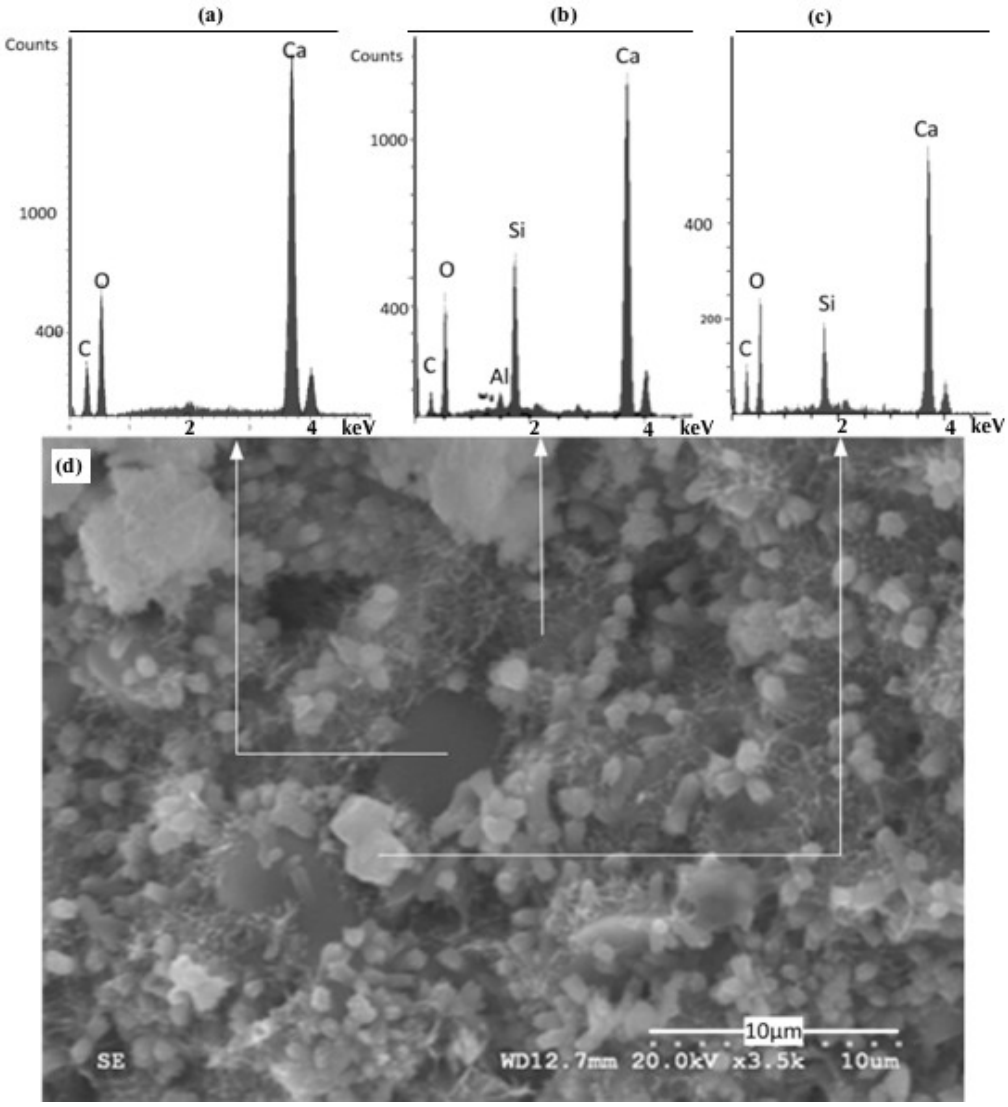

Figure 5-3- Results of EDX analysis (a,b,c) as the locations are indicated in figure (d), which shows microstructure of the C_3S NTP sample-set 10 days in water at 37°C.

Figure 5-4a-g shows the SEM images of C_3S-10MCP fracture surface. We also scanned EDX over Figure 4(g) area and included the results in Figure 5-4h. The C_3S-10MCP microstructure is similar to the C_3S sample. While the thickness of the platelets for both samples is in the same range (2-6 µm), the width of calcium hydroxide platelets is smaller (10-50 µm) than the width of C_3S calcium hydroxide platelets (30-100 µm). We could not identify areas with

high phosphorus content during EDX mapping. This implies homogeneous distribution of MCP in the samples.

As mentioned in Section 5.1.1, K_{IC} of the C_3S-10MCP samples is higher than C_3S samples (0.20 MPa.m$^{0.5}$ compared to 0.12 MPa.m$^{0.5}$). This can be explained by the energy dissipation during micro-crack formations, as we can see 1-2 μm wide micro-cracks on the fracture surfaces of the sample (Figure 5-4d).

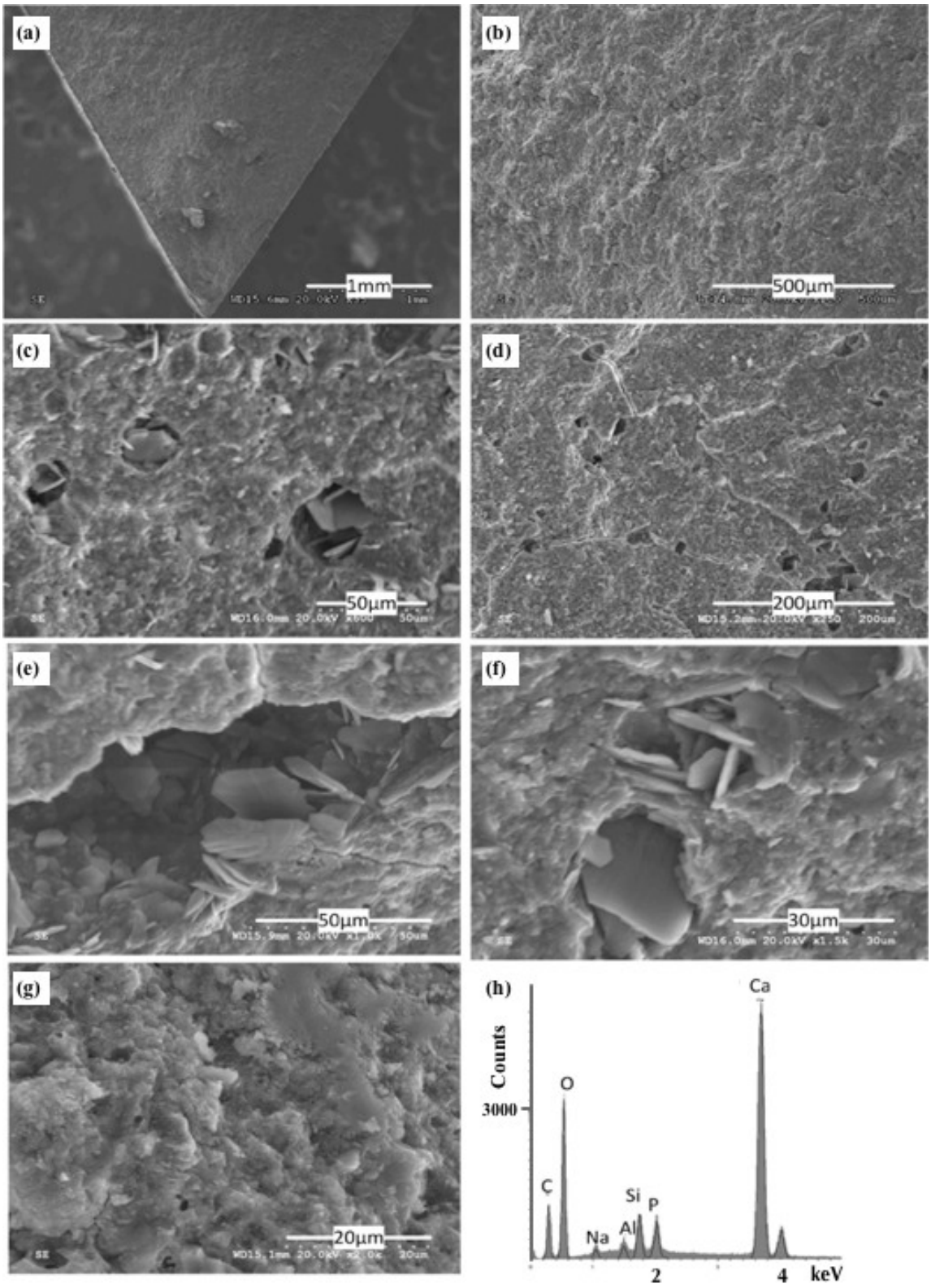

Figure 5-4- SEM image of fractured surface of C_3S-10MCP NTP sample (a-g), (h) the result of the scanned EDX over the area in image (g).

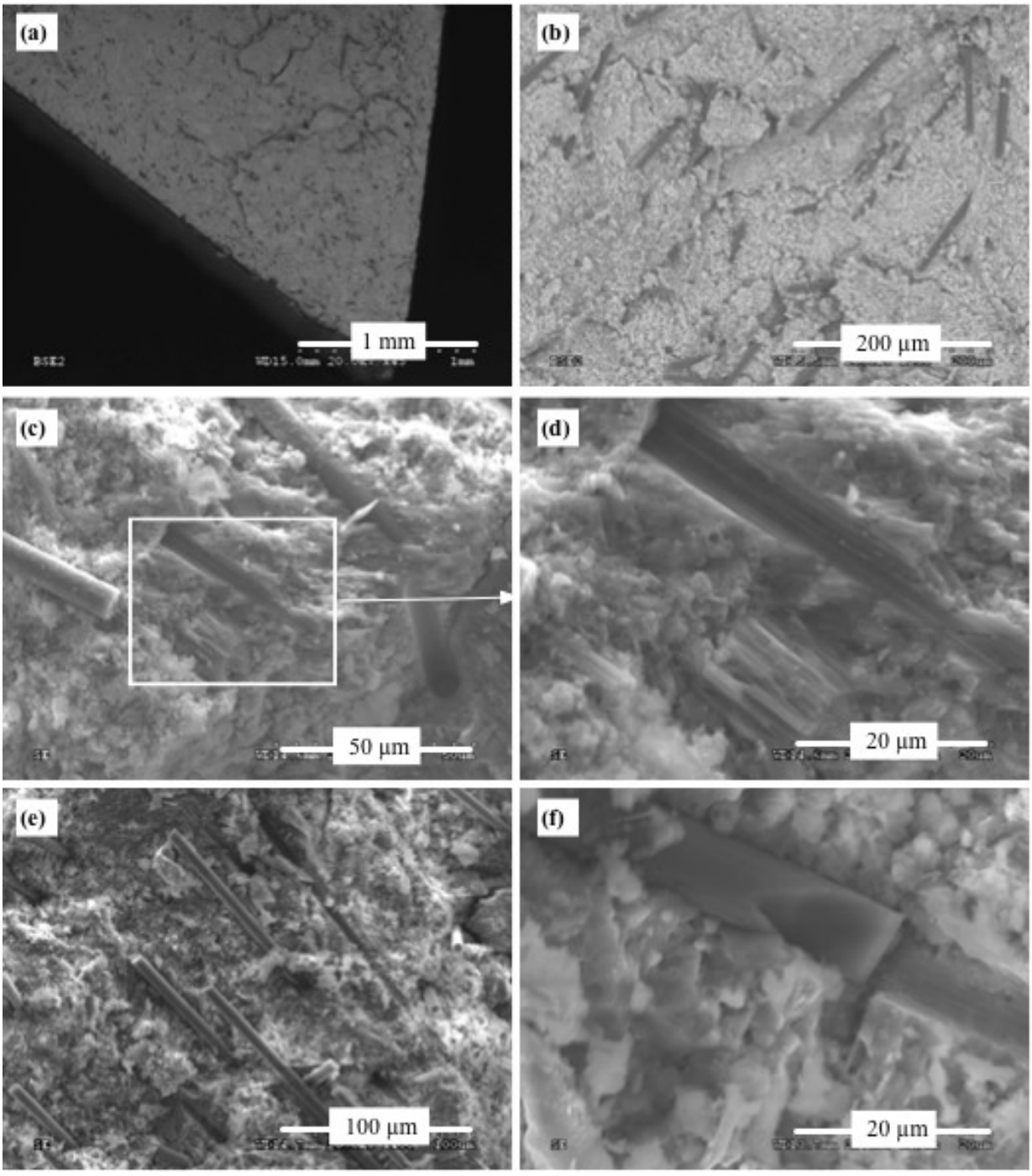

Figure 5-5- Fractured surface of triangle prism of C_3S-10MCP-CF sample.

Figure 5-5a shows SEM images of the C_3S-10MCP-CF macrostructure, whereas Figure 5-5b-f shows the respective microstructures and Figure 5-5d shows higher magnification of a pull out groove. As discussed in the literature review, fiber pull out is one of the main toughening mechanisms of fiber-reinforced ceramic matrix composites [91]. The carbon fibers projecting out of the fractured surfaces are not covered by the matrix particles, and they are not deformed or dented (Figure 5-5). This "cleanness" of the fiber surfaces indicates minimum interaction with the matrix and confirms mechanical interlocking as the only type of the fiber/matrix bonding [111,112,165].

5.1.2.2. *Microstructure analysis of PVA reinforced samples*

Figure 5-6 and Figure 5-7 show the C_3S-PVA and C_3S-10MCP-PVA fractured surface of the NTP test. Toughening mechanisms such as fiber bridging, fiber pull-out, and fiber plastic deformation are visible in these figures. The chemical bonds between PVA fibers and the matrix is indicated by the following phenomena: The fibers are covered by attached matrix particles (Figure 5-6a), suggesting the fiber/matrix bond is stronger than the bond among matrix particles;

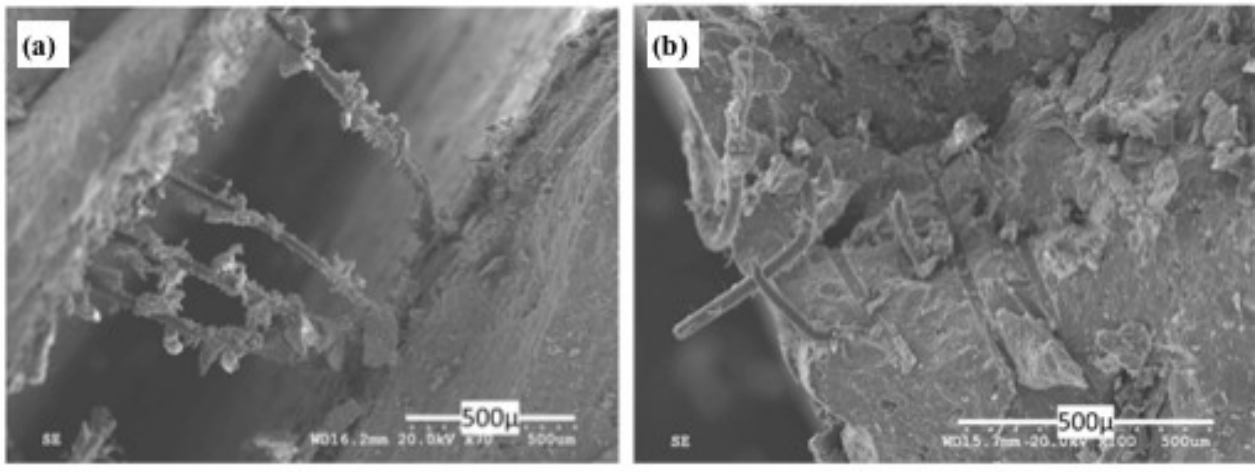

Figure 5-6- Fractured surface of C_3S-PVA NTP sample.

Figure 5-8 compares SEM images of the PVA and carbon fibers projecting out of the fractured surfaces of the composites. PVA fibers deform plastically and show the characteristics of the ductile rupture, where the end of the fibers are elongated and plastically deformed (Figure 5-8b,d). The fiber surfaces are covered by attached matrix particles or have permanent marks and indents from the detached matrix particles on their surfaces. Carbon fibers on the other hand, are brittle and show no plastic deformation on their fractured end. This can explain why PVA reinforcement has been more effective than carbon fibers.

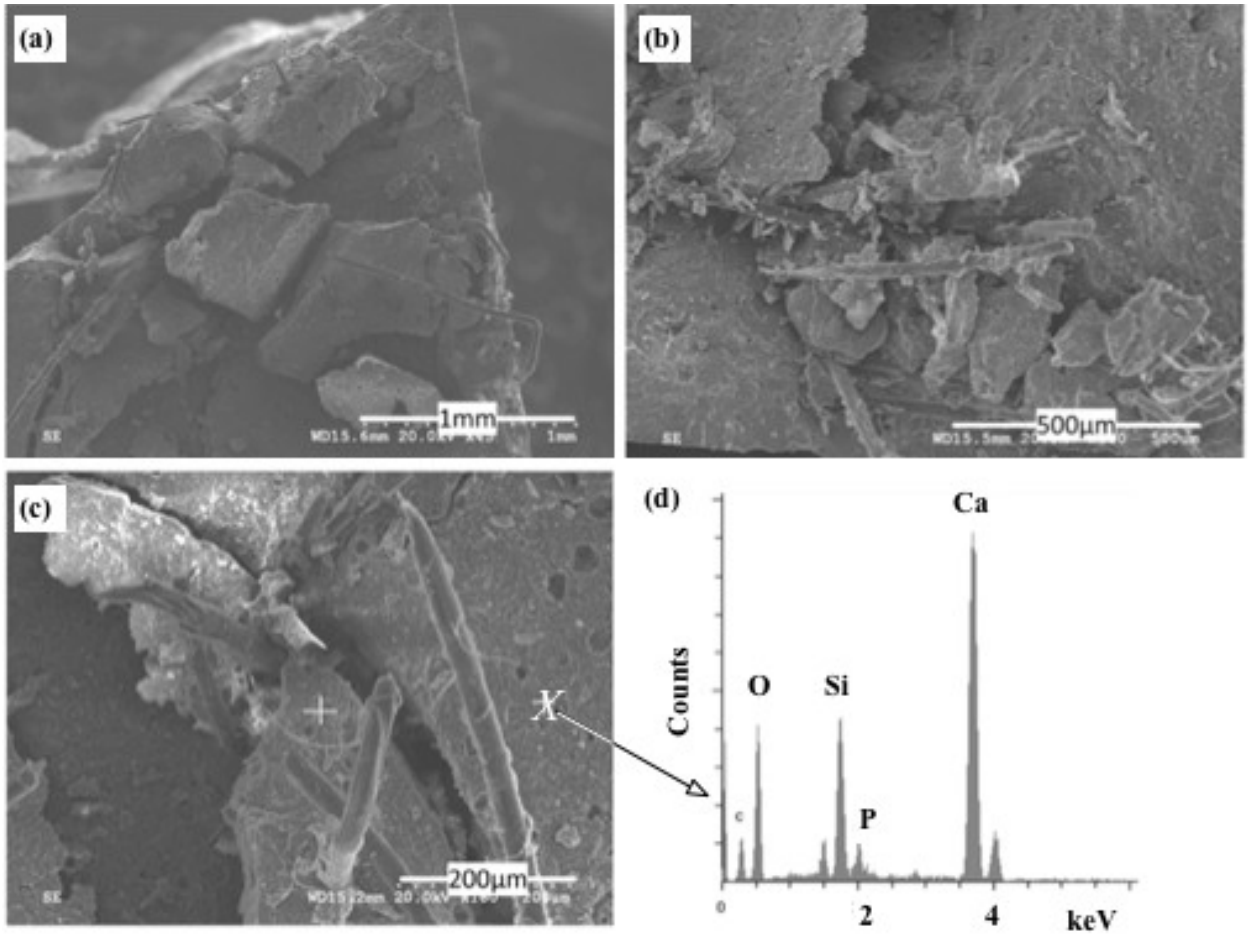

Figure 5-7- Fractured surface of C_3S-10MCP-PVA NTP sample (a-c) and EDX of the matrix (d).

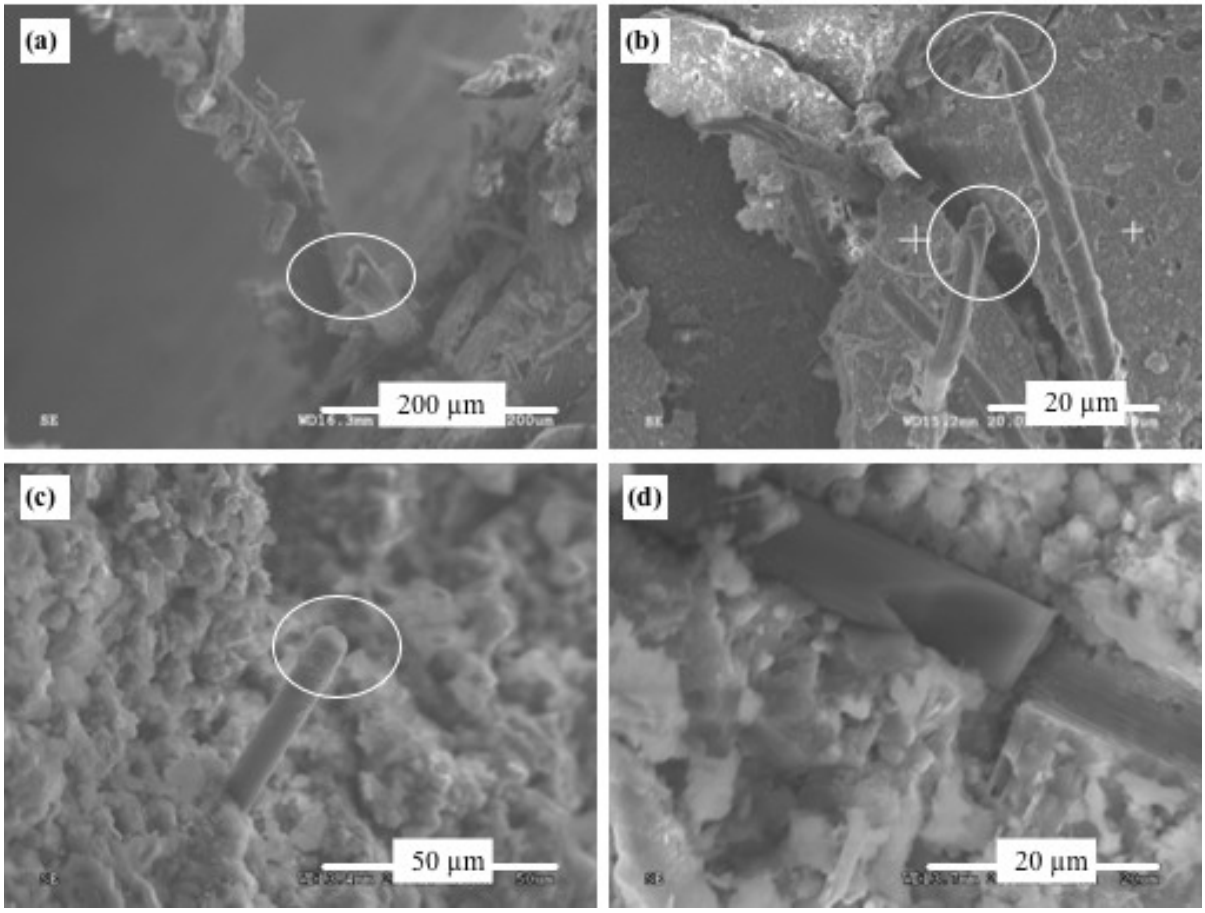

Figure 5-8- Comparison of the fiber ruptured endings of PVA (a,b) and carbon fibers (c,d).

According to Table 5-1 fracture toughness of the C_3S samples reinforced by carbon fibers (liquid phase= methylcellulose solution) is 0.36MPa.$m^{0.5}$. Fracture toughness of the C_3S samples reinforced by PVA fibers is 0.48MPa.$m^{0.5}$ (~33% higher values than CF). Fracture toughness of the C_3S-10MCP samples reinforced by carbon fibers is 0.14 MPa.$m^{0.5}$ and by PVA fibers is 0.22 MPa.$m^{0.5}$ (~57% higher values for PVA). Evidently PVA reinforcement was more effective, which can be explained by the presence of relatively strong chemical bonds between the fibers and the matrix. PVA's simple chemical structure with a pendant hydroxyl group, is assumed to react with metal hydroxide (such as $Ca(OH)_2$) and make a complex cluster [166]. Horikoshi et. al.

assumed that Ca^{+2} and OH^{-} ions in cement slurry might be attracted by PVA and makes $Ca(OH)_2$ layer around the fiber [166].

5.1.3. Validity of NTP tests for PVA reinforced samples

In the previous subsections, NTP test results were reviewed. The NTP test follows the calculations of the chevron notched short rod (CNSR) test [158]. The basis for development of the CNSR test method is linear elastic fracture mechanics and slowly advancing steady-state crack [167]. Such assumptions require samples to have two characteristics: (i) follow linear elastic behaviour; (ii) contain a mono-crack, propagating in one direction (perpendicular to the applied force). The un-reinforced samples and CF reinforced samples were able to hold these assumptions. However, Figure 5-9 schematically shows PVA reinforced samples had multiple cracks and the cracks did not propagate in one direction. Therefore, the fracture toughness results calculated from NTP tests are not strictly valid for PVA-reinforced samples. However, our results suggest significant improvements in the fracture toughness by PVA fibers reinforcement compared to carbon fibers reinforcement. In order to re-evaluate and quantify these results, we switched to three-point-bending tests that will be presented in Section 5.2.

5.2. Three point bend test results

In this section, the results of the Three-Point-Bending (3PB) tests for un-reinforced and reinforced samples are presented. As mentioned in the Section 4.1.3, the 3PB samples were prepared by using PEG-solution as the liquid phase, PEG enhanced homogeneous distribution of the fibers. For each sample, the stiffness and area under the load-displacement curve were calculated. For comparison purposes, we used the area under the load-displacement curve as semi-quantitative indication of material's fracture toughness, in the form of energy absorbed

before failure. We used samples with the same geometry to increase the validity of such a comparison.

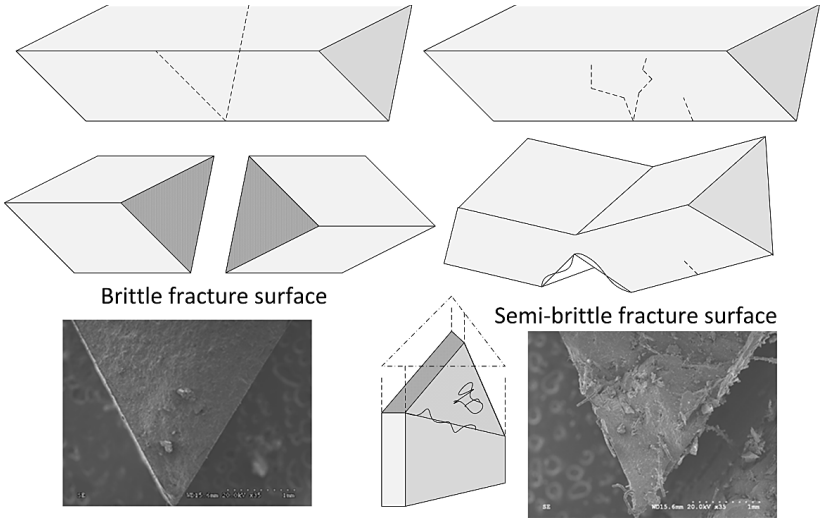

Figure 5-9- Schematic of the brittle and semi-brittle fracture behaviour and SEM images.

Figure 5-10 shows the load-displacement curves of the samples. Table 5-2 summarises the load bearing capacity for all the samples, the average for each set of samples, and their standard deviation. In addition, the area under the load-displacement curve, stiffness (slope of the linear part of load-displacement) and elastic modulus (Equation 5-1) were calculated for each specimen and the average and standard deviation of area, stiffness and modulus are also presented in Table 5-2. In the next subsections, we discuss these results.

$$E = \frac{L^3 m}{4bd^3} \qquad \text{Equation 5-1}$$

Where, L: span length, m: slope of load-displacement curve, b: width and d: thickness of the samples [168].

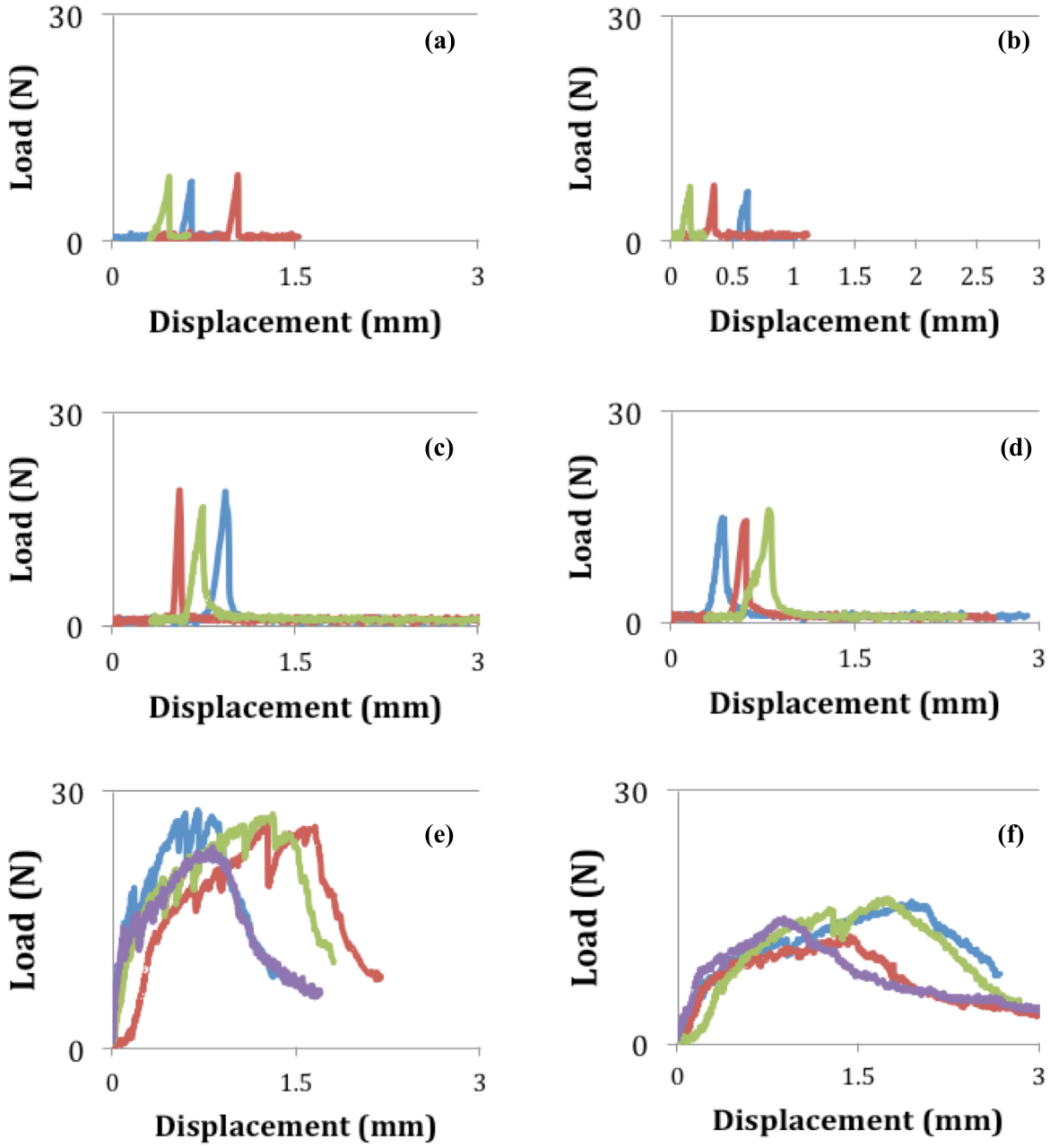

Figure 5-10- Load-displacement curves of three point bending tests of un-reinforced and fiber reinforced C_3S and C_3S-10MCP: a) C_3S, b) C_3S-10MCP, c) C_3S-CF, d) C_3S-10MCP-CF, e) C_3S-PVA, f) C_3S-10MCP-PVA.

Table 5-2- Maximum load capacity, area under the curve and stiffness of the samples derived from load-displacement curves shown in Figure 5-10.

	Max Load	Stiffness	E	Area Under the Curve
	(N)	(N/mm)	(GPa)	(N.mm)
C_3S	8.29 ± 0.36	89.0 ± 7.6	3.22 ± 0.27	0.46 ± 0.07
C_3S-10MCP	6.97 ± 0.33	72.8 ± 11.5	2.63 ± 0.42	0.35 ± 0.01
C_3S-3CF	18.2 ± 1.29	212.4 ± 150.1	7.68 ± 5.43	1.94 ± 0.82
C_3S-10MCP-CF	15.1 ± 0.74	106.5 ± 15.8	3.85 ± 0.57	1.93 ± 0.44
C_3S-PVA	25.6 ± 1.98	111.3 ± 33.8	4.03 ± 1.22	27.5 ± 8.29
C_3S-10MCP-PVA	15.4 ± 2.01	37.8 ± 4.6	1.37 ± 0.17	28.5 ± 3.09

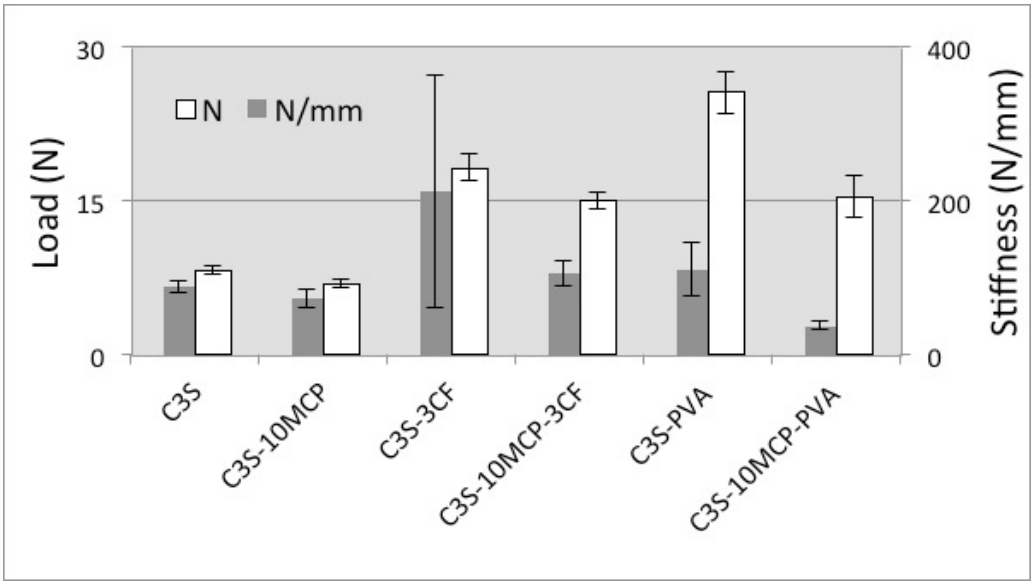

Figure 5-11- Maximum load bearing capacity and stiffness in three point bending test.

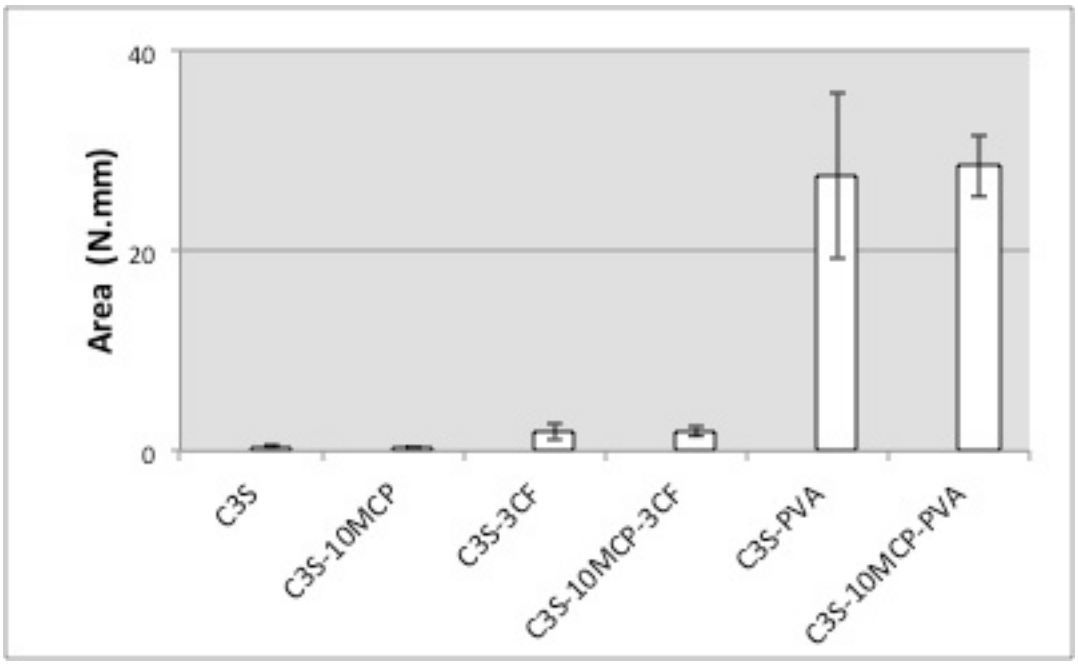

Figure 5-12- Area under the load–displacement curve.

5.2.1. Maximum load capacity of three point bend tests results

To better illustrate the data in Table 5-2, the average of the maximum load capacities for each set of samples, and the average stiffness for each set of samples are shown in Figure 5-11. The error bars show plus-minus standard deviation for each set. The general trend shows samples containing MCP have lower load capacity and lower stiffness. The detailed discussion of these results will be presented in the following sections, after introducing the equivalent flexural strength in Section 5.2.1.1.

5.2.1.1. *Equivalent flexural strength for the maximum load capacity values*

To provide better understanding of the load capacity, we converted the max load capacity values to flexural strength by using conventional formula for a rectangular bar in a three-point-bend test (Equation 5-1).

$$Flexural\ Strength = \frac{3fl}{2bd^2}$$ Equation 5-2

Where, *f*=load, *l*=span length, *b*=width and *d*=thickness of the sample [168]. This equation is valid for materials showing linear elastic behaviour, which is not valid for our fiber-reinforced samples (but valid for unreinforced samples). Therefore, we did not use flexural strength in the presented data table. However, in order to express the meaning of such loads for such geometry, we calculated the "equivalent strength", which will be expressed in MPa unit in the next following subsections.

5.2.1.2. *Maximum load capacity of the unreinforced samples*

According to Figure 5-11 all C_3S-10MCP samples have lower load capacity than their C_3S counterparts in general. Load bearing capacity of the unreinforced C_3S is 8.29± 0.36 N and unreinforced C_3S-10MCP is 6.97±0.33 N. Since they both are brittle materials with linear elastic behaviour, we can calculate the actual flexural strength for them, which will be 8.64 MPa and 7.26 MPa respectively. Compared to ECC samples (flexural strength= 5MPa [4] our samples show significantly higher strength. This can be attributed to the small sample sizes we used. The smaller the sample size, the lower is the chance of defect formation. Likewise, the lower thickness promotes better progress in the hydration process.

Table 5-3 shows results of Archimedes densitometry analysis. C_3S-10MCP samples have higher porosity, which might be responsible for their lower load bearing capacity. In addition, the stiffness of the C_3S-10MCP samples is lower than C_3S (72.8 versus 89.0 N/mm). We may conclude that C_3S-10MCP samples are more porous, possibly due to the excess water released due to MCP reaction with $Ca(OH)_2$.

5.2.1.3. *Maximum load capacity of the reinforced samples*

Figure 5-11 shows C_3S-CF has higher load capacity than C_3S-10MCP-CF (18.2N versus 15.1N) and higher stiffness (212.4±150 N/mm versus 106.5±15.8 N/mm) (Table 5-2 and Figure 5-11). This also can be related to the more porous structure of the C_3S-10MCP matrix. Figure 5-4d shows the porosity in carbon fiber reinforced NTP sample. However, carbon fiber reinforcement has increased load-bearing capacity of both C_3S and C_3S-10MCP matrix more than two-fold.

C_3S-PVA samples had a maximum load of 25.6 N, which is equivalent to 26.7 MPa flexural strength. Similarly, 15.4 N load capacity of C_3S-10MCP-PVA is equivalent to 16 MPa "equivalent strength". PVA fiber reinforcement increased the load bearing capacity of C_3S almost three fold and C_3S-10MCP two fold. These values are significantly higher than the ECC range of flexural strength, which is 5MPa [4,11]. As mentioned previously, this can be attributed to the small sample size. Therefore, we do not claim to have reached much higher strengths than those reported in the literature. However, we have shown that on a small scale (e.g. as a bone cement in small bone defects, such as vertebra) these materials potentially have higher load bearing capacity.

5.2.2. Area under the load-displacement curves

Area under the load-displacement curves is calculated as a comparative indication of toughness and energy absorbed before failure for samples with the same geometry. Figure 5-12 shows the average area under the load-displacement curves for each set of samples.

Carbon fiber reinforcement increased the energy absorbed before the failure of the C_3S samples 4.2 fold (from 0.46 to 1.94 N.mm) and C_3S-10MCP samples 5.6 fold (from 0.35 to 1.93

N.mm). Although the maximum load capacity of C_3S-CF samples is 20% higher than C_3S-10MCP-CF, they have similar values of the area under the load-displacement curves. The visual association of this concept is wider curves for C_3S-10MCP-CF and higher displacement values before failure. In other words, C_3S-10MCP-CF will have less chance for catastrophic failure.

PVA reinforcement increased the energy absorbed before the failure of the C_3S samples 64 fold (from 0.46 to 27.5 N.mm) and C_3S-10MCP samples 80 fold (from 0.35 to 28.5 N.mm). This is a very significant increase, which totally changed the mode of failure of the C_3S and C_3S-10MCP samples, from catastrophic to stable, respectively. Similar behaviour as carbon fiber reinforced samples is observed for PVA fiber reinforced samples. The load capacity of C_3S-PVA is ~66% higher than C_3S-10MCP-PVA (25.6 N versus 15.4 N), but its area under the load-displacement curve is ~3% lower (28.5 versus 27.5 N.mm). The C_3S-10MCP-PVA samples have higher displacement before failure (damage tolerance), and lower stiffness than C_3S-PVA samples. Therefore, the elastic portion of the deformation is higher for the C_3S-10MCP-PVA samples. The slope of load reduction line after the maximum load in C_3S-10MCP samples is lower than C_3S samples, which postpones the sample's failure to higher displacement (deflection) values. Mid-span displacement of 3 mm is equivalent to 8.6% strain for this geometry, based on [169][5]. However the reason for such behaviour in C_3S-10MCP-PVA samples is unclear. As mentioned in the literature review, MCP might be reacting with $Ca(OH)_2$ to produce hydroxyapatite and water. Lower load capacity might be explained by water formation in such reaction. When water either reacts with remnant C_3S particles or is removed during drying, it leaves behind porosity. This can explain higher porosity, determined by

[5] - The strain is calculated based on this formula: $6Dd/L^2$[169], where d=3mm, L=25mm, D=mid-span deflection. However, we are aware that the assumption of linear elastic behavior and continuity of the samples are not met by our samples.

densitometry in Table 5-3 for C_3S-10MCP samples and lower load bearing capacity of the C_3S-10MCP samples rather than their C_3S counterparts.

Finally, our three point bending results suggest PVA fiber reinforcement is an appropriate method to increase toughness and change the catastrophic failure mode of the C_3S and C_3S-10MCP cements, as well as increasing flexural load bearing capacity of both sets of samples. In addition, C_3S-10MCP-PVA samples showed high values of deflection before failure that can be equivalent to 7% strain. The fact that they can withstand very large strains before failure might be especially useful for a field such as bone cements, to prevent catastrophic and sudden failures.

Table 5-3 – Density and porosity of the C_3S and C_3S-10MCP samples (10 days set in water) by Archimedes method.

	% Density	%Total Porosity	% Open Porosity	% Closed Porosity
C_3S	62.3±0.83	37.7±0.83	21.6±0.98	16.1±0.66
C_3S-10MCP	54.6±1.18	45.4±1.21	31.3±1.20	14.1±0.40

5.3. Compressive strength

In this section, results for the compressive strength of the samples are presented. Compressive strength of the C_3S and C_3S-10MCP composites (un-reinforced, carbon fiber and PVA fiber reinforced) are listed in Figure 5-13 and Table 5-4. We used three different liquid phases: Pure distilled water (W), methylcellulose solution (similar to NTP sample preparations), and PEG solution (similar to 3PB sample preparations). The details of liquid phase selection are presented in Materials and Methods section.

5.3.1. Compressive strength of unreinforced samples

According to the Figure 5-13, the highest compressive strength of unreinforced C_3S samples was gained by using methylcellulose solution as the liquid phase. Unreinforced C_3S sample with methylcellulose solution had compressive strength as high as 74.2 MPa, while choosing water as liquid phase resulted in 51.0 MPa compressive strength and PEG solution resulted in 47.3 MPa.

Unreinforced C_3S-10MCP compressive strength is 51.0, 58.5 and 47.3 MPa for water, methylcellulose solution, and PEG solution respectively. C_3S-10MCP with methylcellulose solution, as shown by NTP test results is extremely brittle (K_{IC}=0.01 MPa.m$^{0.5}$) and cannot even withstand de-moulding stresses during three-point-bending sample preparations. However, C_3S-10MCP samples, prepared with methylcellulose solution as liquid phase, have 58.5 MPa compressive strength. Therefore, we conclude that the C_3S-10MCP samples with methylcellulose solution liquid phase have very low strength. The exact method of methylcellulose to increase brittleness and strength of C_3S-10MCP samples is not known. It might alter the reaction between MCP and $Ca(OH)_2$ by producing a layer around one of the reactants and inhibit the reaction. If MCP particles do not react with the matrix to form strong bonds to the other component of the composite, they might act as occlusions and produce stress concentration areas. However, this is just a possible explanation and further studies needed to approve or disapprove.

5.3.2. Effect of fiber reinforcement on the compressive strength

Our results show that the highest compressive strength was 134.9 MPa, it was observed in C_3S-CF samples prepared by methylcellulose solution as the liquid phase. The second highest strength was 110.4 MPa for C_3S-10MCP-CF and methylcellulose solution as the liquid phase. They have shown 82% and 89% growth in the compressive strength respectively, compared to

the non-reinforced sample with the same liquid phase. Carbon fiber reinforcement increased the compressive strength of the C_3S samples prepared by water from 54.8 MPa to 83.6 MPa (53% increase). Similarly, for C_3S-10MCP samples prepared with water as the liquid phase, carbon fiber reinforcement increased compressive strength from 51.0 MPa to 88.7 MPa (74% increase).

C_3S-CF samples prepared by PEG solution as the liquid phase have almost half the compressive strength of the C_3S-CF samples prepared by methylcellulose solution. Comparably, C_3S-10MCP-CF samples prepared by PEG solution as the liquid phase have 36% less compressive strength than the C_3S-10MCP-CF samples prepared by methylcellulose solutions. The reason could be that the only mechanism of fiber/matrix interaction for CF samples is mechanical interlocking [165]. PEG might act similar to oiling agents in ECCs to reduce fibre/matrix bond strength [4] and reduce the friction and mechanical interlocking of carbon fibers and the matrix.

Unlike C_3S-CF and C_3S-10MCP-CF samples, in PVA reinforced samples, compressive strength using PEG solution as the liquid phase showed higher values than using methylcellulose solution. C_3S-PVA when prepared by PEG solution (108.2 MPa) was 6.4% higher than C_3S-PVA when prepared by methylcellulose solution (101.3 MPa). Likewise, C_3S-10MCP-PVA when prepared by PEG solution (89.3 MPa) was 16.6% higher than C_3S-10MCP-PVA when prepared by methylcellulose solution (74.5 MPa). This observation might be described as follows: PEG molecules slightly reduced the bond strength of PVA fiber and the matrix as space inhibitors, or oiling agents. Therefore, fiber de-bonding and fiber pull-out mechanisms became more active and increase toughening of the samples. Li et. al. used a similar approach by introducing an oiling agent to slightly reduce the chemical bond between PVA and cement in order to add the fiber pull-out mechanisms instead of pure fiber rupture [4].

As a summary, the highest compressive strength was gained by using methylcellulose and carbon fiber reinforcement. However, using methylcellulose solution although increased the compressive strength, but decreased the toughness of the samples. PVA fiber reinforcement by using PEG solution as the liquid phase increased compressive strength to higher than 100 MPa (although not as high as C_3S-CF-Methylcellulose: 135 MPa).

Addition of MCP to the cement decreased the compressive strength compared to their C_3S counterparts, probably because of higher porosity in the samples. However, adding PVA fibers increased the C_3S-10MCP compressive strength from 47.3MPa to 89.3MPa (%74 increase).

Table 5-4- Compressive strength of un-reinforced and fiber reinforced samples, processed using different liquid phases.

Liquid Phase	Water	Methylcellulose	PEG
C_3S	54.8±1.2	74.2±5.0	59.1±7.0
C3S-10MCP	51.0±9.3	58.5±11.1	47.3±9.2
C_3S-CF	83.6±10.9	134.9±16.7	72.9±11.5
C_3S-10MCP-CF	88.7±11.2	110.4±12.2	70.4±15.0
C_3S-PVA	NA	101.3±4.4	108.2±4.2
C_3S-10MCP-PVA	NA	74.5±6.6	89.3±5.1

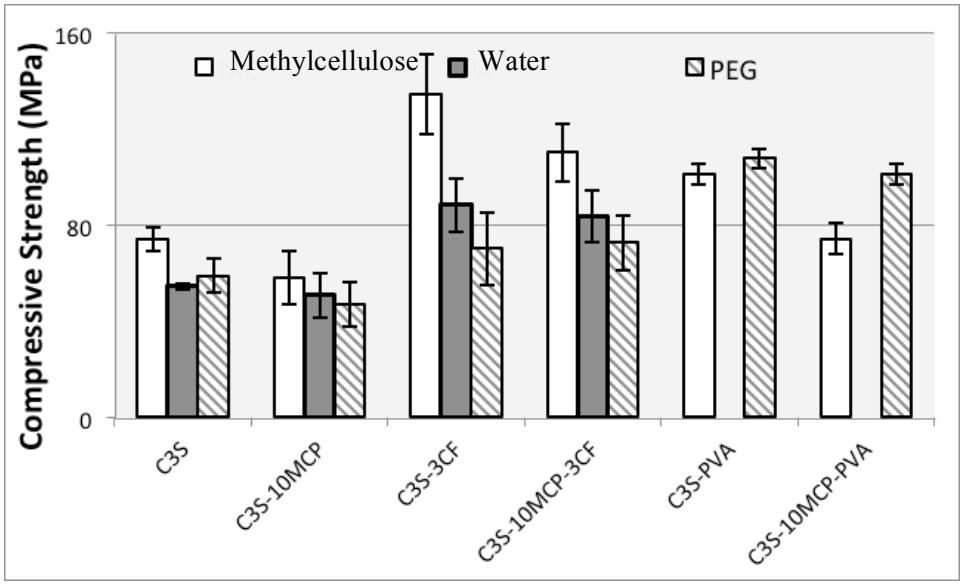

Figure 5-13- Compressive strength of the cement samples and the effect of different liquid phases.

5.4. Summary

According to the presented results of NTP, three point bending and compressive strength tests, in addition to microstructure and EDX analysis, the following conclusions were derived:

- Hand-mixing, in combination with using PEG/distilled water solution as the liquid phase is an effective method to disperse PVA fibers in the C_3S and C_3S-10MCP matrix. PEG can modify the fiber/matrix interface (similar to the effect of oiling agents in ECC fiber/matrix interface tailoring [4] and simultaneously increases strength and toughness of the composite. These composites showed strain-hardening behaviour.
- Evidence of chemical bond between PVA fibers and both the C_3S and C_3S-10MCP matrices was observed (Section 5.1.2.2). The fractured surface images, in which the fibers were covered by the matrix particles, indicated the bond between fiber/matrix were

stronger than the bond between matrix particles together. Plastically deformed and dented fibers were further signs of the strong chemical bond between the fiber and the matrix.

- PVA fiber reinforcement increased the work of fracture up to 60 times, compared to plain C_3S samples and more than 80 times compared to plain C_3S-10MCP samples. Such significant improvements, as confirmed by the microstructure analysis, were based on the activation of three different mechanisms of toughening: fiber-bridging, fiber-pull-out and plastic deformation of the fibers.
- The maximum load capacity in three-point-bending (3PB) for samples with 3x4mm cross-section was achieved by PVA reinforcement. The values were 25.6 N for C_3S-PVA and 15.4 N for C_3S-10MCP-PVA, equivalent to 26.7 MPa and 16 MPa respectively.
- PVA fiber reinforcement has almost doubled the C_3S compressive strength (liquid phase: PEG solution) from 59.1 MPa to 108.3 MPa and from 47.3 MPa to 101.3 MPa for C_3S-10MCP.
- The maximum possible compressive strength gained by the C_3S-CF-Methylcellulose samples was as high as 134.9 MPa. Carbon Fiber reinforcement increased work of fracture in C_3S samples 4.4 times and 5.5 times in C_3S-10MCP samples. The maximum load capacity in 3PB test doubled for both C_3S and C_3S-10MCP samples, by carbon fiber reinforcement.
- Methylcellulose in the liquid phase increased the compressive strength of the C_3S-CF samples. However, this is not compatible with the C_3S-10MCP samples; although it increases the compressive strength, the samples become too brittle. For non-reinforced C_3S-10MCP prepared with methylcellulose solution, the samples were so weak that de-moulding them without shattering them was almost impossible.

- Adding 5 wt% PEG200 to the distilled water in the liquid phase reduced the compressive strength of the CF reinforced samples. The most important toughening mechanism of CF-C_3S is fiber pull out and the fiber/matrix interface is merely physical bonds and mechanical interlocking. PEG might have decreased friction between CF and the matrix, therefore reducing the only interaction mechanism: mechanical interlocking.
- Addition of 10 wt% MCP in to the C_3S matrix decreased their flexural load capacity and compressive strength. The load-deflection curves of samples containing MCP, has broader peak and higher strain before failure. The C_3S-10MCP-PVA composites withstood as high as 7% strain before failure. The area under the load displacement curve of C_3S-10MCP-CF is similar to C_3S-CF. The area under the load-displacement curve of the C_3S-10MCP-PVA is slightly higher than C_3S-PVA.

6. C_3S-PVA Self-Healing

Prior to study crack self-healing, a methodology for producing stable cracks in the cement samples was required. It was previously demonstrated that PVA fiber reinforcement is an effective method to increase toughness of C_3S based composites to enable them withstand micro-sized stable crack formation (see the details on the fracture toughness and strength of the composites reported in Chapter 5). Therefore, C_3S-PVA composites (with PEG dispersant solution as the liquid phase) are used to study the healing behaviour of stable cracks. The microstructure and mechanical behaviour of the cracked samples were characterized before and after the healing treatments. Section 6.1 of this chapter presents the details of the pre-cracking process. The following sections focus on the mechanical behaviour (Section 6.3), macro and microstructure analysis (Section 6.2, 6.4), and chemical and phase composition of the pre-cracked samples before and after the healing treatments (Section 6.5). The last subsection combines these results and proposes the hypothesis for the healing mechanisms in C_3S-PVA composites exposed to simulated body fluid (Section 6.6).

6.1. Pre-cracking process

We used Three-Point-Bending (3PB) test as a tool to produce stable cracks in the samples and semi-quantify mechanical healing. The 3PB method used in the section was the same as the 3PB test described in Chapter 5, except that the test stopped after substantial amount of stable cracks were introduced, and before total failure of samples. Section 6.1.1 presents the stopping criteria for pre-cracking and Section 6.1.2 presents the steps necessary to ensure meeting these criteria.

6.1.1. Stopping criteria to pre-crack the samples

To facilitate defining the damage-stop criteria, we used an approach similar to that reported by Fantalli et. al. for ECC [170]. The schematic 3PB load-displacement curve of the samples, divided into three stages, is presented in Figure 6-1a. At stage (I), the samples show linear elastic behaviour. At stage (II), they show Pseudo Strain Hardening behaviour (similar to ECCs [171]. In most of the samples significant load fluctuations were observed (shown as multiple peaks in the graph), due to the formation of multiple cracks. At stage (III), the bridged fibers rupture, micro-cracks start to propagate in the direction of the applied load and link to a macro-crack, which propagates until total failure of the sample (unless loading stops). Figure 6-1b shows the schematic microstructure of the sample in stage II. The mechanisms, which prevent crack propagation as shown in Chapter 5, are fiber bridging, fiber pull-out, and plastic deformation of the fibers. The cracks at this stage are 20-100 μm wide (micro-cracks) and are oriented in different directions. Figure 6-1c shows the schematic microstructure of the samples in stage III.

In prior self-healing studies on the ECCs [172,173], researchers performed the healing treatment by stopping the loading at stage II. They then, compared the results for the healed samples to the control samples, which were kept at the same conditions without pre-cracking. Preferably, we should have studied the crack healing behaviour, by a similar method that was carried out on ECCs [172,173] and stopped the test in stage (II). However, according to the 3PB results presented in Chapter 5, the maximum load capacity of different samples varied around 10%, and the maximum displacement before the failure varied more than 25%. Therefore, the high variation in the data prevented us from accurately determining the maximum load capacity of the samples. Consequently, it was difficult to distinguish the changes in the behaviour of the

samples that have undergone healing treatment, without knowing the exact behaviour of the original samples. We further pilot-tested this experimental approach for two samples shown in Figure 6-2. For these samples, loading was stopped at stage II, at deflection=0.8 mm, equivalent to 2% strain[6] (continuous line), the healing treatment applied, and then the same samples re-loaded (dashed line). In this approach, it was not possible to distinguish the increase in the load caused by the healing treatment, from the possible increase of loading of the original sample in stage II. Therefore, for all subsequent tests we decided to stop the test in stage III, determine the maximum load capacity of the sample, and then compare the "after-healing" treatment behaviour of each sample with that known maximum load capacity determined before healing.

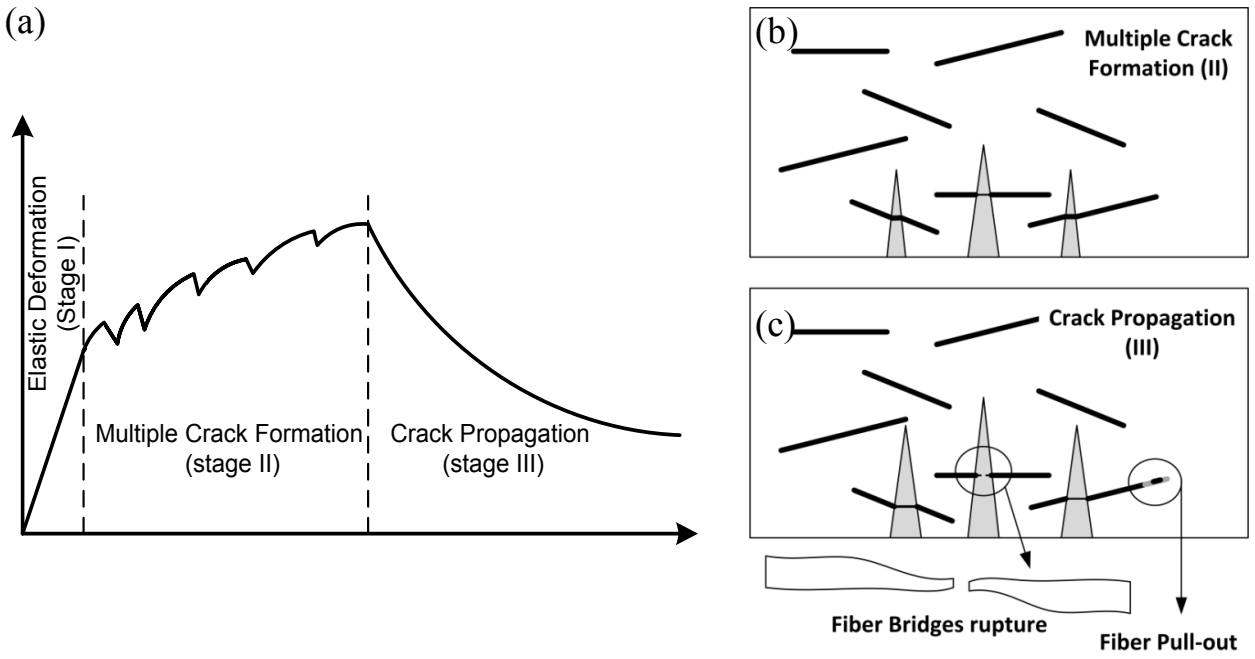

Figure 6-1- (a) Schematic of C_3S-PVA composite cement sample behavior in three point bending test. (b,c) schematic of the damaged material microstructure, showing fibers responsible for the macro-scale behavior of the composite in the regions II and III respectively.

[6] - Calculation was conducted based on rectangular rod formula, $\varepsilon = 6Dd/L^2$. We are aware that this formula is valid for materials with linear elastic behaviour, which obviously is not met by our samples. However, the calculation provides an estimation of the relationship between geometry and the presented deflection of the sample.

This approach can compare the maximum load capacity of each individual sample with itself (i.e. the same sample tested before and after the healing treatment), rather than comparing it to a set of control samples. In addition, this approach eliminates or reduces the effect of operator-dependant variations in the maximum load capacity, occurring in the preparation process for our samples.

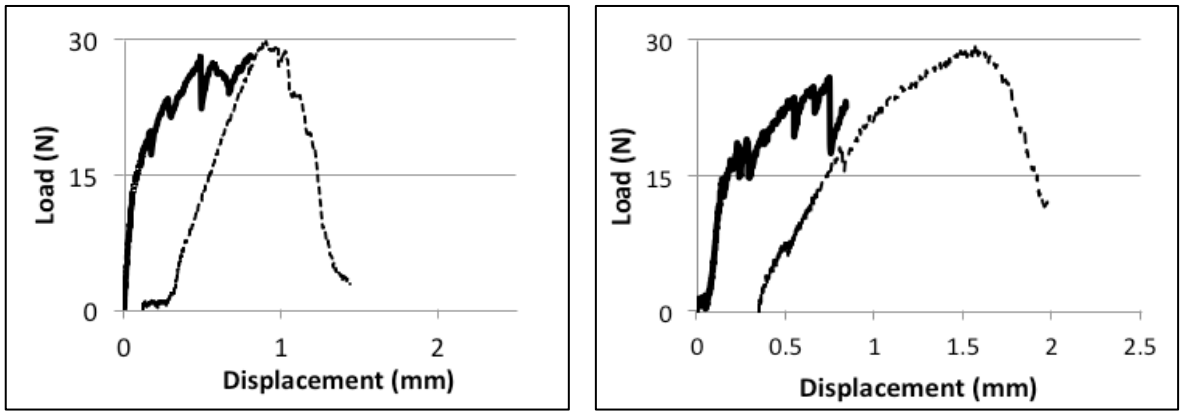

Figure 6-2- Examples of two samples of C_3S-PVA composite, wherein the 3PB test was stopped at stage II (continuous line), and then samples underwent the healing treatment followed by re-loading (dashed lines). The effects of the healing treatment are difficult to assess and quantify, as the maximum load carried by the original (un-healed) samples is unknown.

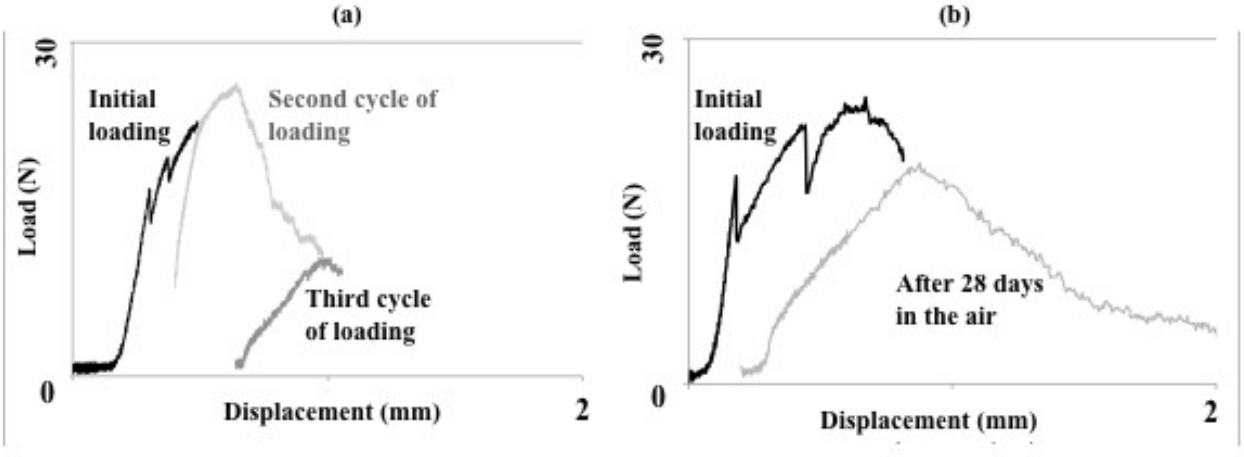

Figure 6-3- 3PB results of C_3S-PVA: (a) stopped at stage II, reloaded immediately (second cycle), then stopped at stage III and re-loaded (third cycle); (b) stopped at stage III and re-loaded after keeping 28 days in the air.

Figure 6-3a shows the results of a 3PB test, where the samples was loaded (first cycle of loading); test was stopped in stage II and re-loaded immediately (second cycle of loading); Then test was stopped in stage III and re-loaded immediately (third cycle of loading). In both second and third cycles, the curve was the continuum of the original curve. Figure 6-3b shows when the test was stopped in stage III; the sample re-loaded after 28 days setting in the air and at room temperature[7]. In both cases, no significant change was observed in the maximum load capacity.

6.1.2. Steps necessary to ensure meeting defined pre-cracking requirements

The challenge of stopping the test in stage III was the formation of multiple cracks and consequently, multiple peaks in the load-displacement curves as schematically illustrated in Figure 6-1 and for the initial pilot tests in Figure 6-2. Each of these local peaks consists of two parts: ascending part and descending part (crack propagation and arrest). If we stop the test when the load starts to decrease (i.e. in the descending part, as shown by an arrow in Figure 6-1), there is a possibility that the load will start raising again. It means the toughening mechanism, e.g. fiber bridging, is activated and stopped the crack propagation. Therefore, we had to define criteria for reaching the maximum load capacity and stopping the test in stage III. We could not use the maximum displacement criteria to stop the tests, since according to the results in Chapter 5, displacement associated with the maximum load capacity had a wide range of 0.7 mm -1.3 mm, equivalent to 2.0 - 3.7% strain. Two practical criteria to ensure reaching the maximum load capacity of the sample were defined as follows: (i) consistent decrease in the load (for over 0.2 mm displacement); and (ii) formation of macro-crack (width of the crack higher than 150-200 μm, often visible by eye on the sample surface during the test). This method allowed obtaining the maximum load capacity of each individual sample, and then to compare it with the value

[7] - Setting times less than 28 days is called early hydration time for Portland cements, after which less dramatic changes in the hydration progress and consequently in the strength will be observed [76].

obtained after the healing treatment. Details of such comparisons and semi-quantifying the mechanical self-healing will be demonstrated in Section 6.3. Semi-quantifying results were provided for samples with splints (see details on Section 4.2.3.4).

6.2. Macrostructure analysis of the healing treatment effect on the cracked samples through optical microscope images

This section reports studies of the macrostructure of the stable cracks in the C_3S-PVA composites, before, during and after healing. Optical microscope (OM) imaging was used to observe the cracked samples immediately after pre-cracking them by 3PB, as SEM would require additional sample preparation precluding them from subsequent healing experiments. To induce the healing process, the samples were soaked in either water or SBF for 7 days at 37°C and we then observed the cracks after the treatments. Figure 6-4 shows relatively low-magnification (10 x) optical microscope images of C_3S-PVA samples, before and after soaking 7 days in distilled water. Figure 6-5 shows images for the samples soaked in SBF prepared as described previously in Section 4.1.3.

As shown in Figure 6-4 and Figure 6-5 the cracks in the samples soaked in SBF are partially eliminated. On the other hand, no significant difference in macro-scale was observed in the cracks of samples soaked in water. In self-healing of ECCs, authors did not report any mechanical effects of healing for 3% pre-strained samples [172], which were soaked in water (they are similar to our results). However, we observed substantial crack elimination in SBF but not in water. Subsequently, we reloaded the samples in 3PB and compared the results with the initial loading records. Restoration in the loading capacity was not observed in the samples soaked in water nor in SBF. For the samples soaked in SBF, elimination of the cracks seen in optical microscopy images, without any restoration of mechanical properties might be explained

by: i) There is only a thin layer of deposits covering the crack mouth, where the tip of the crack is not affected and has high stress concentration; ii) The deposits are formed all the way inside of the crack, but they consist of loose particles without having any chemical bonds to each other; iii) The increased load capacity caused by the healing is cancelled by the deterioration of the sample in the SBF environment; iv) The crack was wider than the maximum limit of the healing mechanism, similar to healing limitation of natural tissues, e.g. natural bone cannot heal large defects.

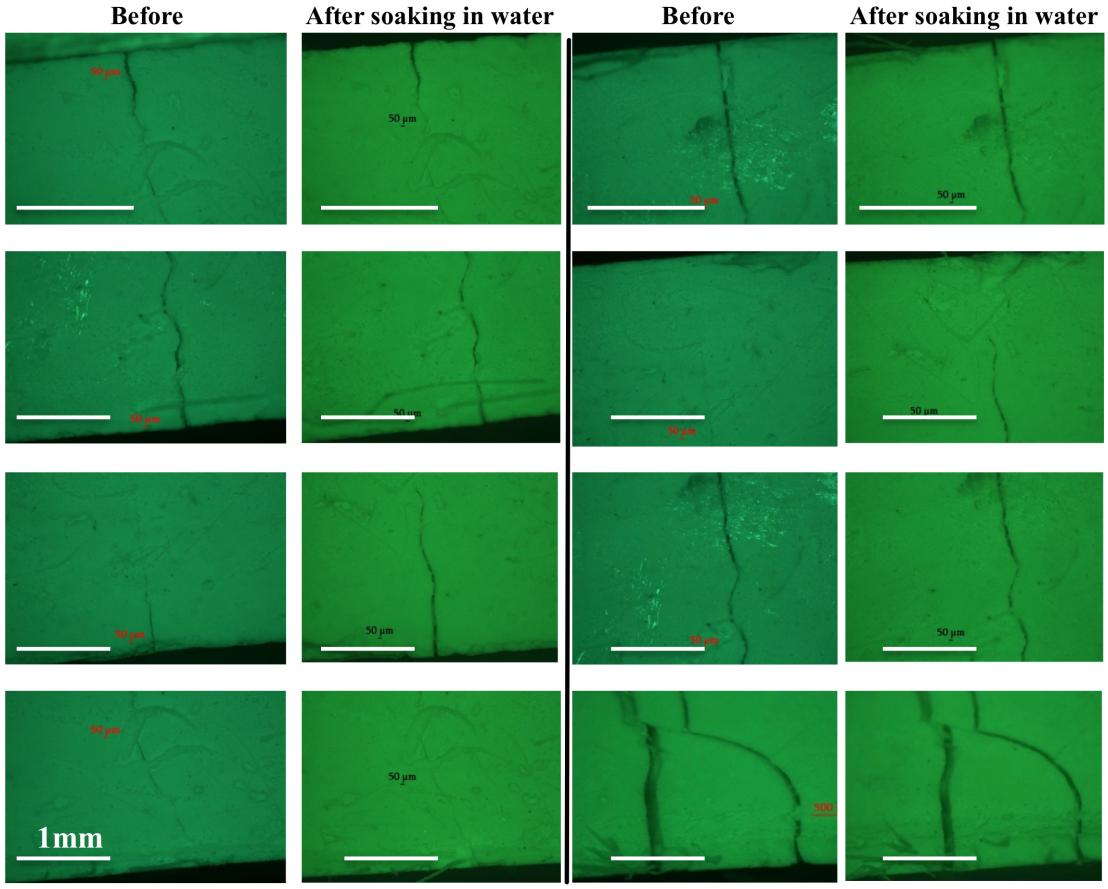

Figure 6-4- Low-magnification (10x) optical microscope images of the pre-cracked samples before and after soaking for 7 days in water (without splint).

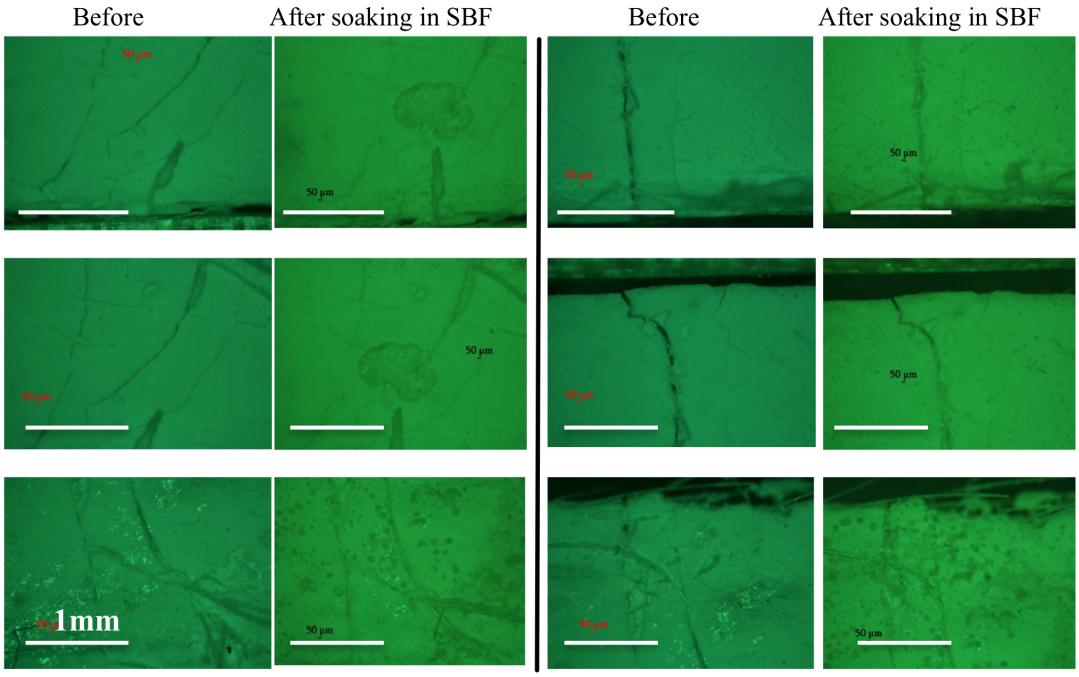

Figure 6-5- Low -magnification (10x) optical microscope images of pre-cracked samples before and after soaking 7 days in SBF (without splint).

In order to better understand the responsible cause(s), we reviewed the limitations available for ECC healing. In ECCs, the size of the crack mouth opening (δ) or width is usually smaller than 50-60 µm for the range of the strains used in Yang et. al. studies [173]. They showed that if $\delta < 50$ µm, then the samples will show full recovery. If 50 µm $< \delta <$150 µm then there is partial recovery, if $\delta >$150 µm then there would be no recovery [172,173]. The crack width obtained in our samples was in the range of 10-200 µm, where at least one crack larger than 150 µm was typically present in the sample. This might explain why no restoration of the maximum load capacity in 3PB tests was attained. However, Yang et. al. reported partial restoration of mechanical properties in 3% pre-strained samples, through wet/dry cycles [172]. Samples soaked in water without drying showed no improvement in the mechanical properties for such strain (3%) [172]. These 3% pre-strained samples soaked in water are similar to our samples soaked in water, for which we also did not observe mechanical effects of healing.

Whereas for structural ECC materials (not intended for underwater applications) the assumptions of wet/dry cycles is rational, bone cements are designed for lifelong contact with body fluids, so our experimental design of the healing treatment (Section 4.1.3) appears more suitable. Therefore, a method to reduce the crack width was introduced by means of a rod attached to a sample (called "splint", see Figure 4-6). This approach and philosophy is somewhat similar to the splints used for immobilization of human bone fractures. If a bone breaks dramatically and/or the defects are large, a splint can be used to stabilize the movement and orient the bone to its natural alignment; on a micro-scale, splints would also help to close the crack mouth in the fractured bone. Therefore, after pre-loading the samples, we unbend the samples to close the crack width to less than 100 μm, with the use of splints (Figure 4-6).

Figure 6-6 and Figure 6-7 shows the optical microscope images of the samples with splint, before and after soaking in SBF and water.

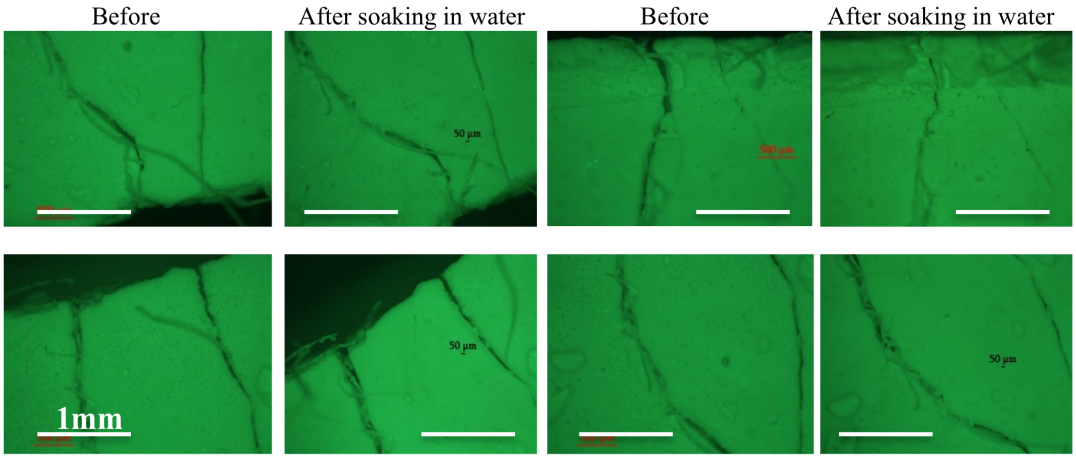

Figure 6-6- Low -magnification (10x) optical microscope images of pre-cracked samples before and after soaking 7 days in water (with splint).

According to Figure 6-6, the samples with splint soaked in water show somewhat better healing ability than samples without splint, i.e. partial eliminations of the cracks is clearly seen in OM images. However, they still showed deterioration in the load capacity (Figure 6-10). According to Yang et. al. the partial healing visible in the sample microstructures should result in improved mechanical properties for the 0.3% pre-strained samples soaked in water [172]. This suggests that healing in this type of composite cements is effective only for "slightly" damaged samples (in contrast to our samples, which are "dramatically" damaged over their maximum load capacity point). At this stage of this pioneering research on the healing of toughened bio-cements, it is difficult to quantify the "slight" damage, which could respond to the healing treatment. However, the results presented in the subsequent sections of this chapter provide further evidence, which could resolve this issue in the future.

The samples soaked with splint in SBF showed crack elimination and healing (Figure 6-7 and Figure 6-8). Smaller cracks are completely eliminated and larger cracks are partially healed. They also showed partial mechanical restoration of their maximum load capacity, which will be presented later in Figure 6-11. Details of the definition and quantification of mechanical healing are presented in Section 6.3.

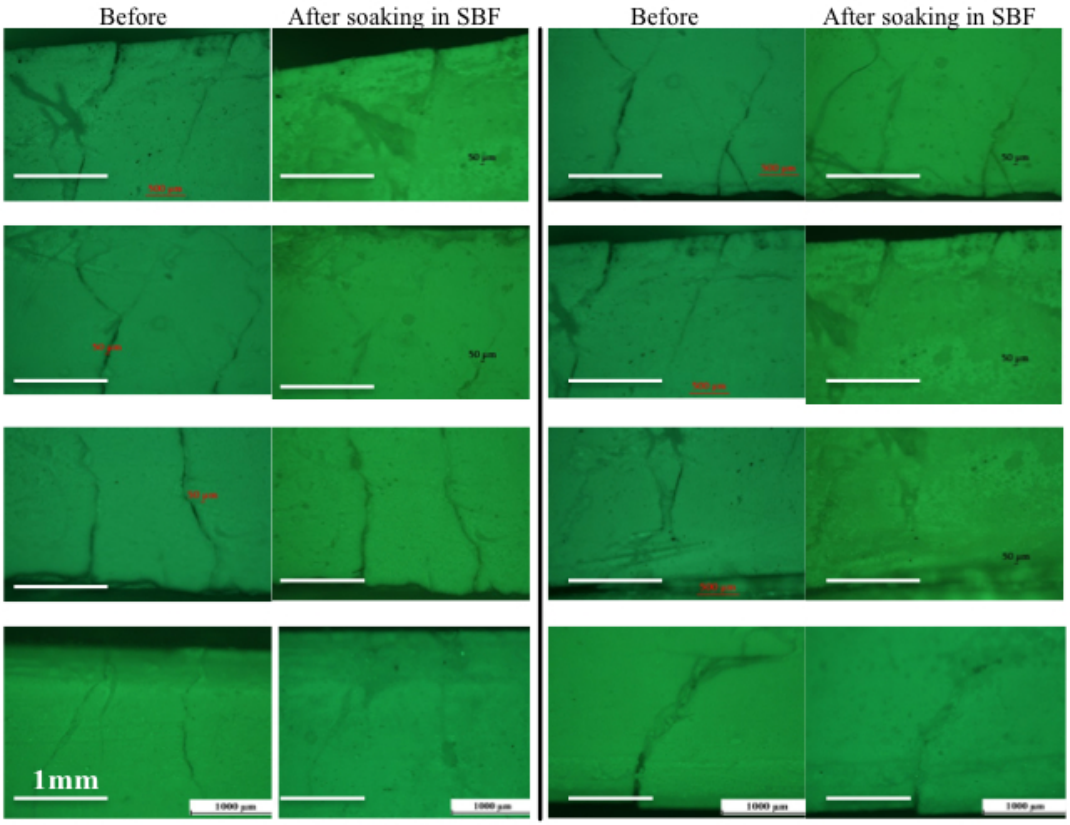

Figure 6-7- Low magnification (10x) optical microscope images of pre-cracked samples before and after soaking 7 days in SBF (with splint).

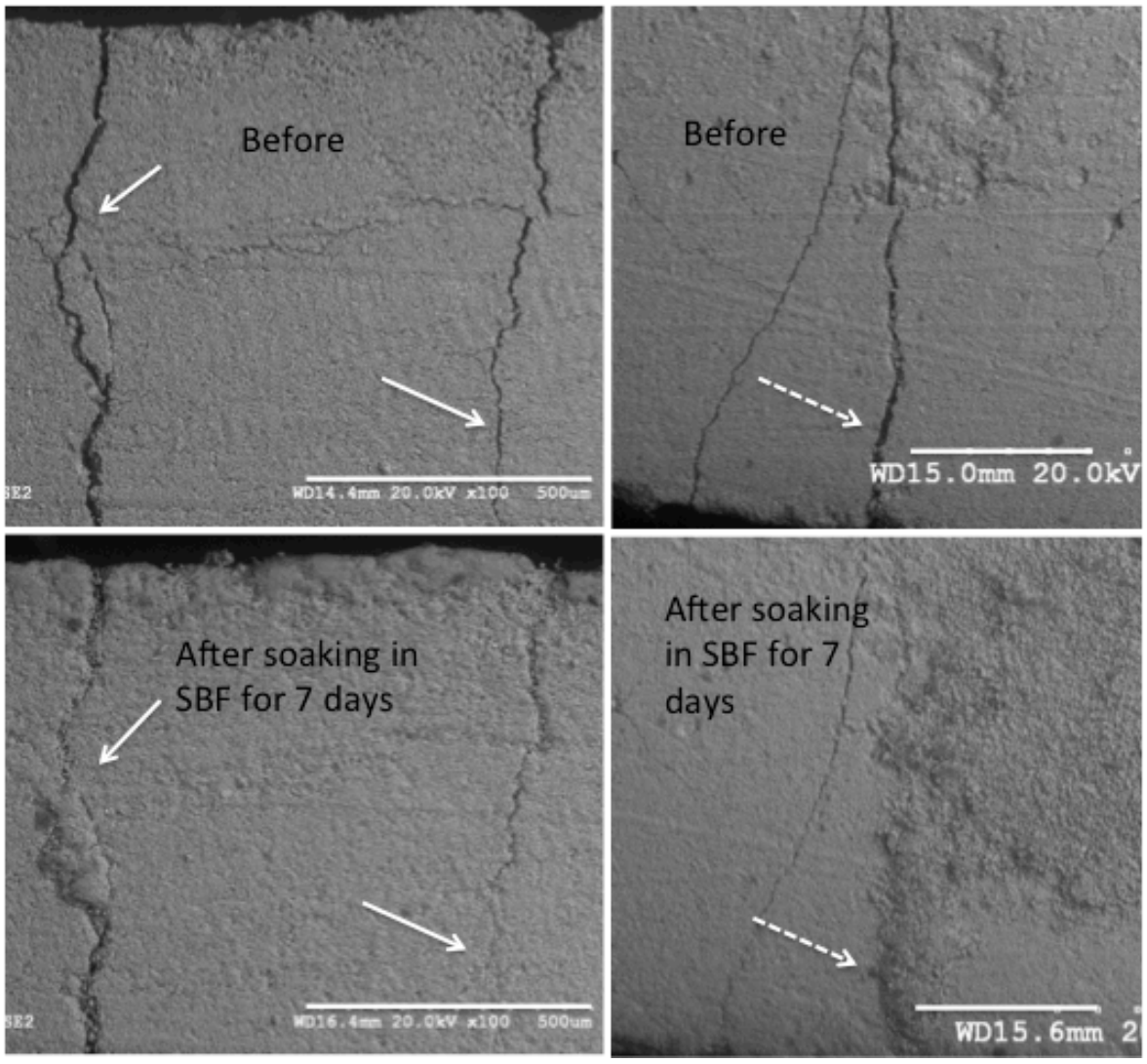

Figure 6-8- Low magnification (100x and 50x) SEM images of pre-cracked samples before and after soaking 7 days in SBF (with splint, scale bar is 500 μm).

6.3. Semi-quantifying the restoration of load capacity by the healing treatments

In this Section we demonstrate a semi-quantifying method to evaluate restoration of load carrying capacity in the 3PB test.

Figure 6-7 showed the optical microscope images of the crack healing. While crack "repair" was observed by soaking in SBF, it was important to quantify how much healing is attained in terms of load carrying capacity restoration. Thus, this Section presents the methodology to semi-quantify the healing behaviour of the samples in three point bend test.

The Healing index (H) is defined to quantify healing, Figure 6-9. If the sample is totally healed, it should yield the same load-carrying capacity as the original sample. Therefore, if the maximum load L after healing (load at point C, or L_C) is the same as the maximum load carried by the original sample (load at point A, or L_A), we define it as "total healing" (or %100 healing). A %100 healed sample behaves in 3PB as if it reset to the original load-carrying capacity. If no change occurs in the sample during the healing treatment, it behaves as if reloaded immediately after stopping the load. It rises up to the point that the loading was stopped (load at point B, or L_B), and then follows the continuum of the original curve. We define this type of load-carrying behaviour as no healing (%0 healing). Therefore, L_B=L_C yields 0% healing and L_c=L_A yields 100% healing. Therefore, the dimensionless healing index H is defined in Equation 6-1, as the ratio of the difference between the peak (or "maximum") load and the "damage-stop-load" for non-healed sample, "L_A-L_B", to the difference between the peak load for the healed sample and the damage-stop-load for non-healed sample, "L_C-L_B":

$$H = \frac{(L_C - L_B)}{(L_A - L_B)} \times 100 \qquad \text{Equation 6-1}$$

If the maximum load after soaking is lower than the stop point (L_C<L_B), H yields negative values, which shows deterioration of the sample during the healing process. If (L_C-L_B)> L_A-L_B then H>100, and the sample is strengthened by the healing treatment. We are aware of the limitation of such definition, as H values vary significantly with L_A-L_B. More discussion in this regard can be found in Section 7.1. The microstructural changes, which may lead to these values of H are discussed in Section 6.4.

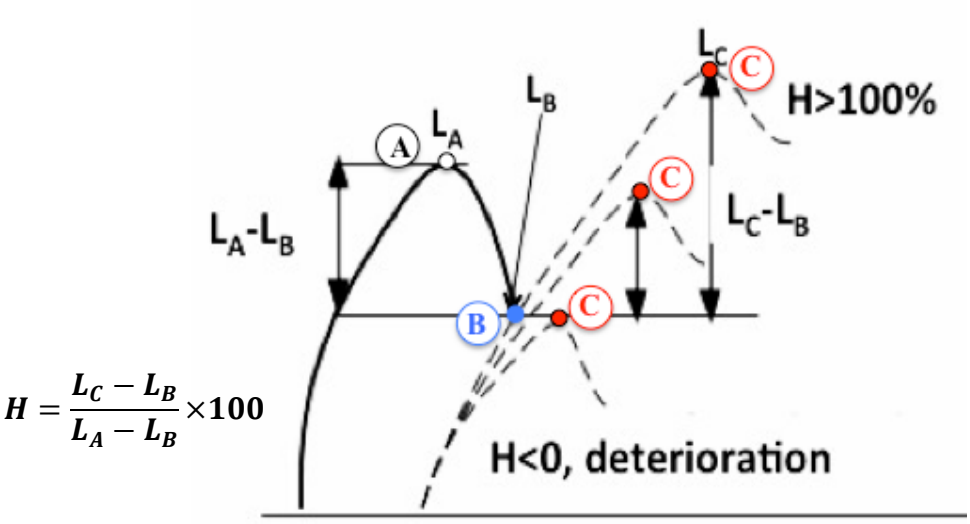

Figure 6-9 - Illustration of the Healing Index (*H*) calculation from a typical three-point-bend (3PB) load-displacement curve (A maximum load of the original sample, B stop load for the original sample, C maximum load after healing treatment).

Figure 6-10a,b,c,d show the effect of soaking the C_3S-PVA samples in water, on the healing index. All samples showed deterioration of the load bearing capacity (i.e. negative *H*). Based on the literature, increasing the setting time for calcium silicate based cements will increase the hydration progress and thus increase the strength of the cement [76,174]. Soaking the samples in water increases the strength of un-cracked samples. On the other hand, when they are pre-cracked the soaking appears to deteriorate their load bearing capacity, Figure 6-10. One possible explanation for this deterioration effect could be the precipitation of calcium carbonate. Formation of the carbonate phase causes 4% volume increase in Portland cement [175]. The volume increase, in particular at the tip of the crack, can increase the internal stress concentration and thus assist propagation of the crack when re-loading. In samples soaked in SBF, we also observed calcium carbonate precipitation. Therefore, the "true" healing in SBF might be *H* in addition to the loss of load capacity in water.

Figure 6-11a,b,c,d,e show the 3PB results of the samples with splint, soaked in SBF for 7 days. The figures show reproducibility of 5 samples prepared and tested in identical way. They all showed partial healing of load carrying capacity (average *H*= 49%), although the values of *H* vary for different samples (34-66%) (see Section 7.1). This shows that there are some other active healing mechanisms in SBF, aside from the active healing mechanisms proposed for ECCs in water [9] as the samples in water were not able to restore load capacity in similar conditions. By increasing the soaking time in SBF to 28 days (Figure 6-12), some of the samples showed total healing (more than 100%), and some showed partial healing. To better understand the healing mechanisms, we carried out microstructure analysis and EDX, XRD and FTIR studies, which will be presented in the following sections.

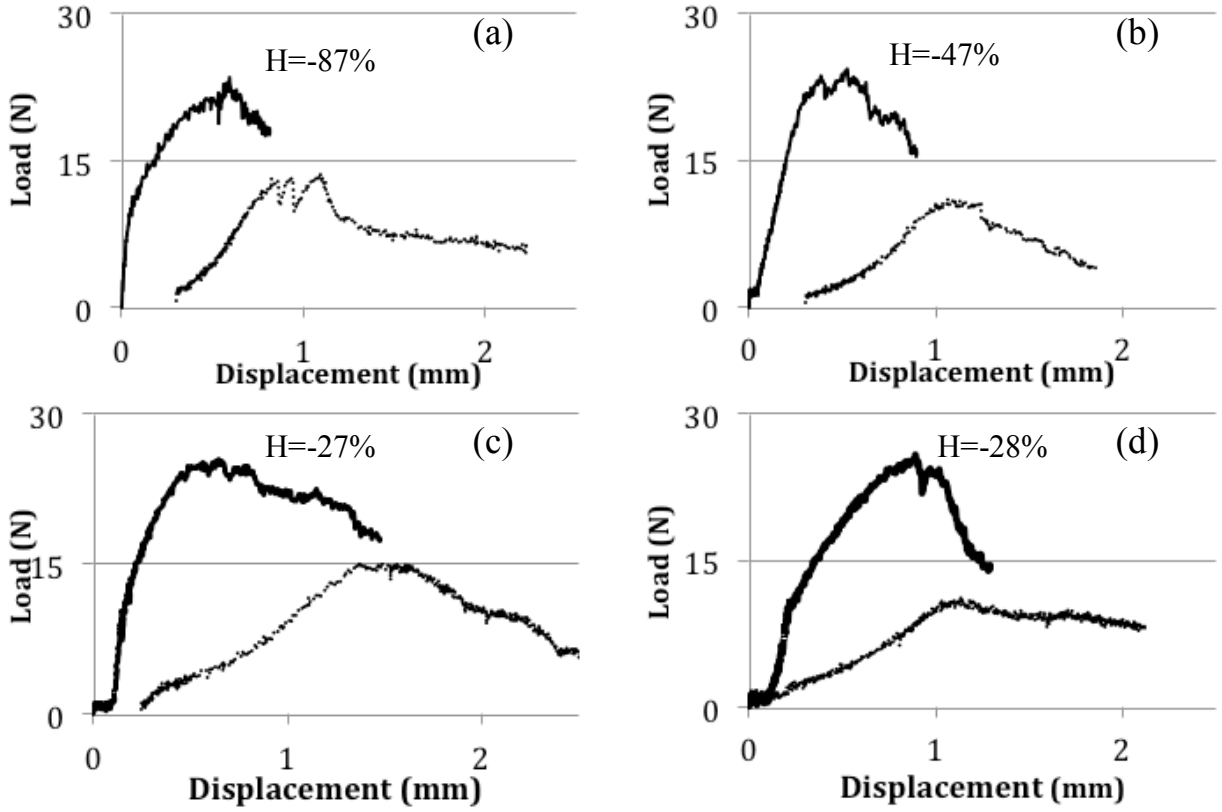

Figure 6-10- 3PB load displacement curves of C_3S-PVA samples, original and after soaking 7 days in water.

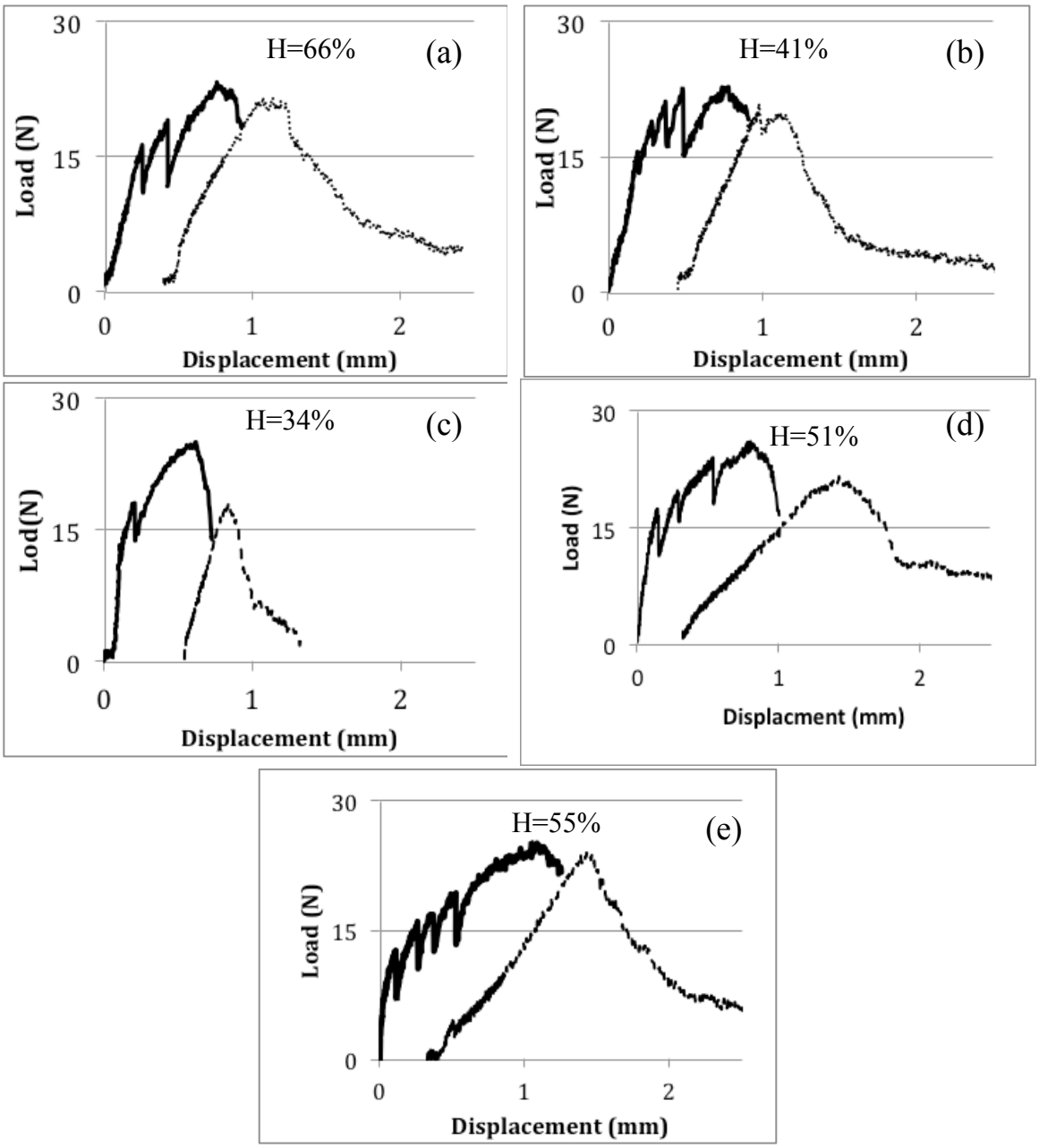

Figure 6-11- 3PB load displacement curves of C_3S-PVA samples, original and after 7 days soaking in SBF.

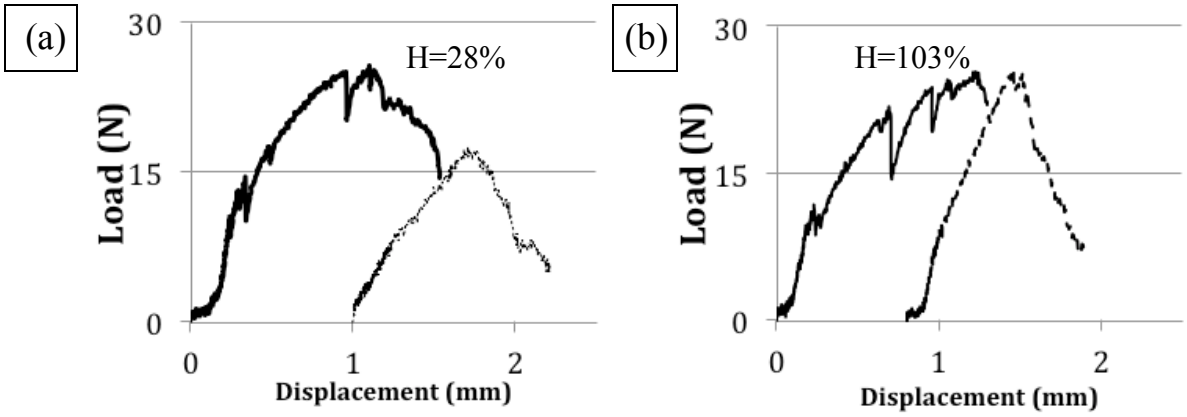

Figure 6-12- 3PB load displacement curves of C_3S-PVA samples, original and after 28 days soaking in SBF.

6.4. Microstructure and EDX analysis of crack healing by Scanning Electron Microscope (SEM)

In previous Sections, crack elimination and partial load-bearing capacity restoration was observed in the pre-cracked structure of C_3S-PVA samples soaked in SBF for 7 days. In this Section, the changes over the course of time in C_3S-PVA samples soaked in SBF were studied and some of the microstructures presented as representative of typical samples. The progress of crack healing and the chemical composition changes was tracked by EDX analysis in samples soaked in SBF and water. Similar changes were observed in many other locations of the samples.

Figure 6-13 shows SEM[8] images of the main macro crack of two samples soaked in SBF for one hour. Figure 6-14 and show the same samples and cracks after 6 hours soaking in SBF. Figure 6-14b,c,d show how the crack faces are "stitched" together through the formation of the

[8] - In order to perform *in situ* inspection of the healing process at variable times of soaking in SBF, we had to avoid coating the samples with a conductive layer. Therefore, using variable pressure mode instead of high-vacuum mode was inevitable. As a result, attaining high-resolution images was difficult, due to the accumulation of electrons on the surface or "charging". Charging eventually causes the incoming electron beam to scatter and the associated image to distort.

bridge-like precipitations. Figure 6-14f shows the thin precipitated phases that we conclude might be the first stages of the bridge-like precipitate formation during the healing process.

Figure 6-15 shows the EDX mapping of the Figure 6-14c, for samples soaked in SBF for 6 hours. The new phase precipitated on the crack is rich in phosphorus. The following pictures show the EDX analysis of the mapped area, in which the average P/Si ratio is 0.89. Figure 6-15e,f,g show the results of the EDX analysis on X1, X2 and X3 locations, respectively. The X1 location, on the crack edge has P/Si ratio of 6.72; P/Si ration for X2 and X3 locations are 0.64 and 0.77, respectively. EDX analysis is a qualitative method due to the inaccuracy of light elements detection and concentration calculations (e.g. for oxygen and carbon). However, comparison of the intensities of two elements in the same setup and the same sample provides semi-quantitative comparative information. The conclusion is that more P is available on the edges of the cracks (e.g. locations such as X1) rather than on the surface of the sample.

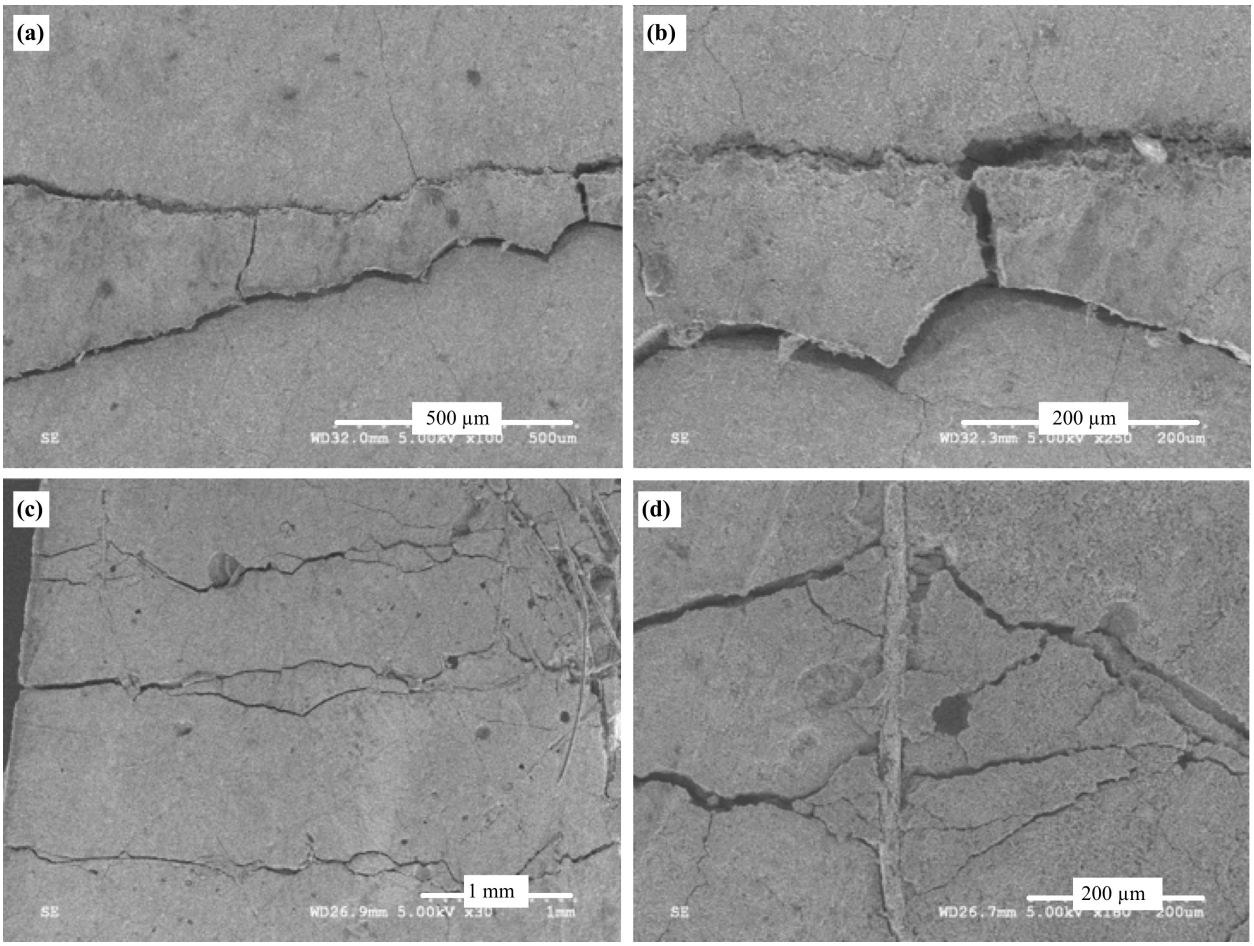

Figure 6-13 – SEM images of C_3S-PVA samples soaked one hour in SBF.

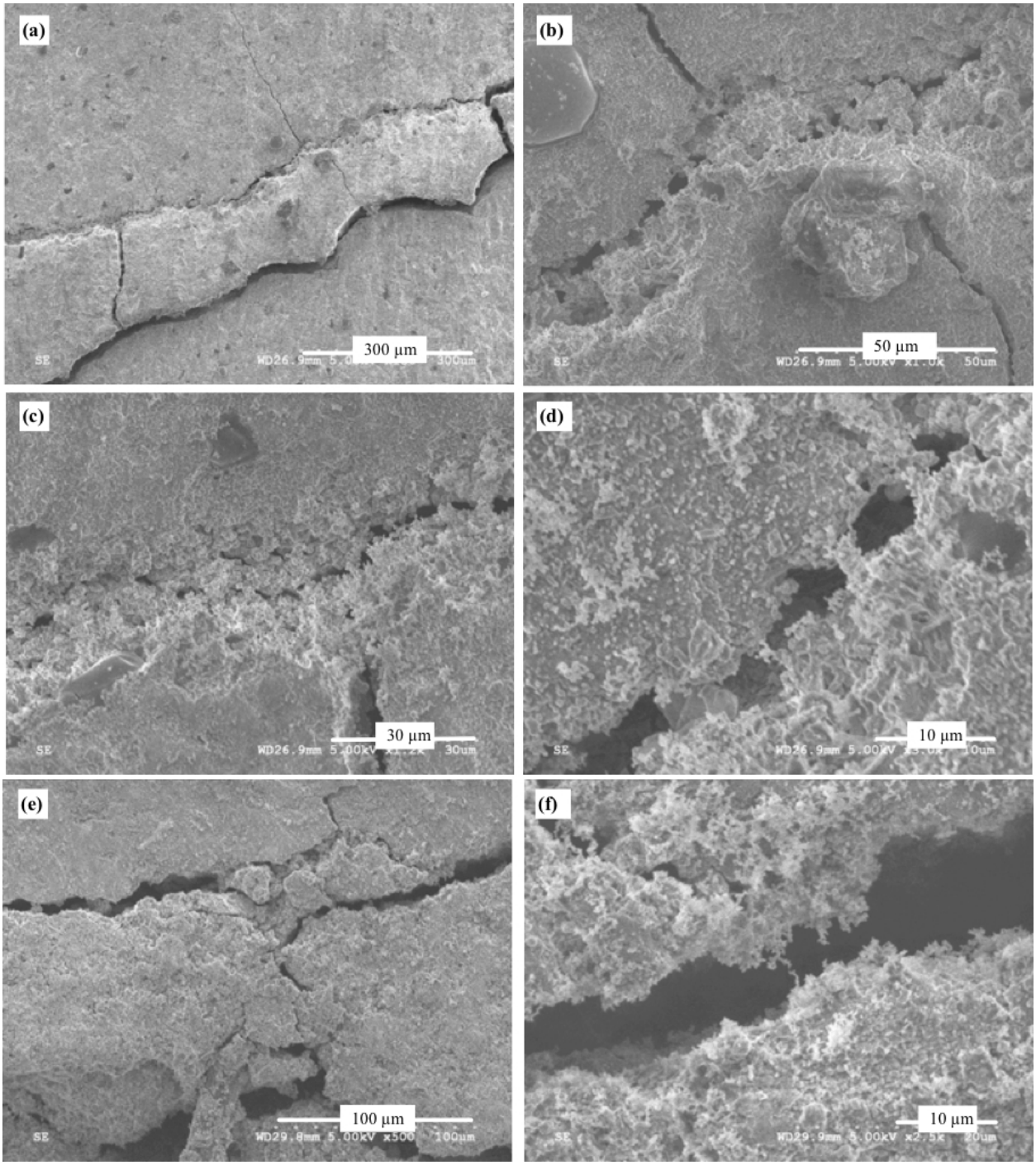

Figure 6-14- SEM images of C_3S-PVA sample soaked 6 hours in SBF.

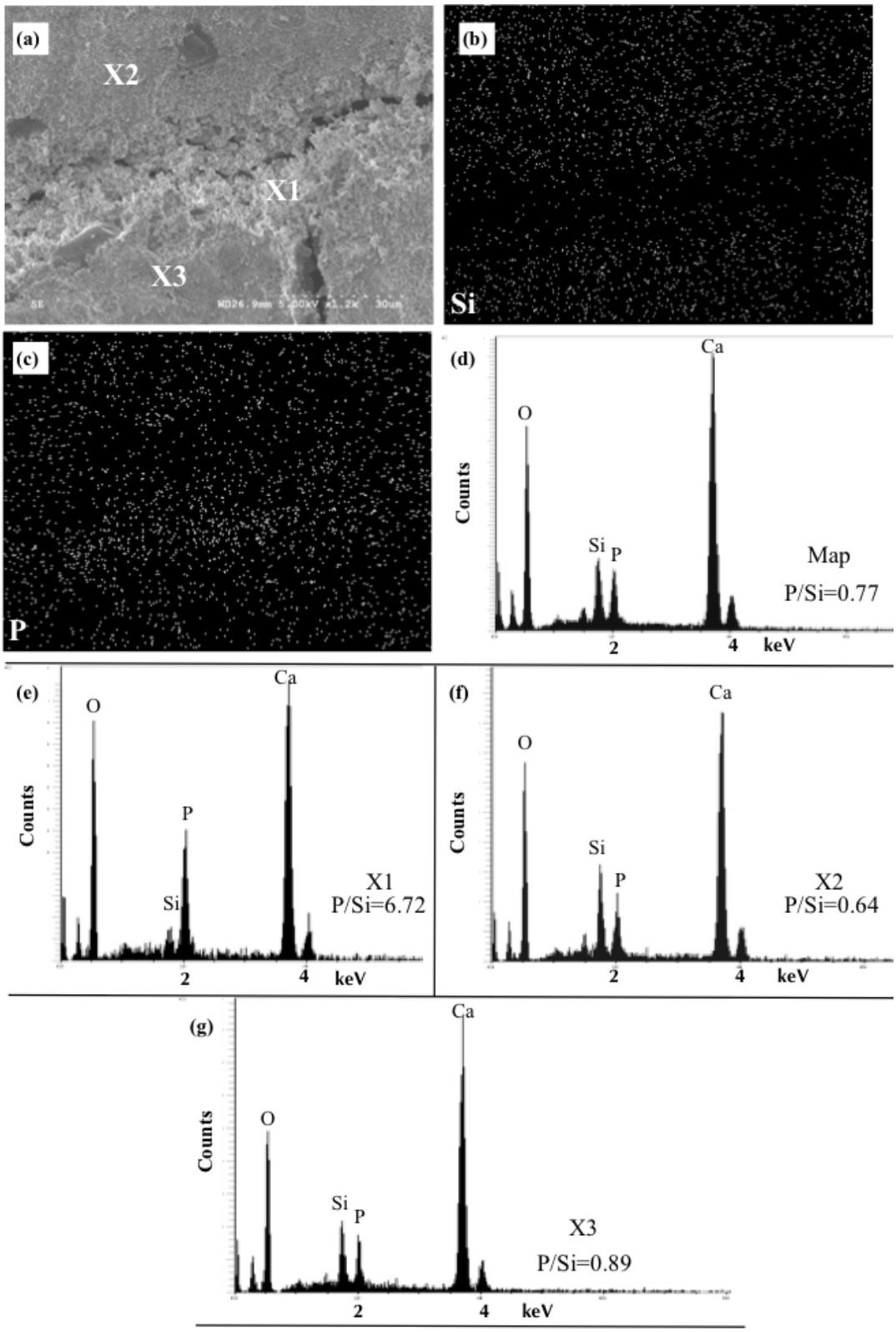

Figure 6-15- EDX analysis and map of the 6 hour soaked in SBF on the image of Figure 6-14c.

Figure 6-16 shows SEM images of the samples after soaking for 24 hours in SBF. It is expected that the crack surfaces will have nucleation sites available; therefore a new phase precipitating from SBF would nucleate and grow on each face of the crack. Consequently, the precipitates from the two faces will finally "collide" (or join) to form the bridge-like structures. These bridges "stich" or connect the two faces of the crack together. Figure 6-16c shows an evidence of formation of such bridges where two conical precipitates extending from each face of the crack are connecting to each other. This morphology can explain the dumbbell-shaped bridges connecting two faces of the crack. We observed these bridges in some parts of the sample soaked for 6 hours (Figure 6-14b, c, d), where the crack width was smaller (<5 μm). Figure 6-14f shows that in a larger crack (<20 μm) thin fibrous-like precipitations are formed. It is possible that these are initial nucleation sites of the precipitates, which subsequently grow perpendicular to the crack surface until meeting another growing counterpart on the opposing crack surface. Consequently, they attach to each other and form the dumbbell-shaped bridges. These bridges stitch the crack by connecting the two opposing face. Finally, the gaps among the bridges will be filled with new precipitates and the free space within the crack will be eliminated. More discussion and illustrations on this subject will be presented in the final Section of this chapter.

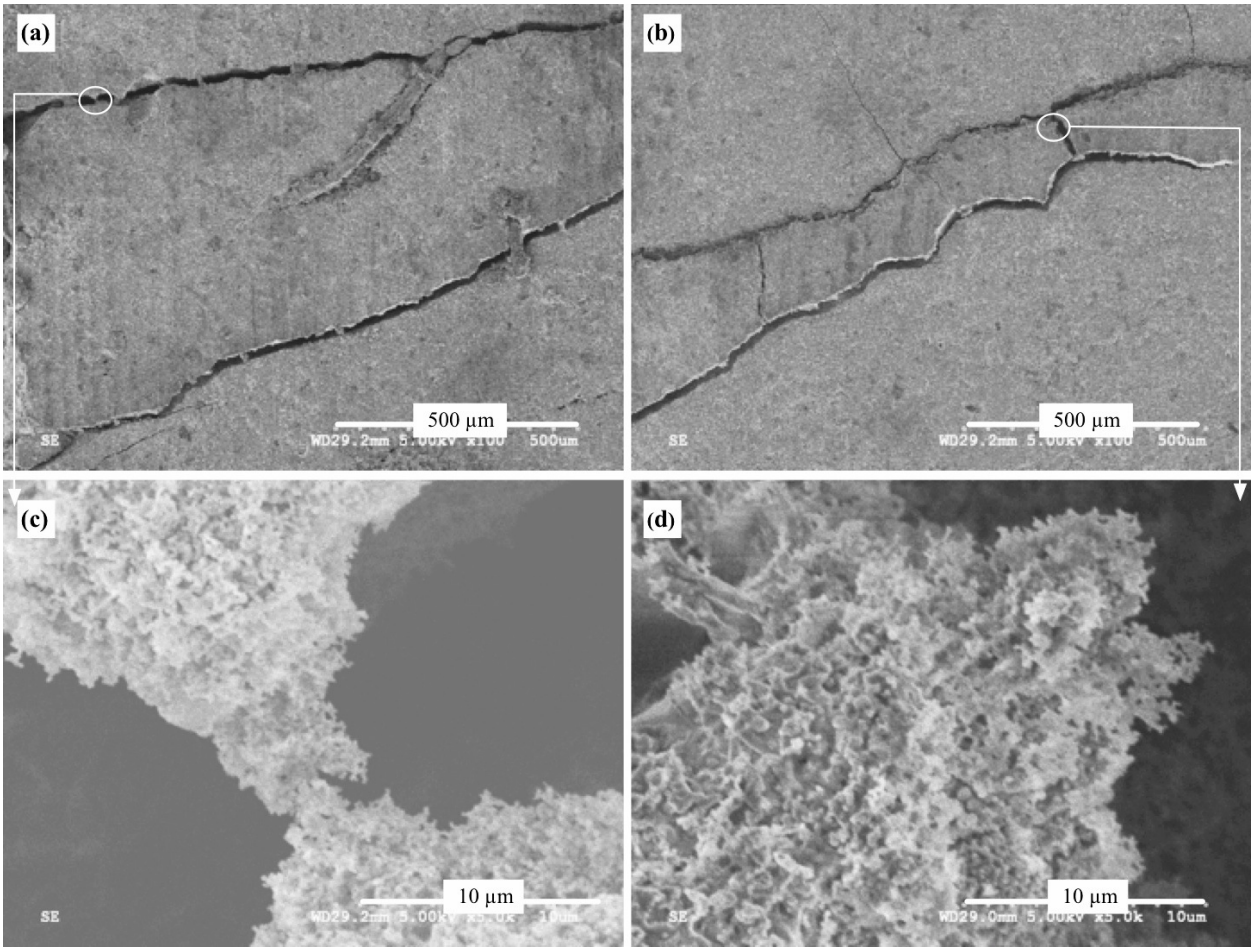

Figure 6-16– SEM images of the C_3S-PVA samples soaked 24 hours in SBF.

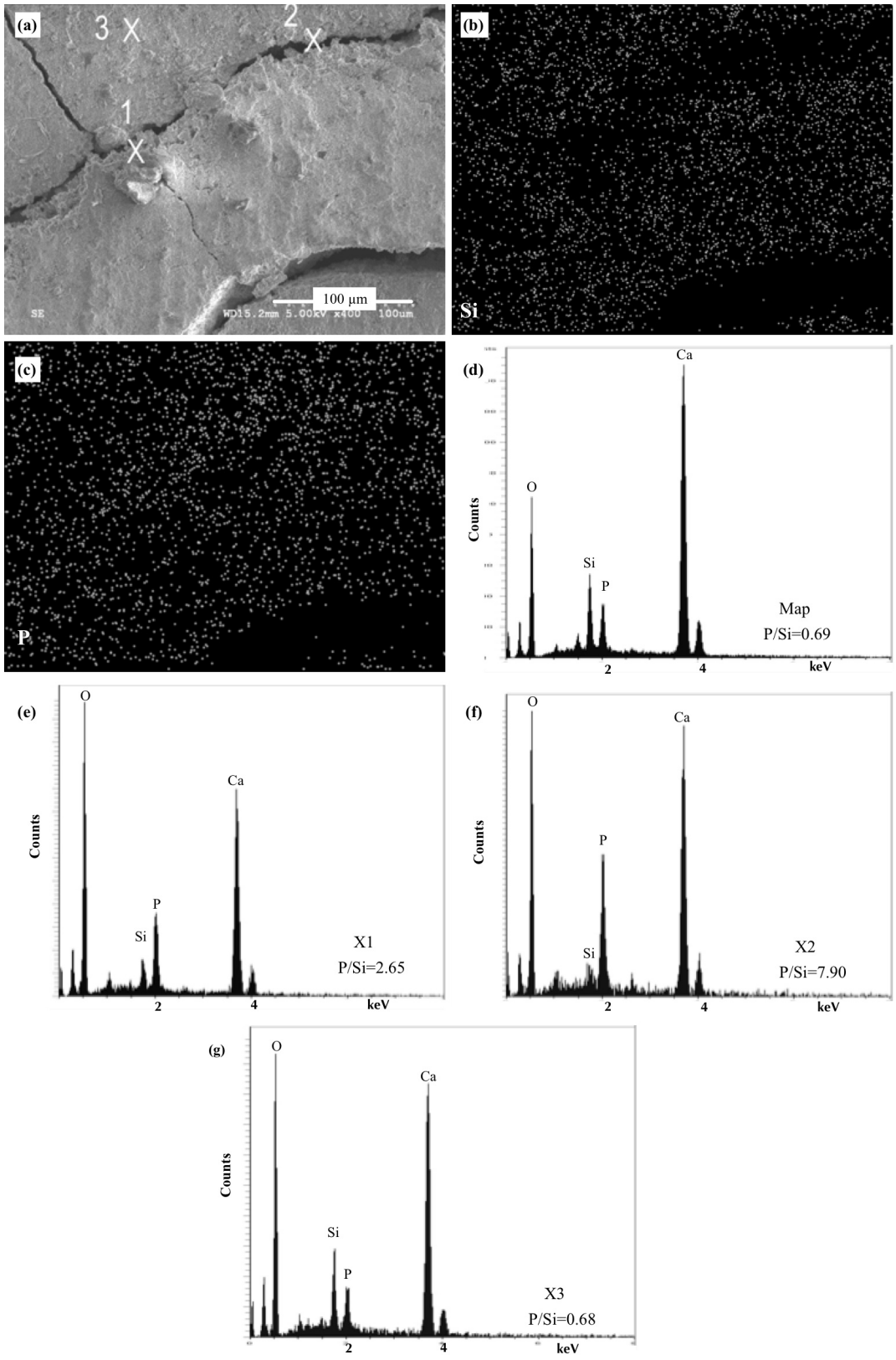

Figure 6-17- EDX and map of the distribution of the P and Si on 24hour soaked sample in SBF.

Figure 6-17a shows SEM image of C_3S-PVA sample soaked in SBF for 7 days and the EDX mapping of Si, and P are shown respectively in Figure 6-17b, c. Figure 6-17d shows EDX results of the mapping (average for the area). Figure 6-17g, h, i show the EDX results of the X1, X2, and X3 locations (shown in fig18a). P/Si ratio for X1 and X2 locations is larger than unit (2.65 and 7.90), where in X3 location P/Si ratio is 0.68. As confirmed both by mapping and point EDXs, higher concentration of phosphorus is observed in the vicinity of the crack. As the calcium concentration is homogeneous along the crack edge, the precipitated phase might be calcium phosphate.

Figure 6-18 shows the SEM images of the sample soaked in SBF for 7 days. The EDX mapping of the Figure 6-18d is shown in Figure 6-19 and EDX mapping of the Figure 6-18e is shown in Figure 6-20. Similar to EDX mapping in Figure 6-17 for 24 hours soaking, after 7 days of soaking, higher concentration of phosphorus and lower concentration of silicon is observed along the crack edge. However, the overall P/Si ratios of the EDX results on the surface of the samples are smaller in the 7 day soaked samples in SBF compared to 24 hour soaking in SBF. This might be caused by precipitation of the calcium carbonate layer, which mask the calcium silicate and calcium phosphate substrate layers in EDX analysis.

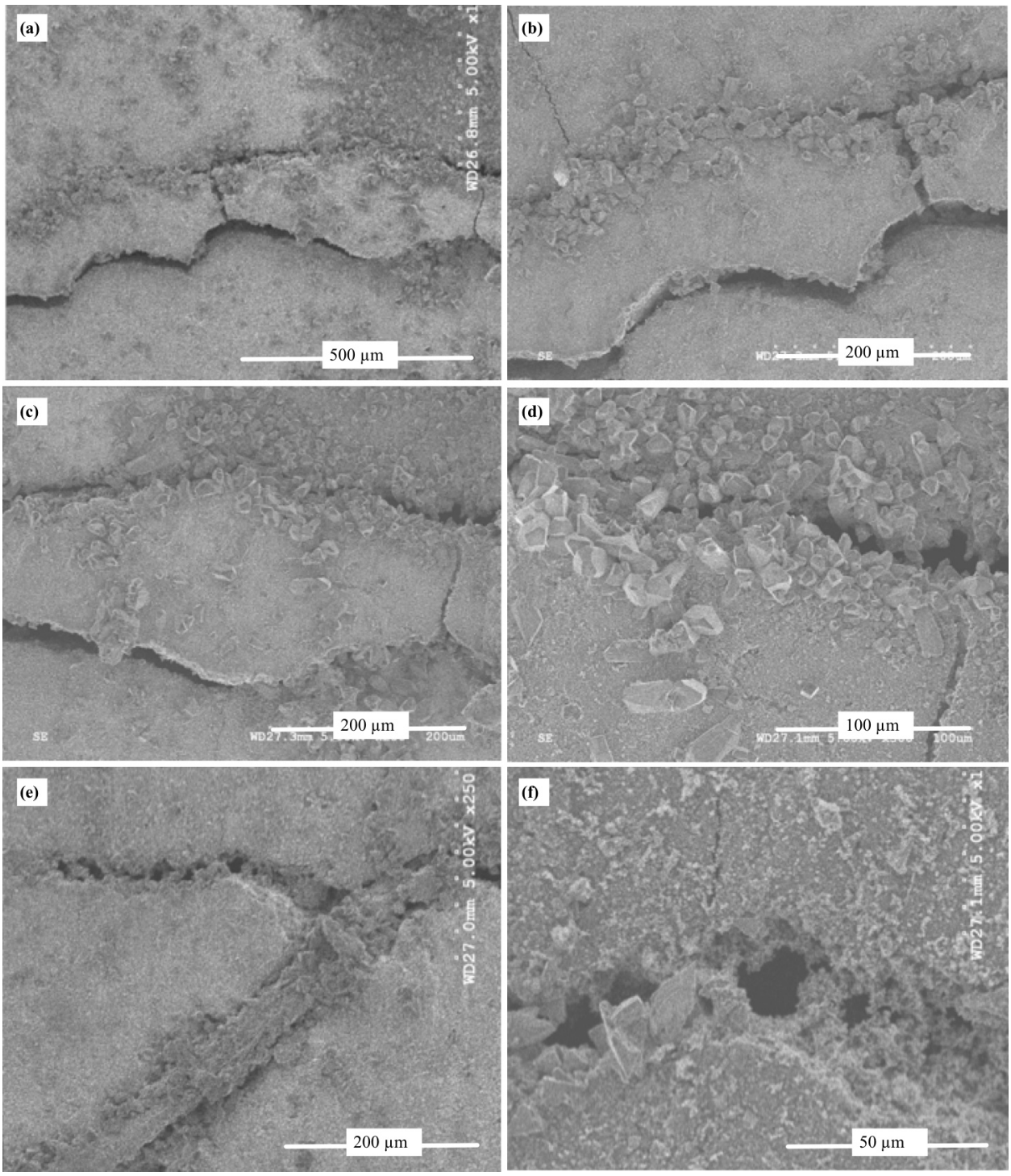

Figure 6-18- SEM images of C_3S-PVA soaked 7 days in SBF.

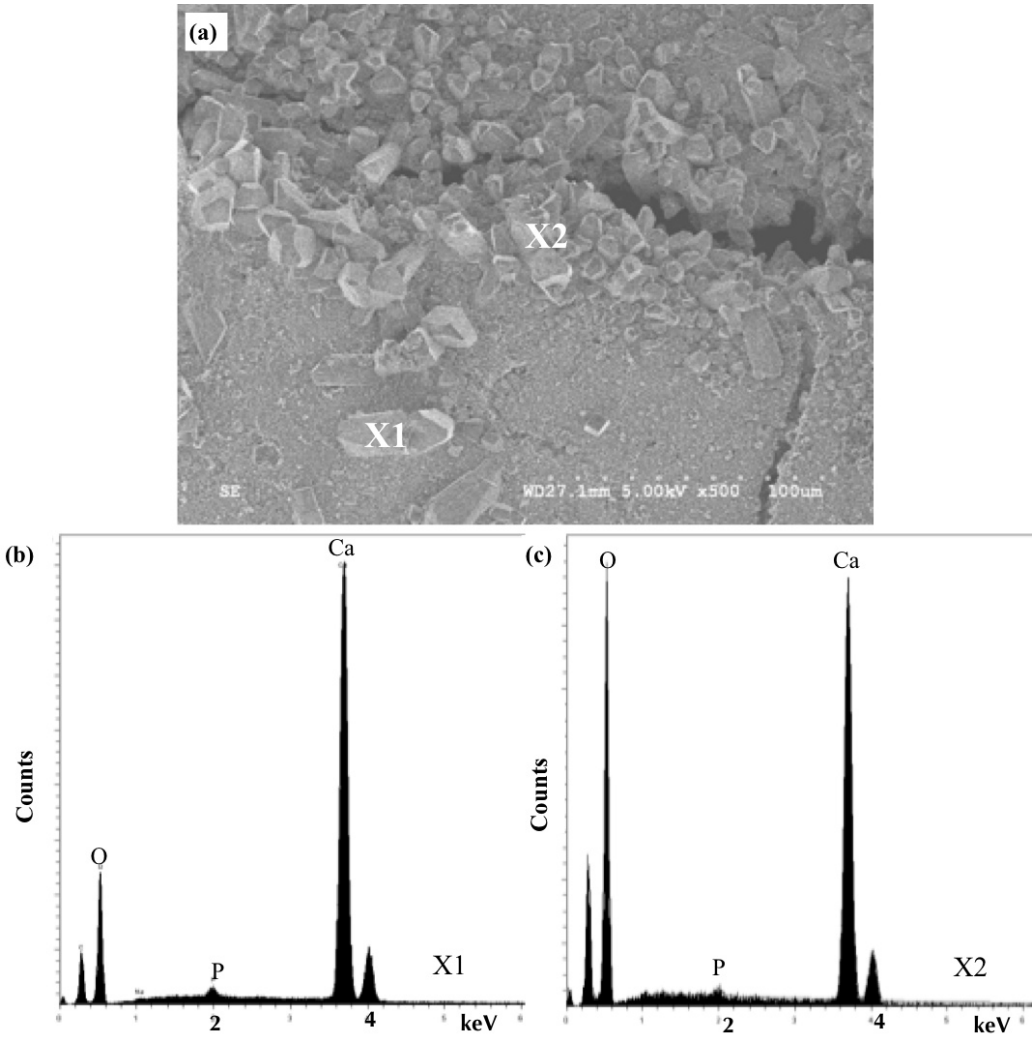

Figure 6-19- EDX on the 7day soaked sample in SBF.

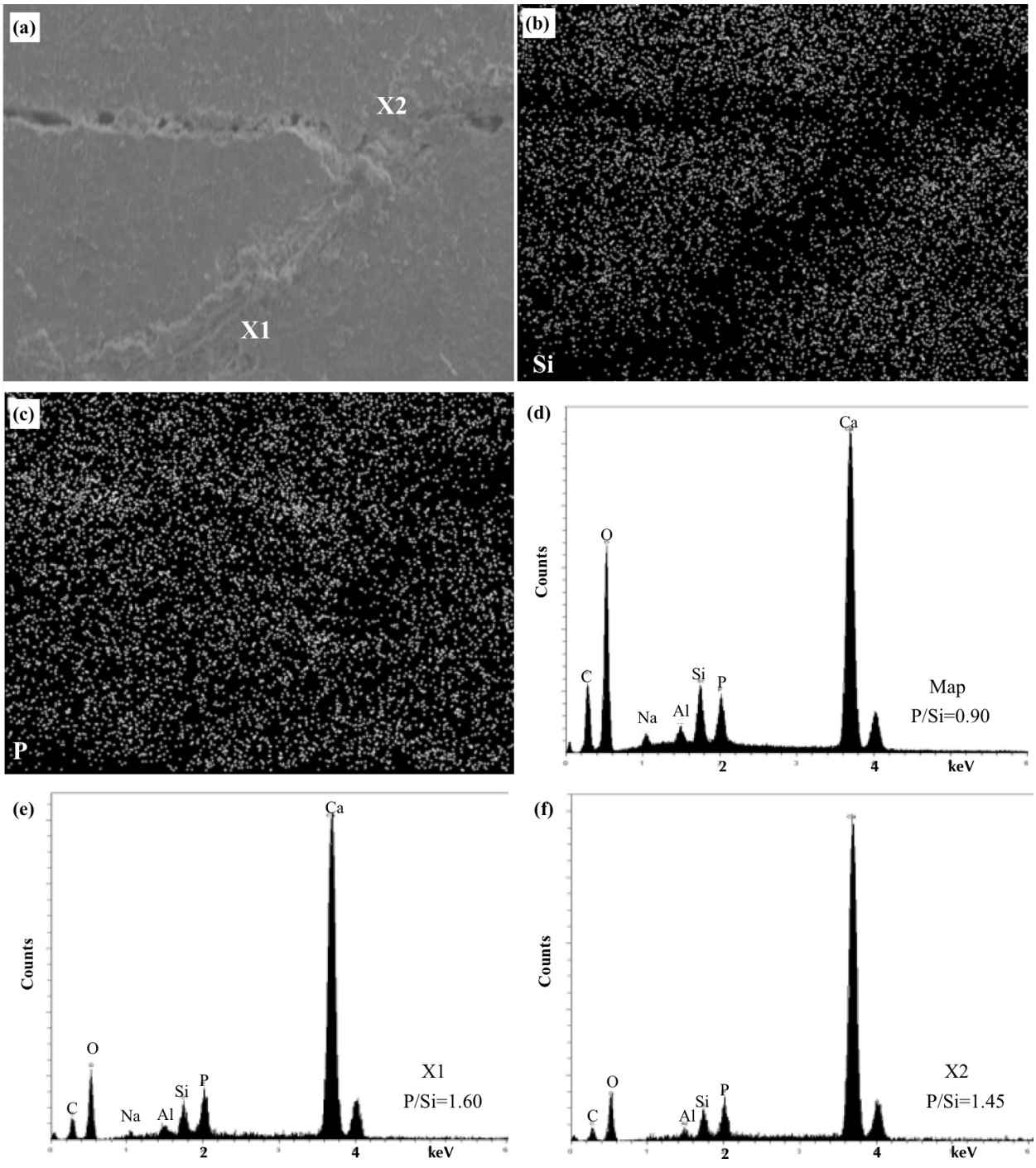

Figure 6-20- EDX of the C_3S-PVA soaked for 7 days in SBF (Si and P map shows Si deficiency in the vicinity of the crack, where there are higher amount of P available in the area).

In order to compare the before and after soaking microstructures of the samples healed in SBF, different phases present in the 10 day set sample, before soaking in SBF are shown in Figure 6-21 and Figure 6-22. Figure 6-21d shows the flower-like phases and their average area EDX (Figure 6-21c) shows that they consist of oxygen, carbon and calcium. This distinctive shape and composition is similar to aragonite (one of the polymorphs of calcium carbonate, with orthorhombic crystal structure) [176]. The hydration products of C_3S consist of two phases: one contains calcium, silicate and oxygen (C-S-H gel) and the other contains calcium and oxygen (calcium hydroxide or carbonate). The C-S-H gel phases have distinctive forms, including nano fibrous phases (Figure 6-22d) and nano flake-like phases (Figure 6-22f). Average EDX on the whole image of Figure 6-22d is shown in Figure 6-22c, where only carbon, oxygen, silicon and calcium are available.

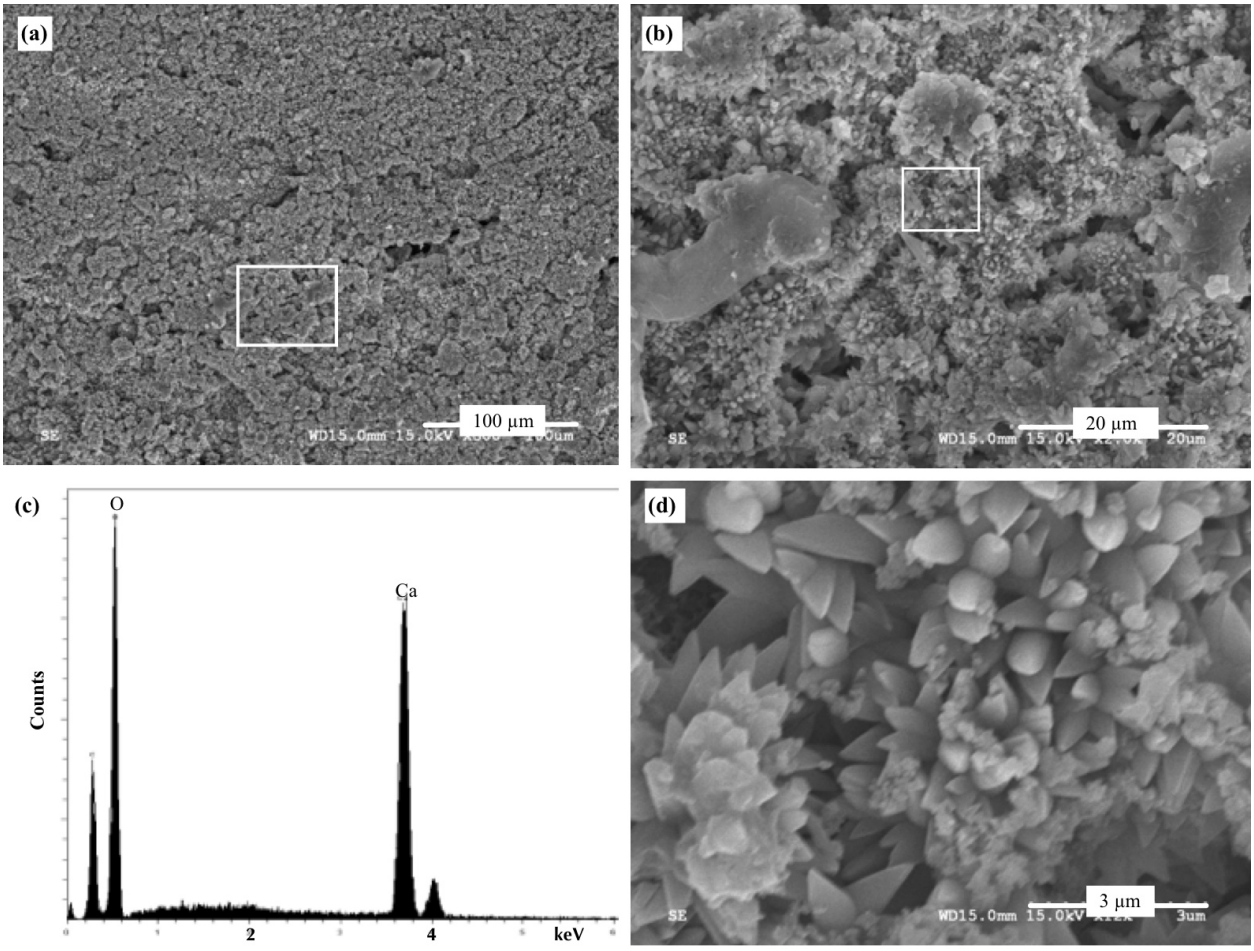

Figure 6-21- SEM of the surface of the 10 day set sample in water, before soaking in SBF.

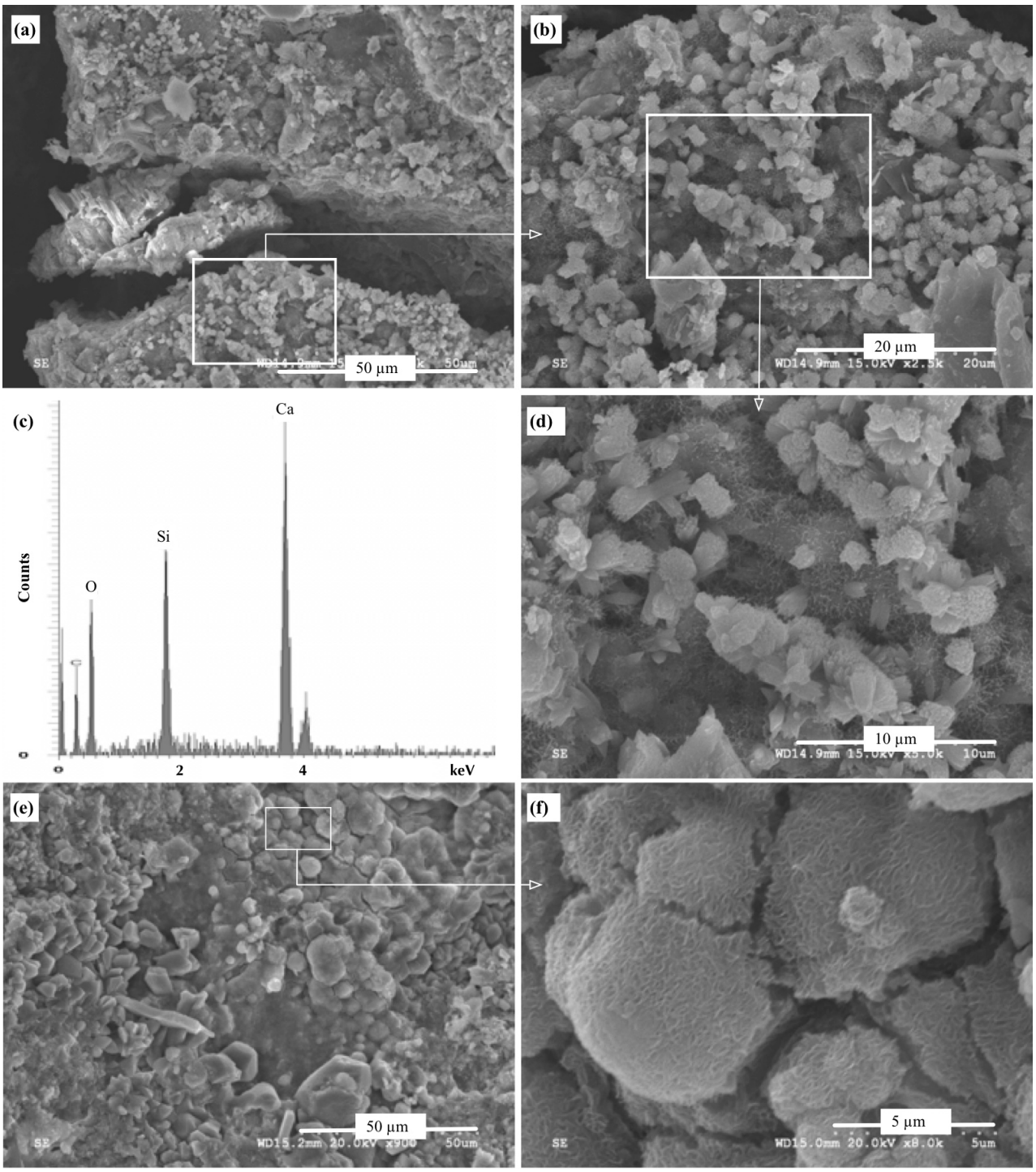

Figure 6-22- SEM of the cracked area of the 10 day set sample in water, before soaking in SBF.

In any form, C-S-H phase provides high surface area, which promotes heterogeneous nucleation of the secondary phases (responsible for healing of the fractured specimens). Figure 6-23 shows the microstructure of the sample after 7 days soaking in SBF. It has similar crystals to Figure 6-21d, but the flower-like structure has nano-sized precipitations on its surface instead of a smooth surface. The results of EDX analysis of the precipitates suggest the presence of phosphorus (2 wt%). One possibility is presence of a layer of calcium phosphate phase on the surface. Another possibility is that phosphorus is present in 5μm depth underneath the beam spot (penetration depth of the EDX). Third possibility is absorption or substitution of phosphorus on the surface of the flower-like phase.

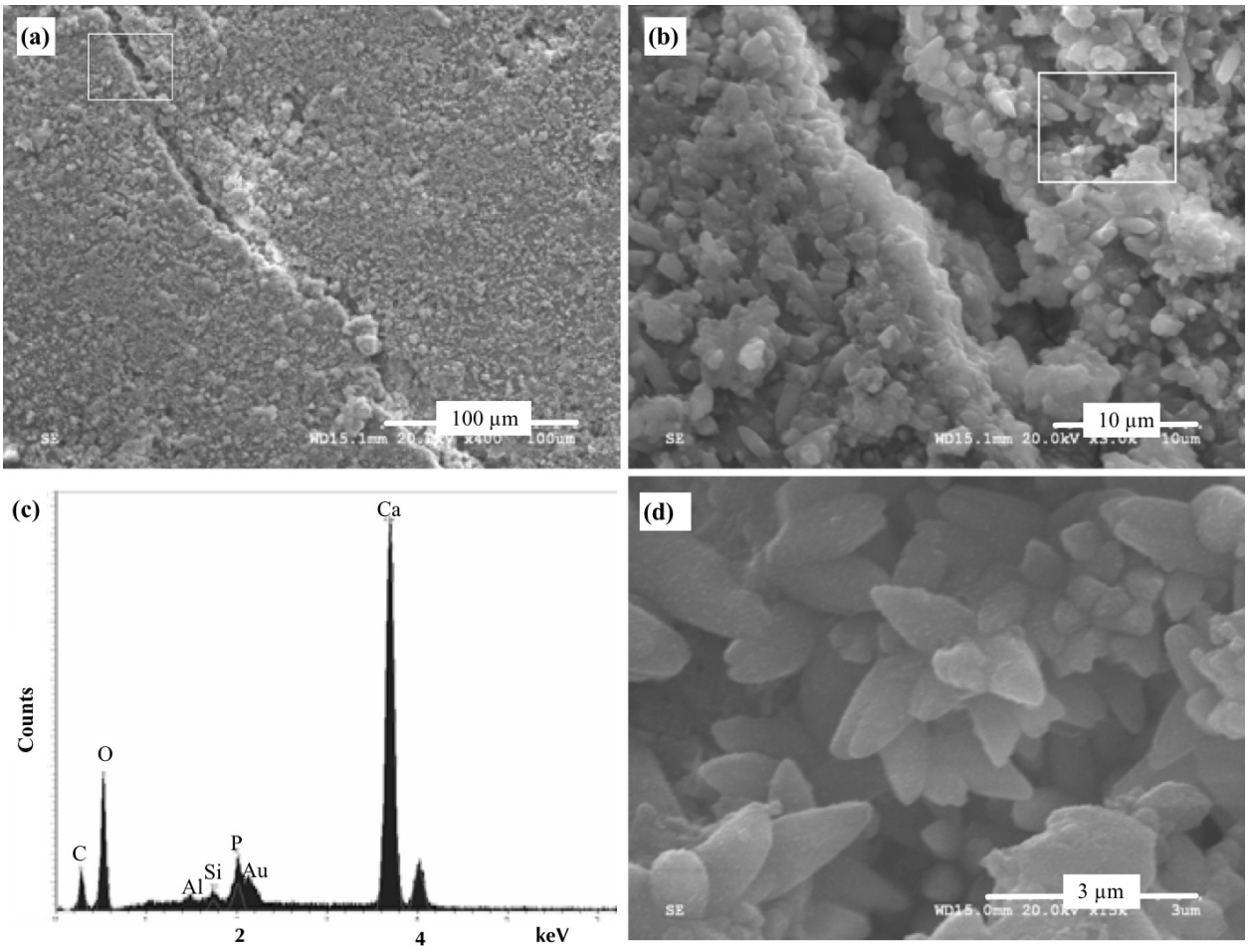

Figure 6-23 - Microstructure of the surface of C_3S-PVA sample soaked for 7 days in SBF.

According to the previous images for samples soaked in SBF for 7 days, information about the surface of the sample and the edge of the crack was gathered. Figure 6-24a,b show the cross section of the sample (away form the main macro cracks). In Figure 6-24c,d Si and P mapping of the image in Figure 6-24b is shown. Thickness of the CaP layer was determined by measuring the thickness of the area with high P concentration in Figure 6-24c. Therefore, on average CaP thickness is estimated to be ~5 μm, which is in accordance with Zhou et. al. work[81]. Presence of P in the inner part of the cross section is very low (0.40 wt% for the average mapping of the whole area), but the spot EDX result at the location close to the CaP layer (marked by X in Figure 6-24b and the EDX result is Figure 6-24f) detected much higher amount of P in comparison with the EDX mapping (3.0%).

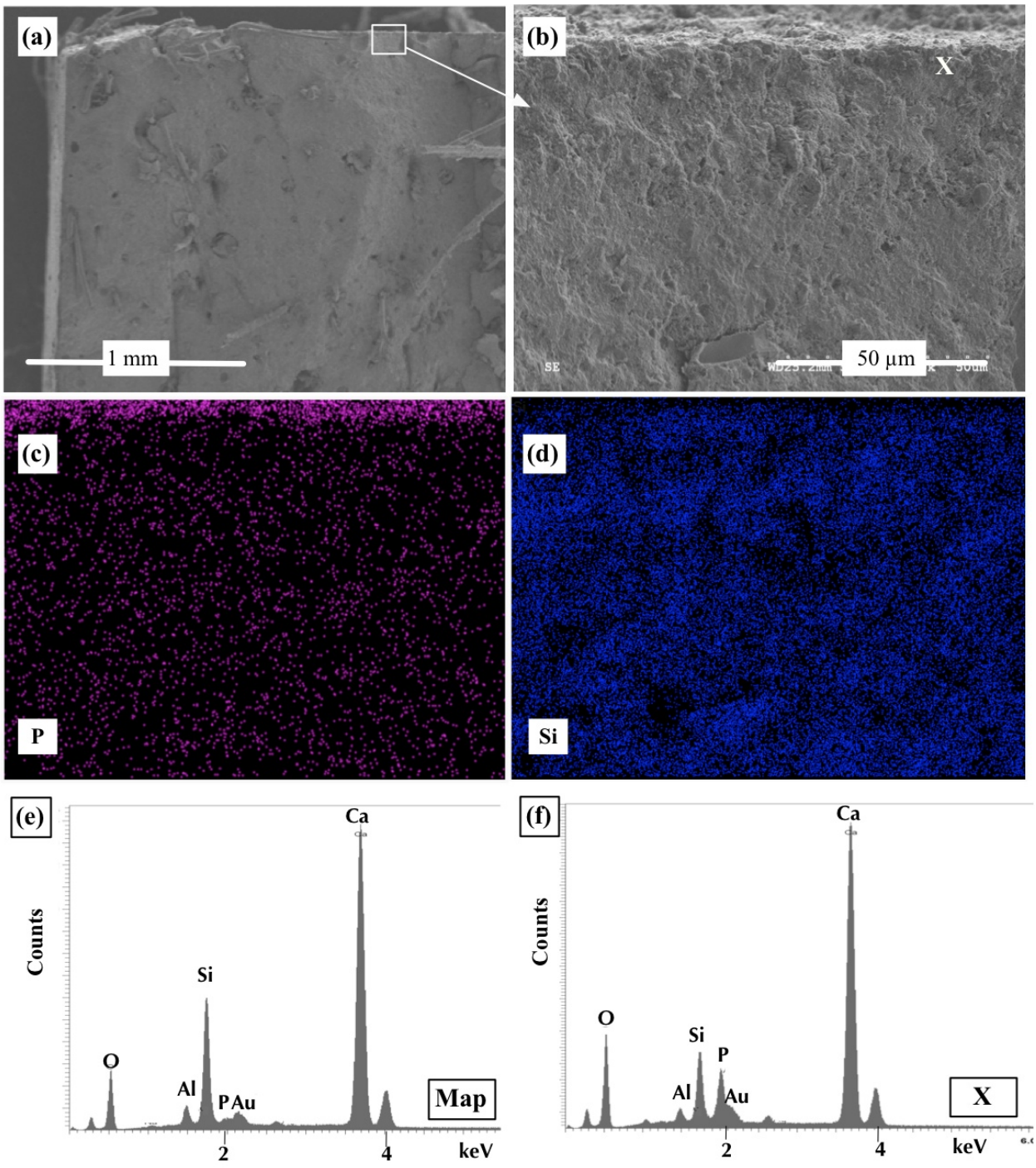

Figure 6-24- (a,b) Cross section of the C_3S-PVA sample soaked in SBF for 7 days, away from main macro crack; (c) EDX mapping of phosphorus; (d) EDX mapping of silicon; (e) the EDX of the mapping; (e) spot EDX of\n the location marked with X in image (b).

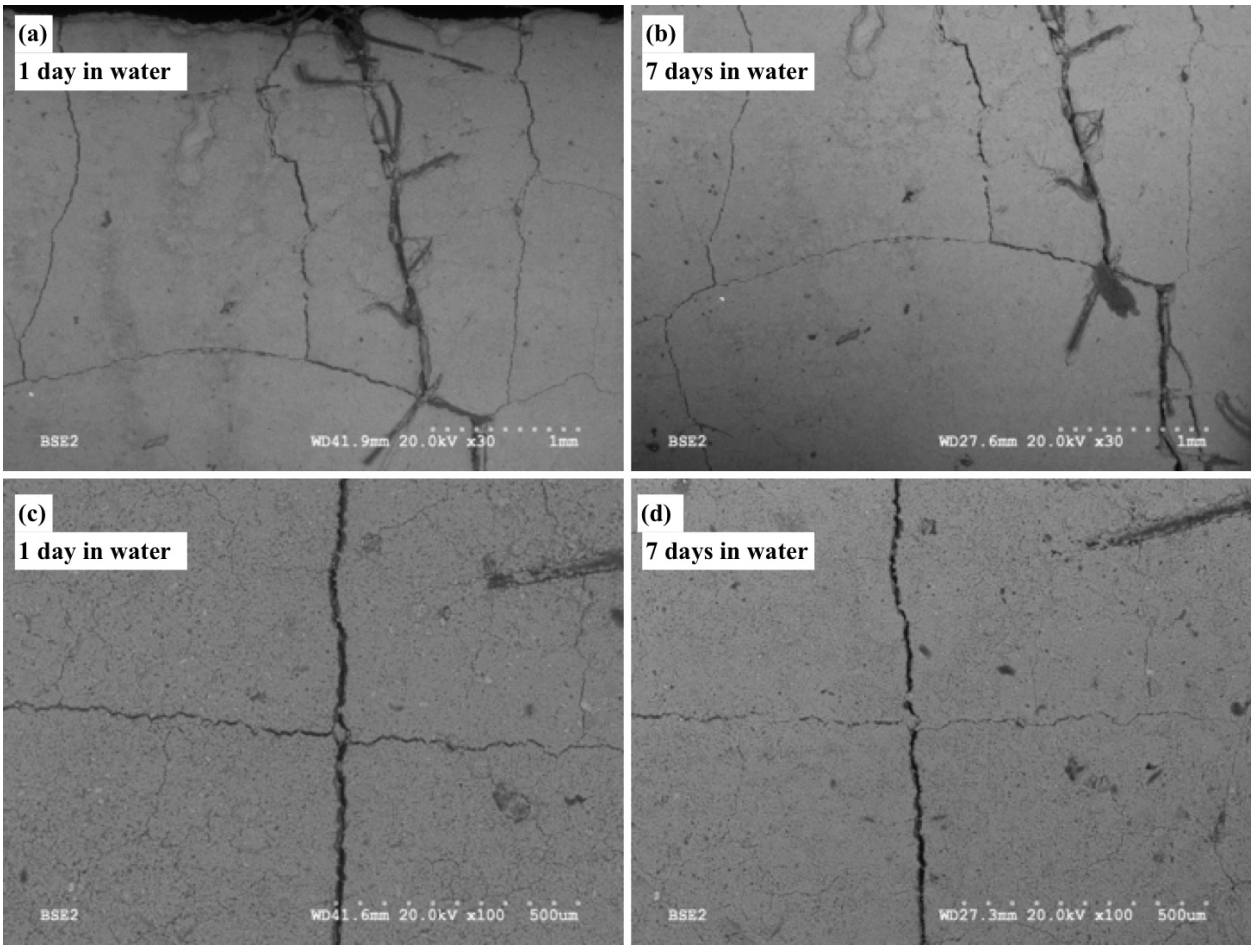

Figure 6-25- Low scale SEM images of the sample soaked in water for 1 day and 7 days.

To understand the effects of the SBF on the healing and precipitation on the C3S-PVA samples, micro and macro structure of the two sets of other samples are observed. First, 10 day set C_3S-PVA sample soaked for 7 days in water (total 17 days in water) were studied. Second, C3S-PVA samples set for 10 days in SBF and then soaked for 7 more days in SBF (total 17 days in SBF) were studied.

Figure 6-25 shows low-magnification SEM images of the samples soaked in water for one day and 7 days. The microstructure of the samples soaked for 7 days in water is shown in Figure 6-26a, b. The samples were previously set for 10 days in water, and after another 7 days of soaking in water, the total time of exposure to water was 17 days. Figure 6-26c,d show very similar results for the average area EDX of the Figure 6-26a,b, respectively. Although, Figure 6-26b shows some precipitates rich in calcium and oxygen, but calcium silicates have occupied main area of the sample surface, according to the EDX results.

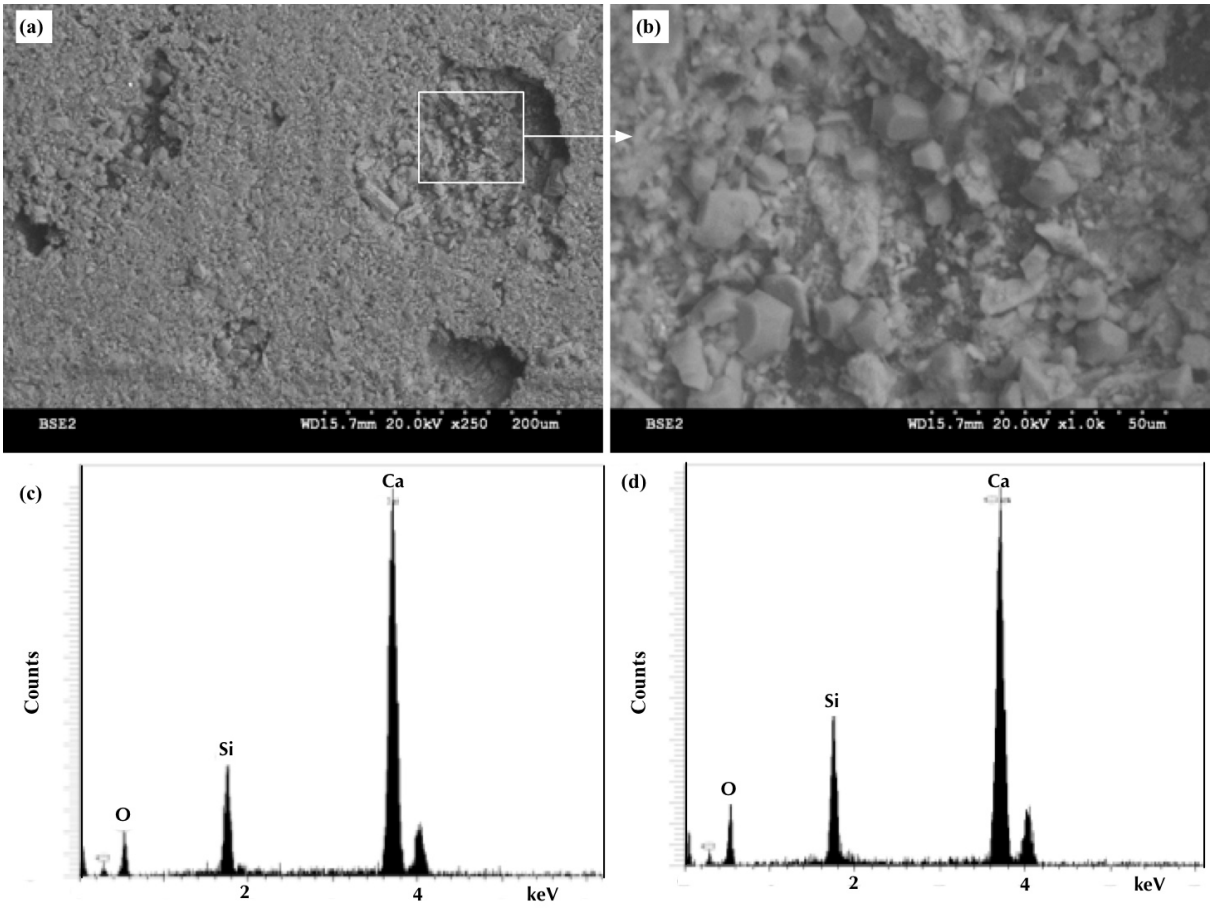

Figure 6-26- SEM and EDX analysis on the surface of the C_3S-PVA sample soaked 7 days in water (10 days set in water + 7 days soaked in water, total 17 days in water).

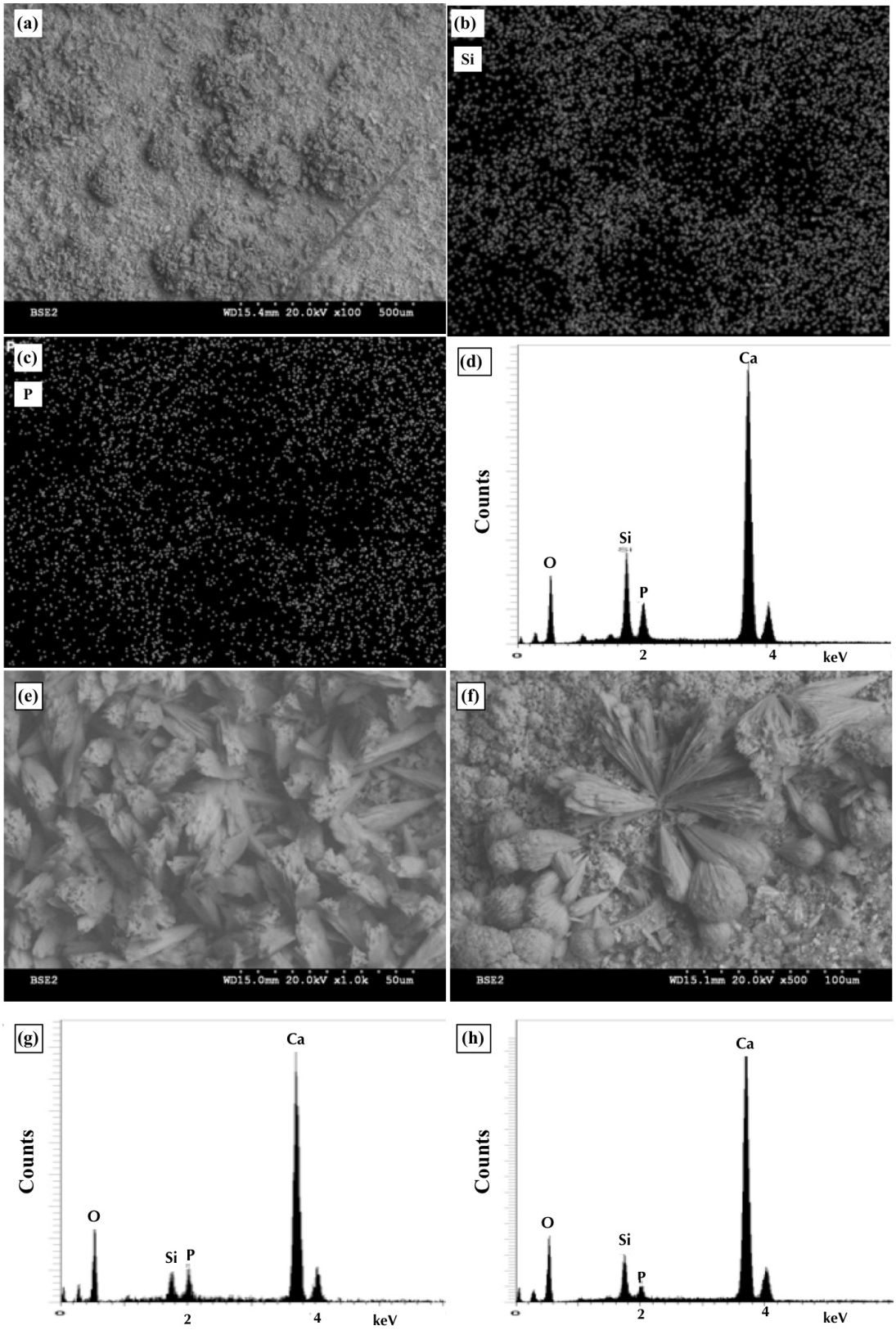

Figure 6-27- SEM and EDX Map of surface of the sample soaked for 17 days in SBF.

Figure 6-27 shows the macro and microstructure of the sample surface, soaked for the total of 17 days in SBF. The surface of the sample is covered by different phases, but all of them have similar composition, rich in calcium and oxygen. The shape of the crystals in Figure 6-27a,e,f is similar to aragonite. The semi-cubic crystals formed on the surface of the sample soaked for 7 days in water (Figure 6-26b) are more similar to the crystals that were observed in the set samples soaked for 7 days in SBF (Figure 6-18). Other phases observed on the surface of the sample soaked for 17 days in SBF, showing sheaf-like and flower-like clusters. In all cases, the shape of precipitates can be described as "radial arrays of polycrystalline aggregates", which Hutter and Bechhoefer define as spherulitic growth [177]. Gránásy et. al. divided the formation of spherulites into two categories: Category (1) Spherulite forms via central multidirectional growth (a growing sphere); Category (2) Spherulite originates from a folded-chain single crystal (a sheaf-like structure), then becomes a fully developed spherulite by unidirectional growth, and low angle branching [178]. Andreassen et. al. reported category 2 Aragonite spherulite growth in high supersaturation and 40 °C [179]. In this case, the growth can be recognized as category (2), i.e. sheaf-like structures in Figure 6-27f. Imai et. al. showed similar SEM images of aragonite on the silicate substrate at pH=9 [176]. Also, they showed that on a needle-like seed the same unidirectional growth occurs for aragonite (category 2). According to the EDX results, Na is available in the growth area of these phases. Stepkowska et. al. reported that the higher Na-content can slightly lowers the activation energy of transformation of calcite into aragonite, but its energy is higher [180]. Therefore, Na may act as a stabilizer for aragonite in room temperature (the transformation temperature is 450 °C). Carbonation of calcium silicate phases leads to volume increase and internal stresses [181], possibly responsible for deterioration of load carrying capacity. Aragonite has higher density than calcite (is 2.93 and 2.71 g/cm^{-3},

respectively) [180]. Therefore, volume increase for calcite precipitation is higher than aragonite (per unit mass), thus calcite may cause more internal stresses and load capacity deterioration than aragonite (e.g. in samples soaked in water versus samples soaked in SBF). In order to further discuss this subject, we need more information on the phase analysis and composition, which will be presented in the next chapter.

6.5. Chemical composition and phase analysis

In Section 6.4, we observed microstructural changes in the cracks for different healing treatments (water and SBF). Elemental chemical composition of the phases was determined by EDX analysis and mapping. To better understand this healing process, we further analysed the phases by XRD (Section 6.5.1), studied changes in the pH of the samples (Section 6.5.2), and determined the available functional groups by FTIR (Section 6.5.3).

6.5.1. Phase Analysis by X-Ray Diffraction (XRD) method

Figure 6-28 shows Co-Kα XRD spectra illustrating the stages of C_3S setting in water from 3 hours to 7 days. At 3 hours, the only detectable crystalline phase is C_3S. According to the literature setting reaction starts only seconds after the addition of water to C_3S powder, but the only well crystallized component of hydration products is $Ca(OH)_2$ [76]. At 3 hours hydration the amount of $Ca(OH)_2$ was still too small to be detected by XRD. In 24 hours hydrated samples, the intensity of C_3S peaks clearly decreases, and the intensity of $Ca(OH)_2$ or Portlandite phase increases. In 10 days set samples, still some un-hydrated C_3S and sharp peaks of $Ca(OH)_2$ are observed. In XRD patterns, the broader the peaks, the smaller the particles are (or more amorphous[9]) [182]. Therefore, $Ca(OH)_2$ with sharper peaks might indicate presence of larger

[9] - There are many other factors effecting broadening of XRD peaks [182]; as we are comparing two samples in the same setting in the same instrument, we assumed that the only difference governing broadening of XRD peaks is the size of the crystals.

crystal sizes. This is in agreement with SEM images of large hexagonal platelets of $Ca(OH)_2$ (10-50 μm).

Figure 6-29 shows the XRD patterns of the precipitated phases on the surface of the 10 day set sample soaked for different times in SBF. It also shows the XRD pattern of the fresh C_3S-paste soaked in SBF for 7 days. The latter can be considered as a simulation of the inside part of the crack, wherein SBF has an access to un-reacted C_3S particles. In order to obtain phase analysis of the precipitated layer, we have isolated the precipitated particles from the surface of the set sample to avoid masking it by the substrate pattern. According to the patterns available in Figure 6-29, precipitates on the surface of the 10 day set sample consists of some un-hydrated C_3S and Portlandite. After 1 day soaking in SBF, the main phase detected by XRD is calcite (and small amount of Portlandite). As the peak intensities of calcites are low and only one of the peaks is dominated, it might indicate the possible directional growth of calcite. After 7 days of soaking in SBF, still the only available phase is calcite, but it has higher intensities and other peaks related to other crystallographic planes are visible. On the other hand, according to EDX

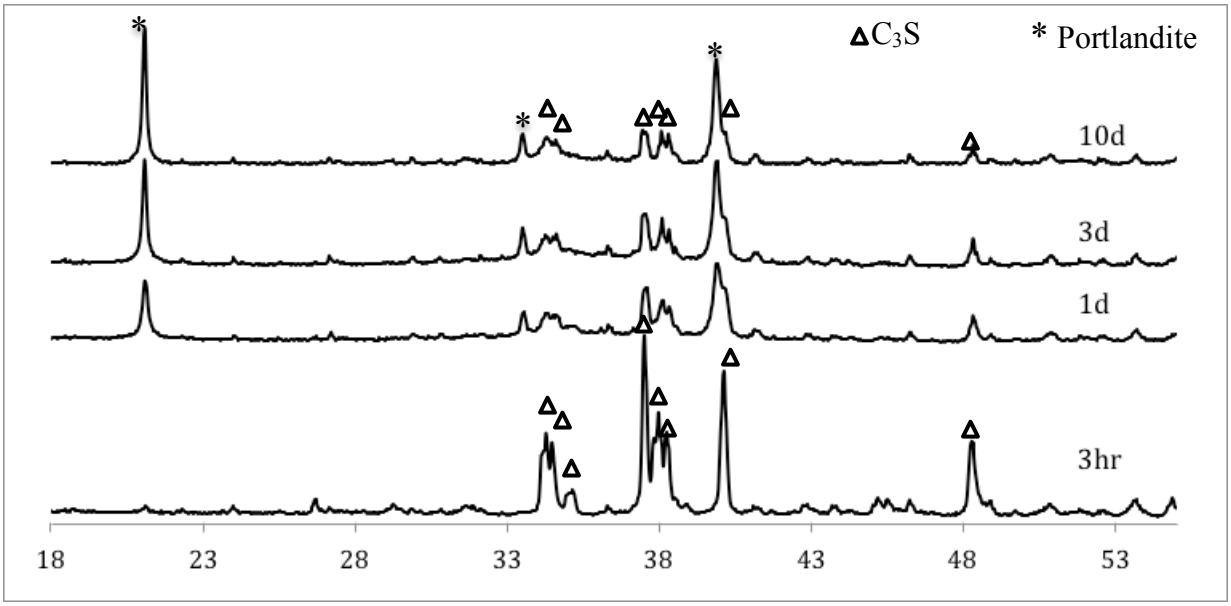

Figure 6-28 - XRD patterns of the C_3S setting in water at 37 °C.

data in Section 6.4, some phase(s) containing phosphorous should be available. It is possible that i) phosphorous is available in the form of nano-scale calcium phosphate phase or amorphous phase, therefore is not visible by XRD; ii) phosphorous is doped into the C-S-H gel structure; iii) phosphorous containing phase is on the substrate and is not detached from the substrate by scratching. Further studies, such as using TEM for measuring the crystallographic d spacing and distortion of the crystal structure could obtain more precise information and confirm these possibilities.

According to Figure 6-29, precipitates on the surface of the fresh C_3S paste after 7 days of soaking in SBF contains un-reacted C_3S, Portlandite and calcite. Precipitates on the surface of the 10 day set C_3S sample after 7 days soaking in SBF is mainly consist of calcite. In the 10 day

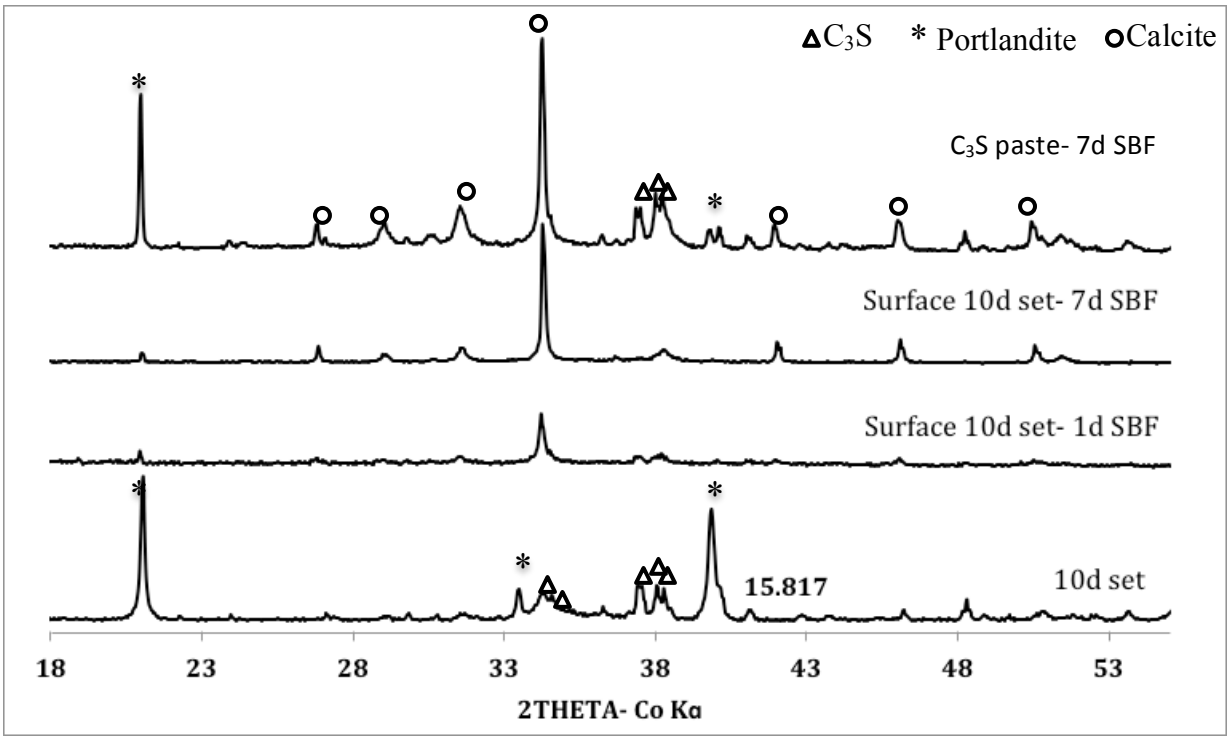

Figure 6-29- XRD patterns of the 10-day set sample and C_3S-paste sample soaked in SBF.

set samples, there is no access to fresh C_3S, as the hydration products have covered the C_3S particles. Presence of un-reacted C_3S on the surface of the samples affects the behaviour of the samples when soaked in aqueous solutions, e.g. SBF. In the next Section pH changes during soaking (healing) the materials in SBF are presented and more discussion follows on this subject.

6.5.2. Variations of pH during the healing process in water and SBF

To better understand the reactions that control elimination of the cracks, we measured the pH values of the 10 day set samples, soaked in water or SBF up to 7 days at 37 °C. To simulate the confined environment inside of the cracks, fresh paste samples were used. We assumed that the cracks would expose the un-reacted C_3S particles to small amount of ingress water or SBF through the cracks. The minimum possible amount of water or SBF in our experimental setup (6 ml) was used, to emphasize the limited amount of solution available inside the cracks and measuring the local changes in pH. Figure 6-30 shows variations in pH values of the 10 day set samples and paste samples, soaked in SBF and distilled water. Summary of the pH values are presented in the Table 6-1. The samples soaked for 1 hour in SBF show significantly lower pH values than their counterparts soaked in water: For example, for a set sample, pH=7.7 in SBF and 9.2 in water; For paste sample, pH=8.3 in SBF and 10.2 in water. However, with increasing the soaking time, difference in pH values of the paste samples soaked in SBF and water decreases and the pH value in SBF is even higher than in water (e.g. pH=11.9 for sample soaked 7 days in SBF and pH=11.4 in water). The paste samples have higher pH values than the set samples. The assumption is the set samples can represent the surface of the sample, while the paste samples simulate the environment inside of the cracks exposed to the healing environment. The pH of the inside part of the crack is higher than the surface of the sample. This difference is more

significant in case of SBF (for SBF, the difference is 11.9-9.2=2.7 pH units and for water is 11.4-10.8= 0.6).

Zhao et. al reported that the C_3S sintered ceramic bodies have pH value of 8.1 after 7 day soaking in SBF [15]. We observed higher pH values for 10 day set sample, soaked for 7 days in SBF (9.2); the reason for such difference might be low reactivity of the sintered samples compared to set cements. However, the results reported in [14] and ours suggest maintaining much lower pH value in SBF than the pH values associated with C_3S hydration in water (pH over 12 [183]), probably because of the buffered nature of SBF.

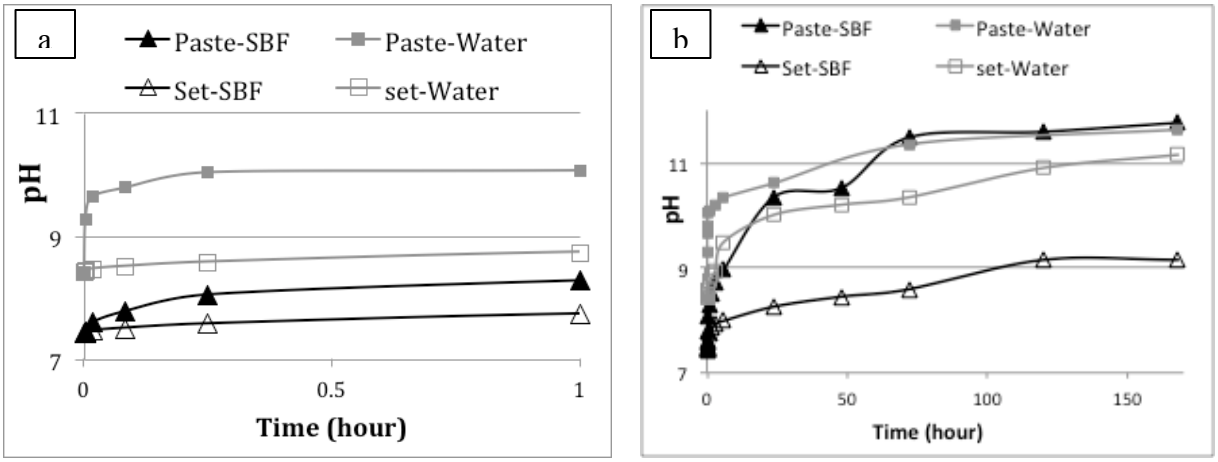

Figure 6-30- pH results for 10-day-set C_3S samples and paste samples soaked in SBF (a) first 60 min, (b) up to 7 days (168hr).

Table 6-1- pH values of C_3S set and paste in SBF and water

	1 hour	1 day	7 days
C_3S-Paste in SBF (6cc)	8.3±0.06	10.3±0.08	11.8±0.04
C_3S-Paste in water (6cc)	10.1±0.08	10.6±0.03	11.6±0.09
Set C_3S in SBF (50cc)	7.8±0.05	8.3±0.07	9.2±0.08
Set C_3S in water (50cc)	8.8±0.07	10±0.10	11.1±0.05

6.5.3. Functional group analysis by Fourier Transform Infrared (FTIR) spectroscopy

In order to further study the phases participating in the healing process, the functional groups of the precipitated phases were studied by FTIR. Figure 6-31 shows the FTIR spectra of the 10 day set C_3S sample (top) and precipitates on the sample after soaking for 6 hours, 24 hours and 7 days at 37 °C. The lower spectrum belongs to the precipitates of the C_3S fresh paste soaked for 7 days in SBF (i.e. simulating the inside part of the cracks).

To facilitate the interpretation of the spectra, all the possibly available functional groups and their associated wavenumbers are summarized in Table 6-2. Further discussion follows for each individual functional group (silicates, carbonates, phosphates, and hydroxyl).

Table 6-2- Summary of the FTIR peaks associated with the functional groups and availability of them in our spectra (Y-Yes available, M-Maybe available, exact conclusion cannot be made due to the overlapping of the peaks) [184-191].

	Silicate		Carbonate		Phosphate		OH
Wavenumber (cm^{-1})	452	925*	875-880	1420-1488	575	1038	3645
Set sample	Y	Y	-	Y	-	-	Y
6 hours in SBF	Y	Y	Y	Y	-	Y	-
24 hours in SBF	Y	Y	Y	Y	-	Y	-
7 days in SBF	Y	Y	Y	Y	-	Y	-
Paste - 7 days in SBF	Y	Y	Y	Y	Y	Y	-

*- With polymerization shift, the peaks located at 975-982 cm^{-1} can be recognized as 925 cm^{-1}

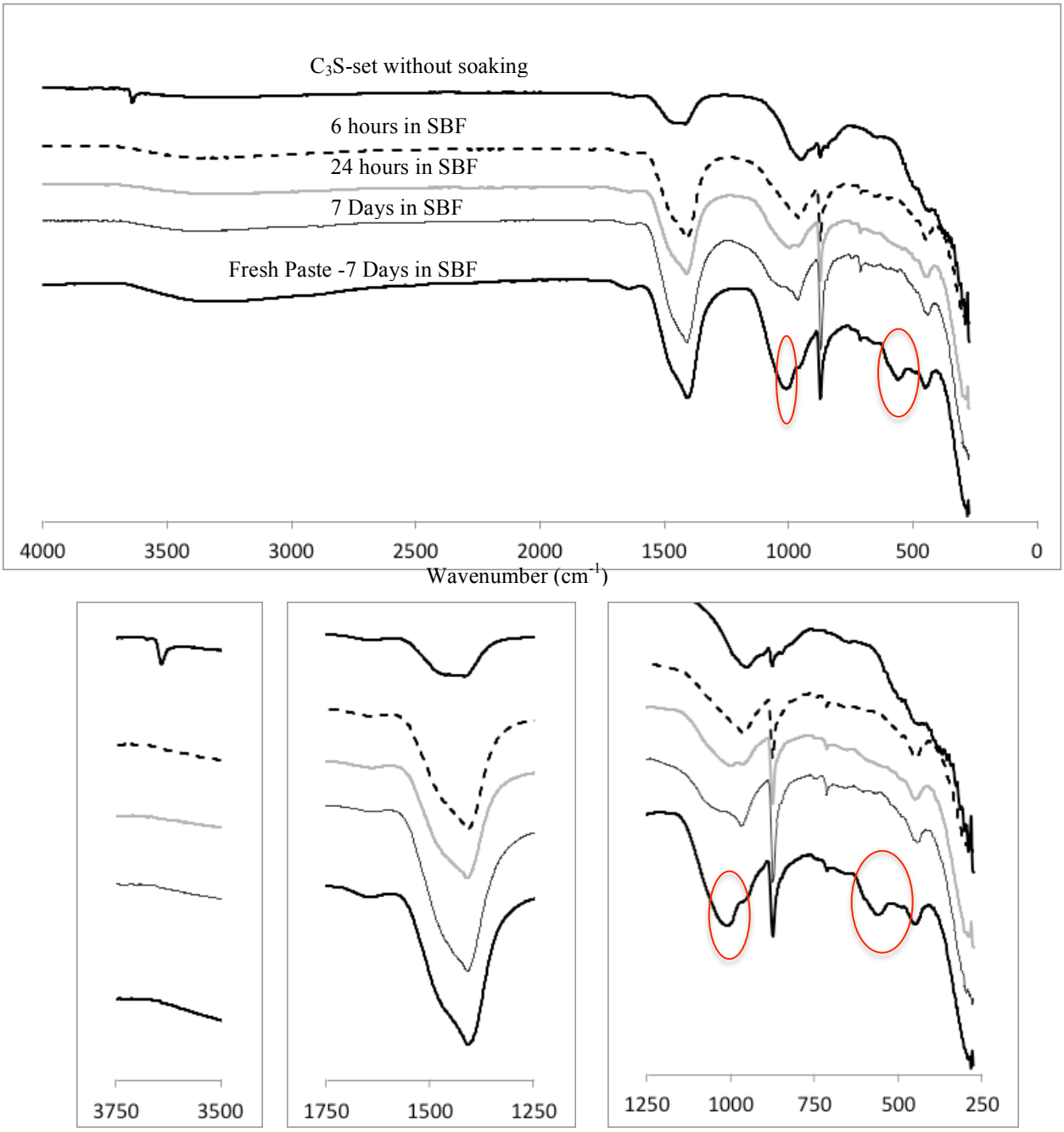

Figure 6-31 - FTIR spectra of the 10 day set sample, soaked for different times in SBF and fresh paste sample soaked in SBF for 7 days.

6.5.3.1. Silicate IR adsorption spectra

In all samples, there is a peak in the range of 459 - 462[10] cm^{-1}. The 452 cm^{-1} peak belongs to in-plane bending (v_2) of silicate [184]. The 460 cm^{-1} peak belongs to Si-O-Si and O-Si-O bending vibration in glass [191] and can be related to C-S-H structure with semi-amorphous nature. The peaks available in our samples are closer to the 460 cm^{-1}, therefore we conclude that they represent Si-O-Si and O-Si-O bending vibration in the C-S-H structure.

In our sample, there is a peak at 975 cm^{-1}. Asymmetric stretching (v_3) vibration of Si-O is located at 925 cm^{-1} [186]. However, the shifting of the Si-O stretching vibration (v_3) to a higher wavenumber is considered as "fingerprint evidence" for the degree of polymerization in regards to the formation of C-S-H phase [184]. Mollah et. al. showed that this shift can be as much as 60 cm^{-1} units [184]. Therefore, the peaks ranging from 975-985 cm^{-1} might belong to polymerized Si-O in the C-S-H structure. Also, availability of Si-O in-plane bending vibrations peak (v_2 at 452 cm^{-1}, which here is shifted to 460 cm^{-1}) can support this conclusion. However, there is another possibility, as 962 cm^{-1} peak is assigned to v_1 P-O stretching mode [186]. Although the EDX results did not show presence of P, but if small amount of P (e.g. <1%) forms solid solution with C-S-H, one may see FTIR peaks modification with no EDX peaks. Therefore, it is also possible that P is doped into C-S-H structure.

[10] - From top to bottom respectively the values for the peaks are 460, 459, 462, 459, 462; they represent presence of silicate v_2.

6.5.3.2. Carbonates IR adsorption spectra

712 cm^{-1} peak is known as the vibrational in-plane-bending (v_4) of carbonate [189]. Except the set sample, the rest of the samples have peaks close to 712 cm^{-1} (from top to bottom: 716,716, 715, 719 cm^{-1}). This suggests the carbonization occurred in all samples soaked in SBF. 875-880 cm^{-1} peaks represent carbonate functional group [184,185], which is not available in the set sample. All the other samples have a peak close to this range: 878, 882, 883, 883, 875 cm^{-1} (respectively from top, starting from 6 hours in SBF). Although some references are reported 863.3 cm^{-1} [187] and 870 cm^{-1} [190] as HPO_4^{2-} representatives, but as the other peaks for this functional group was not observed, these peaks most probably belong to carbonate.

The set sample (without SBF soaking) has a shoulder covering the range from1420 to1480 cm^{-1}. A broad shoulder indicates fusion of two or more peaks together. In the following curves of the samples soaked in SBF, the second peak gradually becomes distinctive and is located at around 1480 cm^{-1}. The carbonate bands are located at 1420–1480 cm^{-1} [184]. The wavenumbers in this range, that are associated to carbonate by different researchers include: 1414, 1418, 1419, 1420, 1421, 1422, 1460, 1465, 1480, 1487, 1488 cm^{-1} [185,187,188]. Also, 1472 cm^{-1} peak is reported to be CO_3^{2-} in PO_4^{3-} position in apatite [190]. Therefore, we may conclude that smaller amount of carbonate is available in the set sample, but soaking in SBF vividly increases the amount of available carbonate functional groups.

6.5.3.3. Phosphates IR adsorption spectra

The only pattern that has the 575 cm^{-1} peak is C_3S-paste soaked for 7 days in SBF. This peak is known as v_4 bending vibration of $PO4^{3-}$ [185,188]. The presence of phosphorus is confirmed by the EDX results (Section 6.4), presence of this functional group shows phosphorus is available in the form of a phosphate. As the measured pH for C_3S-paste-7dSBF was higher

than 11 (Section 6.5.2), the only thermodynamically stable calcium phosphate phase in this pH range is HAp. However, as the hydroxyl group is missing, the presence of HAp cannot be confirmed.

1038 cm^{-1} peak is assigned to v_3 P-O stretching mode [186]. For samples soaked in SBF, another peak gradually forms around 1020 cm^{-1} and merged with the 980 cm^{-1} peak. For the paste sample soaked for 7 days in SBF, the second peak is located at 1040 cm^{-1}. As mentioned before, peak at 1038 cm^{-1} is assigned to v_3 P-O stretching mode. Therefore we can conclude the sample soaked in SBF has phosphate groups (along with the other peak at 575 cm^{-1}). Also, it is possible that 962 cm^{-1} v_1 P-O stretching mode might be masked by the higher intensity peak at 975 cm^{-1} in the samples soaked in SBF.

6.5.3.4. Hydroxyl IR adsorption spectra

A small peak at 3649 cm^{-1} is observed in the set sample only. The band at 3645 cm-1 is due to the metal-bonded hydroxides and can be related to OH bond from $Ca(OH)_2$ in our samples [184]. Disappearance of this band after soaking in SBF can be related to the calcium hydroxide leaching from the sample to the aqueous environment, which causes the pH to increase.

6.5.3.5. Summary of FTIR spectra studies

All samples show the silicate functional groups associated with C-S-H structure. The set sample has low amount of carbonate, while the soaked samples have higher amount of carbonate (according to the growing intensity of associated peaks). C_3S-Paste sample has the highest intensity of phosphate functional group peaks among all the other samples. However, other samples soaked in SBF have some of the phosphate associated peaks in their patterns, which might suggest the presence of phosphate in lower amounts. Section 6.6 will present a hypothesis

on the healing mechanism of C_3S-PVA samples in the SBF, based on the provided data.

6.6. Self-healing mechanism hypothesis

Based on the results presented in previous sections, a mechanism for the healing of C_3S-PVA samples in SBF is proposed. Figure 6-32 schematically illustrates the possible sequence of the events taking place in the partially fractured C_3S-PVA cement samples during the healing process in SBF. Figure 6-32a shows simplified schematic microstructure of hydrated C_3S, including hydration products (C-S-H gel and $Ca(OH)_2$) layer around the remnant non-hydrated C_3S particles (round), and white platelet crystals of $Ca(OH)_2$ [76]. Cracks in such system expose unreacted C_3S particles to SBF, thus triggers release of Ca^{2+}, silicates and OH^- ions into the confined microenvironment inside the crack. Based on the results presented in previous sections, the resulting pH in such micro-environment is expected to be relatively high (simulation by using 6cc SBF for fresh paste sample), possibly exceeding pH=11. Such high pH might trigger precipitation of new phases favoured by such high pH. The average pH at the surface of the sample in SBF was changing over the course of the time, from 7.4 at t=0 to 9.2 at t=7 days, which is caused by the further hydration of C_3S as the source of OH^- ion production in the system. There are different phenomena occurring at the same time in the SBF solution (dissolution of C_3S, hydration of C_3S, precipitation of calcium phosphate family and calcium carbonate). This makes it impossible to assume equilibrium for such system to preform any thermodynamic calculations. However, as the stability of PO_4^{-3} ion increases in higher pH (see appendix II), the possibility of hydroxyapatite formation increases. Similar trend is effective for the stability of the CO_3^{-2} (see appendix II).

Figure 6-32b schematically shows the resulting formation of CaP (possibly HA) layer on the surface of the sample and a thicker CaP layer inside of the crack. Figure 6-32c, schematically

shows a later stage in precipitation of calcium carbonate ($CaCO_3$) on the CaP layer after 7 days soaking in SBF, through interaction of the crack micro-environment with the dissolved CO_2 in aqueous solution and from the SBF. Figure 6-32d shows the real SEM image of $CaCO_3$ precipitations within the crack after 7 days soaking.

To further support the proposed mechanism, we should study the differences between the inside of the crack and the surface of the sample, which might lead to the preferential CaP precipitation inside the cracks. There are three main differences between inside part of the crack and the surface of the sample: (1) access to fresh C_3S; (2) physical space limitation (confined environment); and (3) roughness of the inside part of the crack. Each difference will be explained in the following paragraphs.

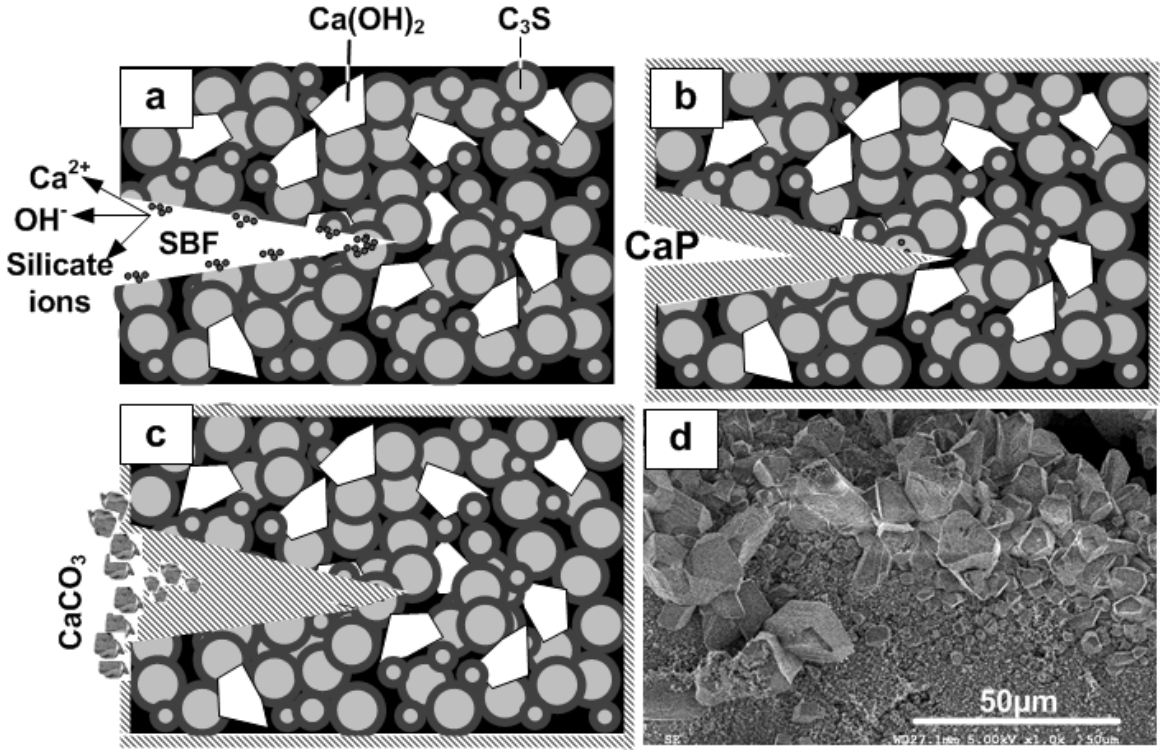

Figure 6-32- Schematic diagram of the proposed self-healing mechanism.

First difference is due to the access to C_3S in the inside surface of the crack. On the outside surface of the sample, the solution has access to C-S-H gel and calcium hydroxide, providing Ca^{+2} and OH^- ions. However, in the inside part of the crack, the solution additionally has access to fresh (non-hydrated) C_3S opened by the propagating crack, which will produce silicate ions and more Ca^{+2} and OH^- ions [76]. The effects of silicon ions on enhancing the healing ability of cementitious materials with higher fraction of fly ash have been confirmed previously [7]. Furthermore, Taylor [76] hypothesized that the silicate ions might have a "poisoning effect" on $Ca(OH)_2$ nuclei, and thus inhibiting the precipitation of $Ca(OH)_2$. Consequently, fresh C_3S will hydrate and produce more OH^- ions (higher pH) within the confined space of the crack. Since these OH^- ions in the presence of silicates do not precipitate as $Ca(OH)_2$, then they will remain available as OH ions and the pH will further increase (as confirmed by pH measurements results). The higher pH creates thermodynamically favourable state for precipitation of CaP (possibly in the form of HA) [51,82].

The second difference is the physical space limitation, which may lead to limited diffusion range within the 10-20 μm wide cracks and thus very significant concentration gradients. Dependence of the healing process on the crack size (width) has been previously confirmed for Engineered Cementitious Composites (ECC) [10], and it appears significant in our work as well. Yu et. al. reported qualitatively that the healing process for ECC is limited to the "tighter" cracks (lower than 50 μm) [10]. This size dependency might confirm the importance of the effects of short-range diffusion in such healing processes. The limited diffusion causes accumulation of the ions and high concentration gradients. This appears more effective, where there is a supply of fresh C_3S to hydrate and produce higher concentration of OH^- ions, as well as silicate ions. A 10-20 μm confined space might cause a higher supersaturation inside the cracks,

but when the crack is large enough this local supersaturation might be overcome by flow of the liquid phase by convection, and faster ionic exchange with the solution outside of the crack. The presence of non-homogeneous nucleation and growth of Calcium Phosphates in samples soaked for 6 hours and 24 hours (Figure 6-14 and Figure 6-16), also suggests the operation of short-range diffusion in this process. However, further information such as *in situ* microanalysis of pH and ion concentrations could help understanding the effect of changes in supersaturation and short-range diffusion in the healing process.

The third difference is the roughness of the inside of the crack, versus the relatively flat outside surface of these samples. If we assume the inside part of the crack has higher specific surface area and roughness than the outside surface of the sample (as supported by SEM), then there is a higher chance for heterogeneous nucleation of new phases inside of the cracks. However, as the C-S-H structure has nano-fibrous or nano-flakes structure with high surface area, and is available on the surface of the sample, the possible effects of higher roughness and surface area inside of the crack requires further investigations.

Any one of the above differences, or a combination of them, could explain the preferred CaP (possibly HA) precipitation inside of the cracks at the early stages of the healing process. As Fig. 5c,d show, the later stage in the healing process appears to be the precipitation of calcite. Due to the limited availability of phosphate ions in the confined space of cracks, calcite starts to precipitate. SEM images in Figure 6-18 show that the calcite prefers to precipitate on the crack mouth rather than the surface of the sample, which previously were covered with CaP film. This might be interpreted as higher tendency of calcite precipitation on the CaP substrate rather than calcium silicate or follow the same rules for the better chance of precipitation inside of the crack because of three mentioned differences.

6.7. Summary

In summary, the proposed mechanism for the crack self-healing in C_3S-PVA samples in SBF consists of CaP precipitation on the surface of the sample and inside of the cracks, wherein the phosphate concentration is higher at the crack edges. Subsequently, carbonate precipitates in form of large calcite crystals or aragonite crystals in the samples soaked for 7 days in SBF and appear to participate in partial restoration of the mechanical properties of the sample. This mechanism, similar to other healing mechanisms in ECCs is dependent on the crack width, i.e. becomes operational in cracks < 50 μm wide.

The healing experiments attempted in samples soaked in water, in our experimental setup with high strain pre-cracking, could not restore the load-carrying capacity of the samples. Instead, deterioration of mechanical properties was observed. This might be explained by the volume increase of calcite precipitation, in absence of CaP "stitching" precipitates. Naus et. al. have reported the transformation of $Ca(OH)_2$ to calcite results in 4% volume increase in Portland cement [175]. This volume increase could lead to internal stresses, responsible for the observed deterioration of mechanical properties. However, we anticipate that the healing could be effective for low strain pre-cracking in water, possibly because less damage is produced in the samples and less calcium carbonate will form.

7. Self-Healing of C_3S-10MCP-PVA Cements

In this chapter, the results of self-healing studies of the C_3S-10MCP-PVA composite cements are reported. Chapter 6 presented the results of studies of self-healing of the C_3S-PVA composites and proposed the healing mechanism operating in samples submerged into Simulated Body Fluid (SBF). In this chapter, results of the self-healing studies of C_3S-10MCP-PVA composites are presented and compared to C_3S-PVA composites. Chapter 5 presented the mechanical properties of C_3S-10MCP-PVA, which on average had 40% lower load bearing capacity in bending than C_3S-PVA (15.4±2.0 N versus 25.6±2.0 N). However, they had similar area under the load-displacement curve (28.5±8.3 N.mm versus 27.5±3.1 N.mm), which is associated with the energy dissipated during the test. The C_3S-10MCP-PVA composites showed capability to withstand higher strains before failure (more than 1.4±0.5 mm, equivalent of 4.1±1.3% strain), as compared to C_3S-PVA composites strains before failure of 0.9±0.4 mm, equivalent of 2.6±1.1% strain). To study self-sealing, it was essential to produce damage cracks in the samples without shattering them completely. Therefore, C_3S-10MCP-PVA composite was a proper candidate to study the self-healing (C_3S-10MCP-PVA were processed with PEG solution as the liquid phase in order to disperse the fibers in the matrix; details on the method to produce the samples can be found in Section 4.1.3).

To pre-crack the samples, the same method as the one described in Chapter 6 was used (details in Section 6.1.1and Section 6.1.2). The three point bending (3PB) behaviour of the pre-cracked samples was studied after soaking them in SBF or distilled water for 7 days. To semi-quantify the changes in load capacity, the healing index with the same formula as described in Section 6.3 was applied.

Section 7.1 presents the 3PB load-displacement curves of C_3S-10MCP- PVA composites and the curves after soaking them for 7 days in SBF or distilled water. Section 7.2 shows SEM images of macro and microstructure, and EDX analysis of the samples after soaking in SBF for 7 days. Section 7.3 and Section 7.4 show XRD analysis and variations of pH upon soaking in SBF. Section 7.5 combines these results and presents a summary on the healing process and ability of C_3S-10MCP- PVA samples.

7.1. Results of three point bend test for C_3S-10MCP-PVA samples, initial loading and loading after soaking for 7 days in SBF or water

Figure 7-1 shows the original load-displacement curves for pre-cracking of C_3S-10MCP-PVA, and loading after soaking them in distilled water for 7 days. The effects of soaking the samples in water (instead in SBF) on their load bearing capacity of the C_3S-10MCP-PVA samples and their associated Healing index (*H*) are considered as a reference test towards subsequent healing the samples in SBF. All samples have small negative *H* value (average = -3.4%), which shows small amount of deterioration in the load-bearing capacity, hence absence of healing. These samples have shown however, significant improvements as compared to the C_3S-PVA samples soaked in water, with the average *H* values = -47%. The absolute values of load-bearing capacity in the C_3S-10MCP-PVA samples are considerably lower than the C_3S-PVA samples (15.4±2.0 N versus 25.6±2.0 N). This was the main reason of defining such dimensionless healing index, to enable comparing two sets of samples with different maximum load capacity.

Figure 7-2 shows the effects of soaking the C_3S-10MCP-PVA samples in SBF. The average *H* value of the curves is 80%, while for C_3S-PVA samples in SBF the average value of *H* was 49% (i.e., the C_3S-10MCP-PVA samples showed higher degree of healing). However, the

absolute values of the load-bearing capacity were lower for the samples containing MCP. As mentioned in the Chapter 2, adding 10wt% MCP to C_3S matrix was expected to increase the strength of the set cement, as confirmed by other researchers [154]. However, our results show that C_3S-10MCP samples had lower compressive and bending strength than C_3S samples (see Sections 5.2 and 5.3). The reaction of MCP particles with CH (Equation 2-3) produces HAp and water molecules. The formation of water can increase strength by providing further hydration in the sample [81]. It can also decrease the strength by producing porosity (confirmed by densitometry results (Table 5-3). Therefore, the higher self-healing ability of C_3S-10MCP-PVA samples could be related to the presence of HAp, in-situ produced water molecules, higher porosity, and reduced CH content or a combination of them.

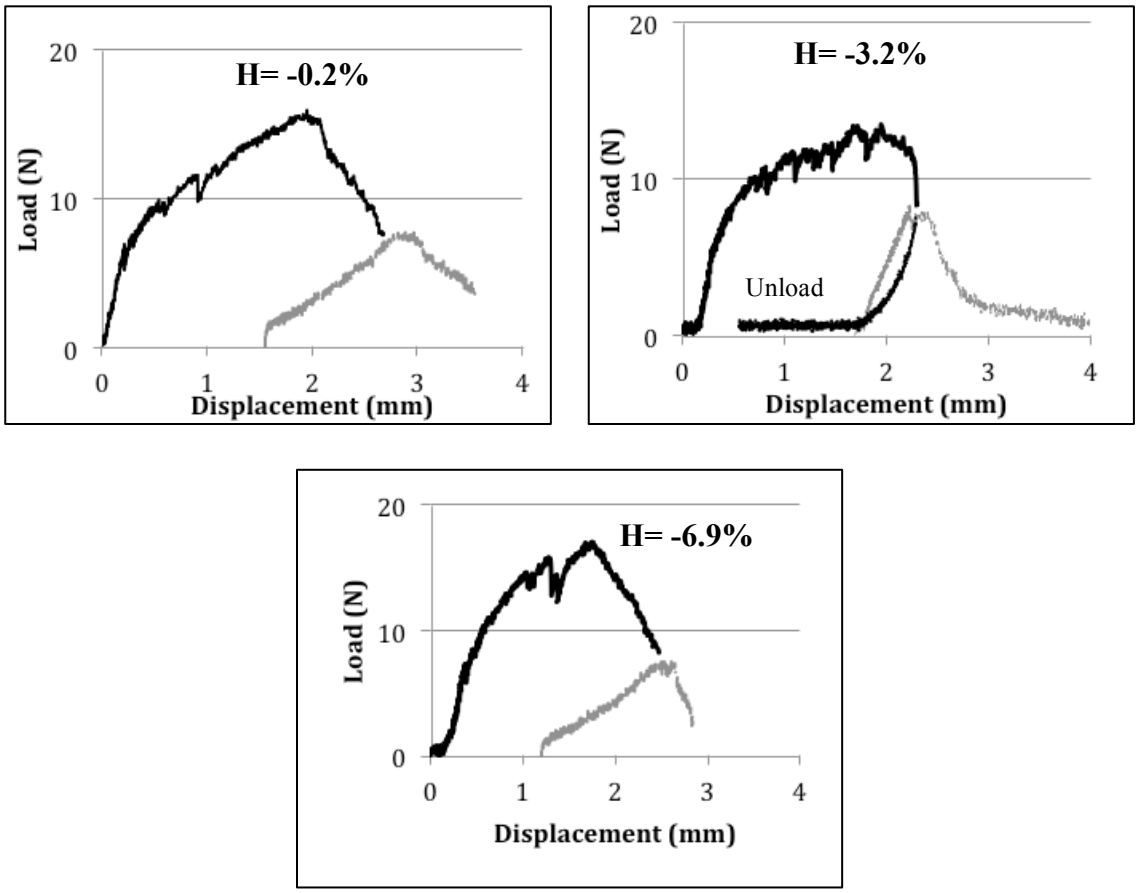

Figure 7-1- 3PB load-displacement curves, including the initial loading and loading after soaking the pre-cracked samples for 7 days in water (dashed grey line is for the samples soaked in water). The Healing Index (HI) of each curve is shown on the graphs.

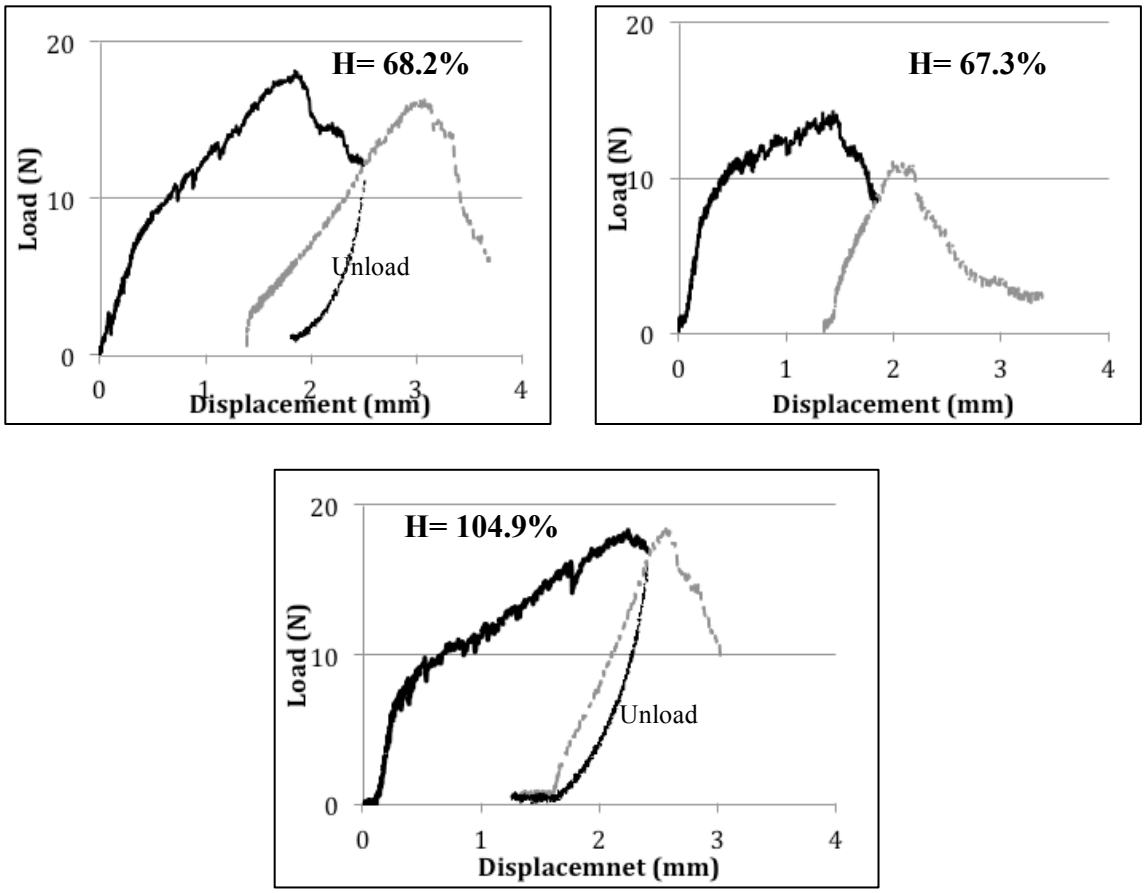

Figure 7-2- 3PB load-displacement curves, including the initial loading and loading after soaking the pre-cracked samples for 7 days in SBF (dashed grey line is for the samples soaked in SBF). The Healing Index (HI) of each curve is shown on the graphs.

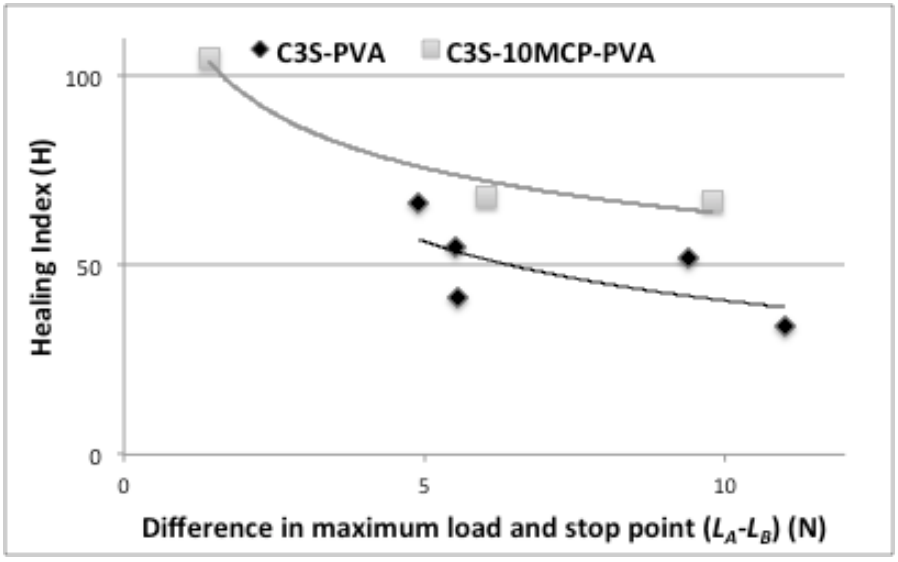

Figure 7-3 Dependence of the healing index on the "L_A-L_B" value.

Figure 7-3 shows the *H* changes versus "L_A-L_B" for C_3S-PVA and C_3S-10MCP-PVA cements. The smaller the "L_A-L_B", the higher is the *H* value and vise versa. The term "L_A-L_B" represents how far loading is continued after reaching the maximum load, equivalent to the degree of damage accumulated in the test sample before the healing treatment. As expected, the higher damage decreases the subsequent healing, possibly due to the cracks width exceeding ~150 μm, the value above which the currently studied healing process was found ineffective.

This observation set the rationale to use a splint to close the crack mouth and decrease the crack width, in order to enable studying the healing process in more details. The use of the splints closed the mouth of the cracks generally <100 μm (see Figure 4-6). However, some loose (spalling) particles detached from the crack surface, might prevent the crack mouth to close to that critical width. The possibility of formation of these spalling particles increases with the degree of damage to the sample. Therefore, the larger the "L_A-L_B", the sample is more damaged and more difficult to heal.

In Chapter 6, we discussed the mechanism of self-healing of the C_3S samples in SBF and proposed the following hypothesis: the phosphate and calcium ions precipitate preferentially within the cracks in the form of a calcium phosphate layer, which then becomes a substrate for further calcium carbonate precipitation. The presented above results can provide two observations to support this hypothesis:

The first observation is the less deterioration in C_3S-10MCP-PVA samples soaked in water as compared to C_3S-PVA samples in water (Healing index (*H*)= -3.4% versus -47.0%). The main difference between these two samples is the presence of Mono calcium phosphate(MCP), which is unstable in pH higher than 2 [51]. Therefore, MCP particles in an

aqueous solution will dissociate into calcium and phosphate ions, thus react with calcium hydroxide and precipitate as calcium phosphate (probably HAp). Such healing scenario would be similar to that operating in SBF-soaked samples. As mentioned in Chapter 6, the material volume increases by carbonation, can lead to internal stress concentration, thus assist in propagation of the cracks, and finally lead to deterioration of the load-carrying capacity in the samples soaked in water. On the other hand, transformation of CH to HAp results in 3% volume reduction [89]. Therefore, in the samples containing MCP, less volume increase is expected and consequently less possibility of additional damage. We anticipate therefore that if more MCP is admixed into the cement matrix, it might be possible to increase the healing ability of these cements in water. This observation remains to be verified, but could be important for non-biological applications of the cements, wherein the structure should be in life-long contact with aqueous solutions. Marine cement structures could be one target for such applications. However, further investigation is required to confirm such effect.

The second observation is the higher Healing Index (H) attained for the C_3S-10MCP-PVA samples in SBF, as compared to the C_3S-PVA samples in SBF (average of H=80% versus H=49%, respectively). Such enhanced healing might be explained by the availability of more phosphate and calcium ions for CaP precipitation within the cracks. In order to further continue discussion about self-healing of C_3S-10MCP-PVA samples, macro and microstructural, and EDX analysis are presented in Section 7.2, 7.3 and 7.4 respectively.

7.2. Macro and microstructure, and EDX analysis of the cement samples after the healing treatments

In this Section, SEM images and their associated EDX mapping or EDX spot analysis are presented. Figure 7-4a-f shows SEM images of the pre-cracked C_3S-10MCP-PVA samples,

soaked for 7 days in SBF. The overall conclusion from these SEM images suggests the main difference with C_3S-PVA samples soaked for 7 days in SBF is the presence of precipitates on the whole surface of the sample in C_3S-10MCP-PVA samples, rather than selective precipitation on the edges of the cracks for C_3S-PVA samples. According to Figure 7-4d,f the fibers were mineralized by the precipitates as well.

Figure 7-5 shows EDX mapping and EDX spot analysis on the pre-cracked C_3S-10MCP-PVA sample, soaked for 7 days in SBF. SEM image in Figure 7-5a shows a flower-like phase on the crack edge, which is rich in calcium and oxygen. If we assume it a calcium carbonate, then based on the available data in literature [176], this flower-like shape is similar to aragonite (one of the polymorphs of calcium carbonate) [176]. Further phase analysis is required to determine the exact crystallographic phase.

Figure 7-6 shows EDX mapping and EDX spot analysis of the image in Figure 7-4f. The average EDX result of the whole picture (mapping) shows the dominant chemical elements are oxygen and calcium. Small amounts of Si and P are visible, but this might be due to the surface penetration of the electron beam (collecting data from the deeper underneath layers). There are no preferential accumulations of Si or P observed in the EDX mapping (Figure 7-6b,c).

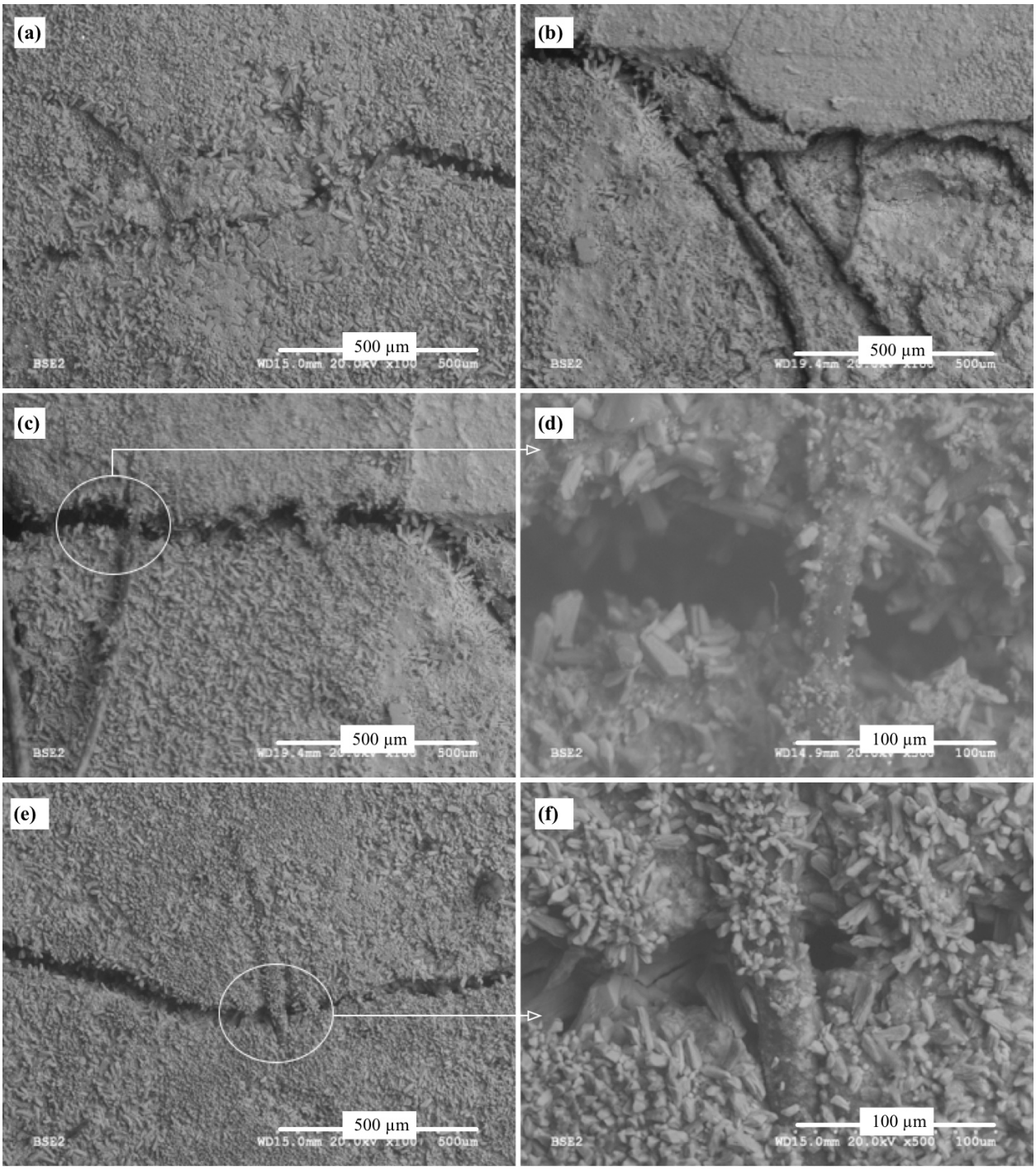

Figure 7-4- SEM images of the C_3S-10MCP-PVA samples, soaked for 7 days in SBF.

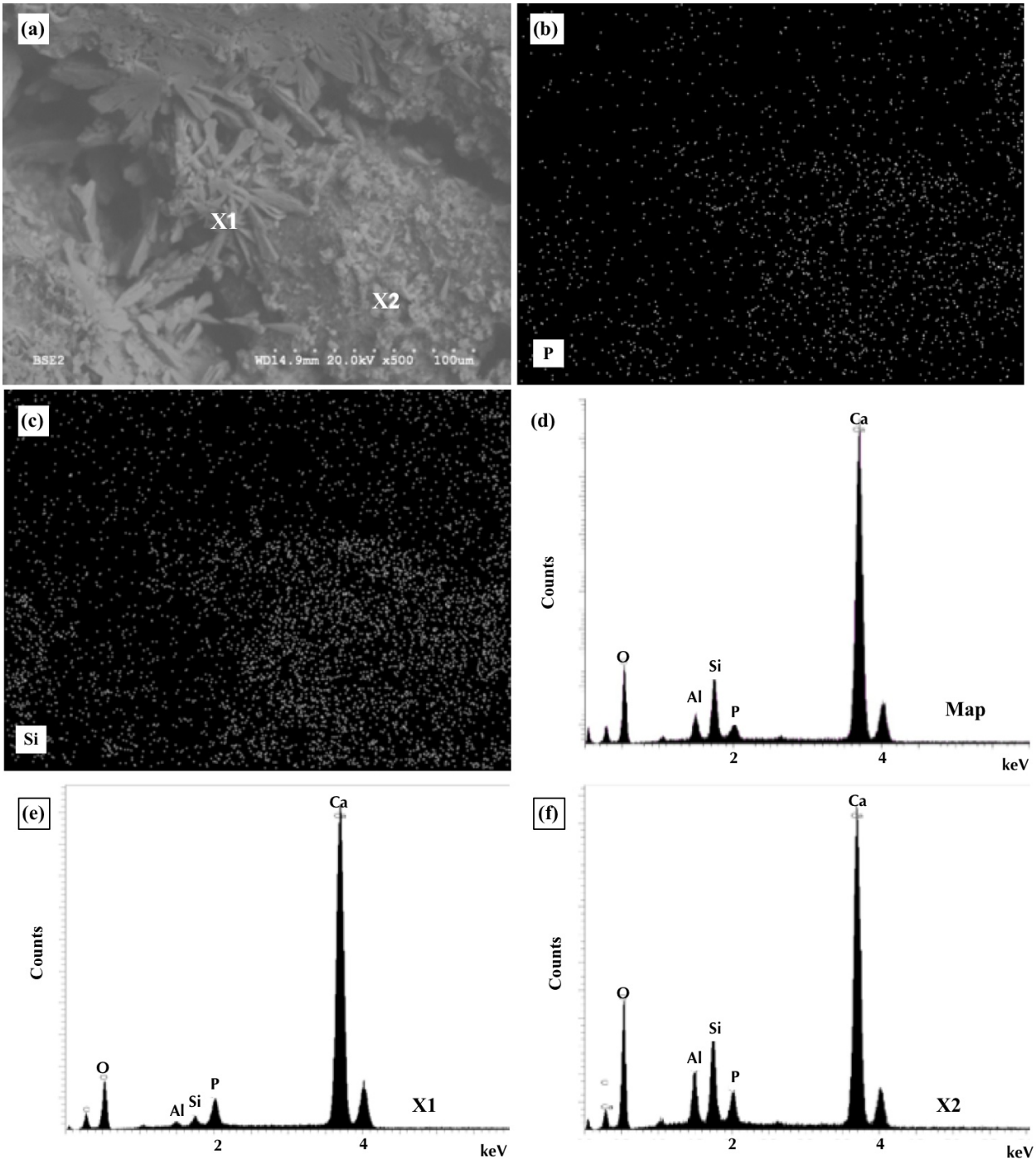

Figure 7-5- EDX mapping and EDX spot analysis on the C_3S-10MCP-PVA sample, soaked for 7 days in SBF.

Figure 7-7 shows EDX mapping and EDX spot analysis of the surface of the C_3S-10MCP-PVA sample (away from the main macro crack), soaked for 7 days in SBF. No flower-like calcium carbonate phases were observed on the surface of these samples. The semi-cubical prism structure, both in morphology and EDX analysis is similar to the calcite phase, detected on the surface of C_3S-PVA samples soaked for 7 days in SBF. The substrate layer (spot X3, marked in Figure 7-7a and the EDX result in Figure 7-7d) contains calcium, silicon and phosphor elements, representing calcium silicate and calcium phosphate availability. Therefore, similar to the results presented in Chapter 6, we might also conclude that the calcium carbonate precipitates on top of the calcium silicate and calcium phosphate layers.

Higher concentration of phosphorus and silicon deficiency was observed along the crack edge in C_3S-PVA samples (Section 6.4), but a similar trend for C_3S-10MCP-PVA samples was not detected. The whole surface of the samples containing MCP is covered with the precipitates, including the crack edge. In EDX analysis on the surface of the samples, lower amount of Si and P was observed in general (Si = 0.44-4.0 wt%, P = 0.41-1.75wt%) than the reported concentration of Si and P in C_3S-PVA samples soaked for 7 days in SBF (Si = 1.78-6.33 wt% , P = 1.84-3.12 wt%). Lower amount of P detected for C_3S-10MCP-PVA samples. Considering the fact that C_3S-10MCP-PVA samples have 10 wt% calcium phosphate in their matrix, lower amount of P detected might be caused by the formation of a thicker calcium carbonate phase on top of the calcium phosphate layer.

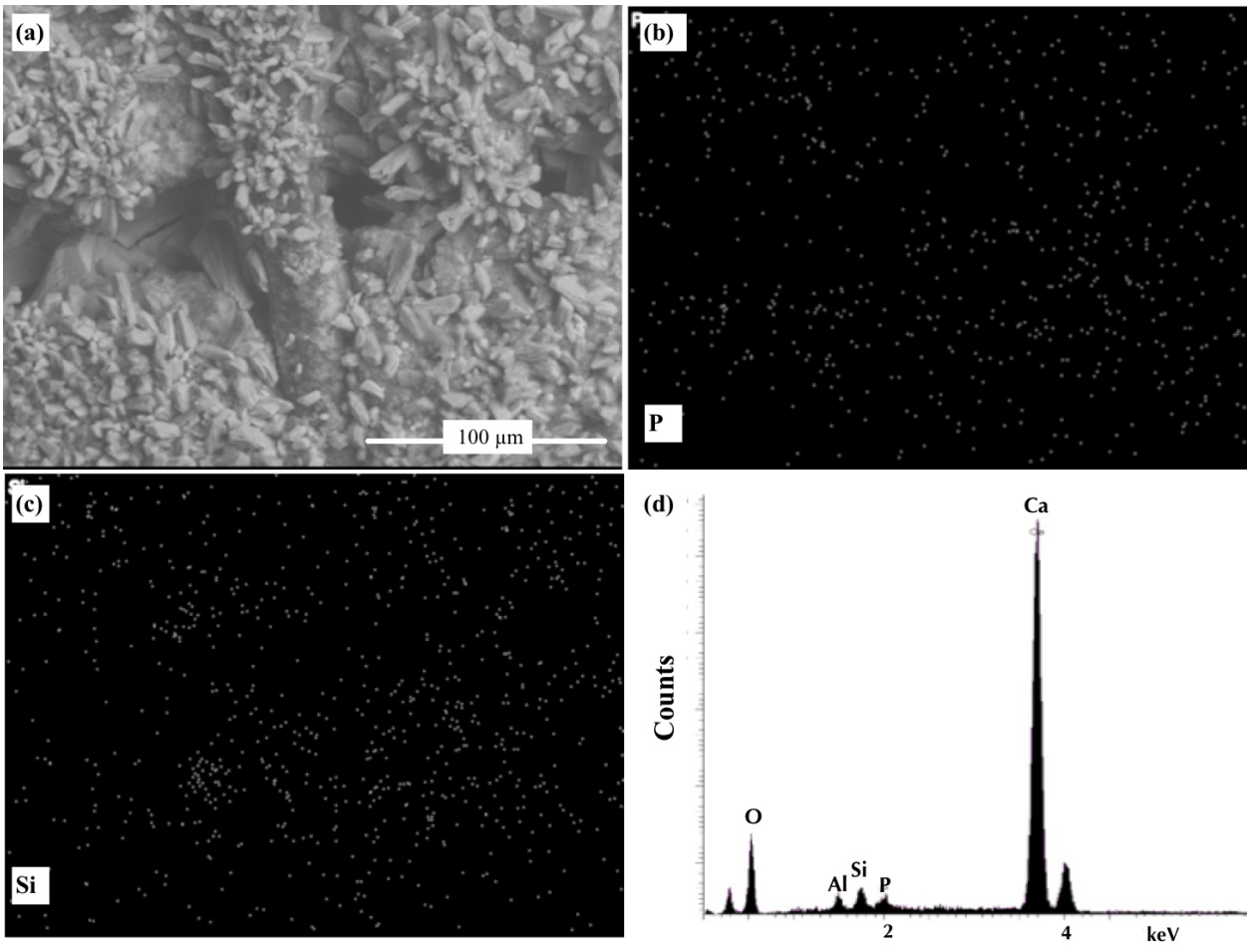

Figure 7-6- EDX mapping on the C_3S-10MCP-PVA sample, soaked for 7 days in SBF.

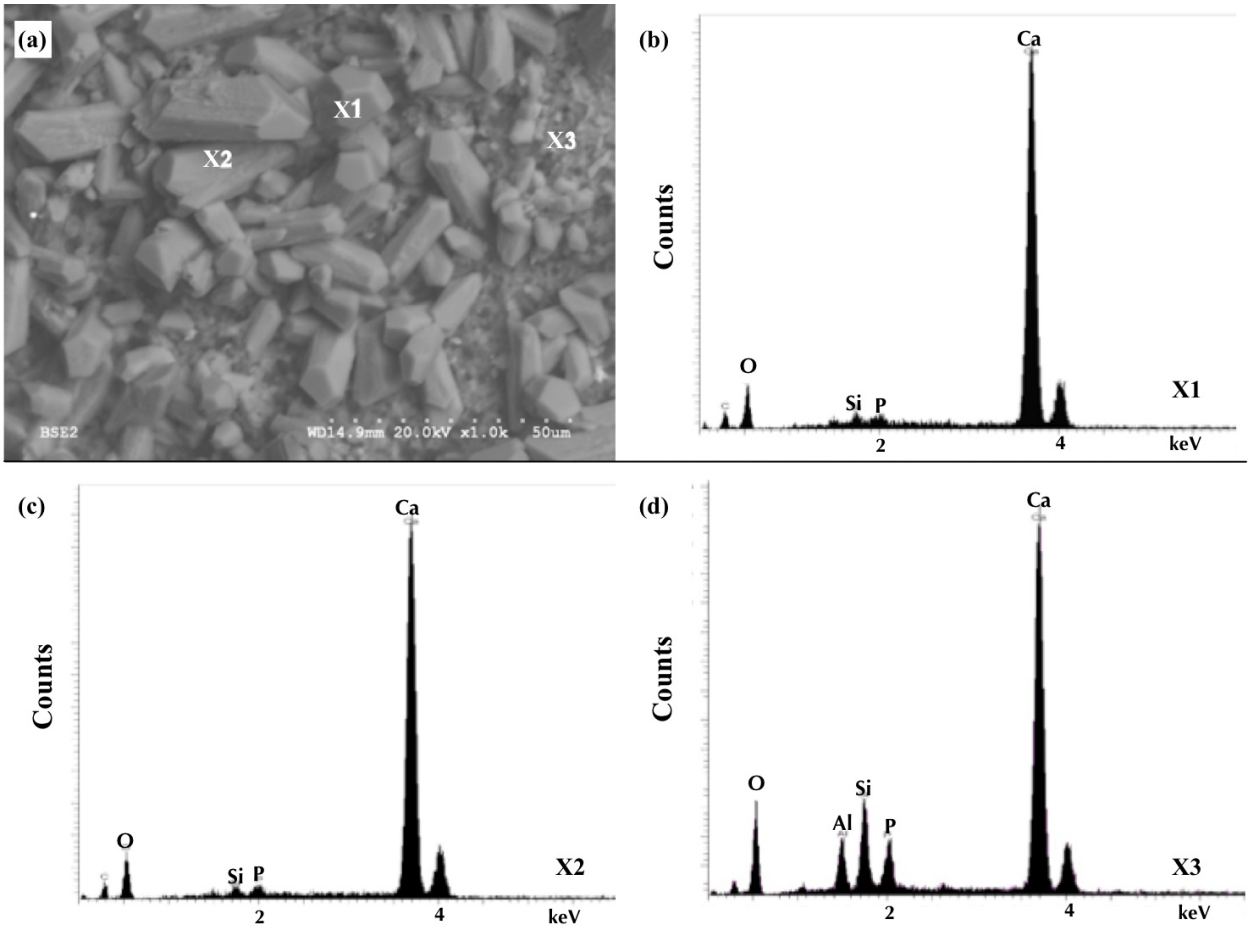

Figure 7-7- EDX spot analysis on the C_3S-10MCP-PVA sample, soaked for 7 days in SBF.

In Chapter 6, the precipitates were characterized as calcite on the C_3S-PVA surface after soaking for 7 days in SBF. The EDX and morphology of the semi-cubical prism phase (Figure 7-7) observed on C_3S-10MCP-PVA surface are similar to those for the precipitates on the C_3S-PVA surface. In addition, most parameters of the two systems are also similar. Therefore, this semi-cubical prism calcium carbonate phase on the surface of C_3S-10MCP-PVA samples appears to be calcite. There are some flower-like phases precipitated at the edge of the crack that resemble aragonite crystals. We could not identify calcium phosphate phase on the surface of C_3S-10MCP-PVA samples after 7 days soaking in SBF. It might be available in the substrate but

has been covered by the calcium carbonate. The phase analysis by XRD, and the pH values of C_3S-10MCP samples are presented in the following Sections (7.3 and 7.4). They provide some preliminary results supporting proposed future research (Chapter 9). The summary and conclusion for this Chapter is presented in Section 7.5.

7.3. XRD analysis

In this section, phase analysis of the C_3S-10MCP samples by XRD is presented. Figure 7-8 shows XRD patterns of: (a) C_3S-10MCP powder, (b) C_3S-10MCP sample, set for 10 days in distilled water, and (c) C_3S-10MCP sample set for 10 days in water and soaked in SBF for 7 days. The C_3S-10MCP powder pattern shows combination of C_3S and MCP peaks. As the C_3S is the dominant phase and small amount of MCP is available, the MCP peaks have much lower intensities than C_3S peaks. In C_3S-10MCP sample set for 10 days in water (Figure 7-8b), intensities of C_3S peaks are lowered and Portlandite phase is available in the form of sharp peaks with relatively high intensity. MCP peaks are not visible anymore in the XRD pattern of set sample, as MCP is not stable in pH>2 [51] and hydroxyapatite (HAp) peaks in low intensity are detected.

The XRD pattern for C_3S-10MCP set sample, soaked in SBF (Figure 7-8c) shows similar peaks to C_3S-10MCP set sample (Figure 7-8b). The main difference is lower intensities of Portlandite peaks and higher intensities of HAp peaks. However, in both patterns, three main peaks of HAp are masked by C_3S peaks: HAp peaks are located at 2theta = 31.8, 32.2, 32.9 degrees and C_3S peaks at 2theta=32.1, 32.5, 32.7 degrees, as indicated in the patterns. Due to further hydration of unreacted C_3S, the intensity of C_3S peaks should decrease or remain the same. Therefore, the increase in the intensity of the multiple broad peaks at 2theta range between 30 degree to 33 degree show the effect of HAp peaks in this range. The overlap of these six

peaks has formed the broad peak at this range. The peak at 2theta= 29.58 degree is associated with C-S-H structure by other researchers [81].

HAp is the most thermodynamically stable phase of calcium phosphates in solutions with pH higher than 6.5 [51]. As indicated in the pattern, the set sample before soaking in SBF has some small amount of HAp present in its structure. When soaked in SBF, the HAp phase inside of the set sample could act as seeds for nucleation of the new HAp phase and promote formation of more HAp.

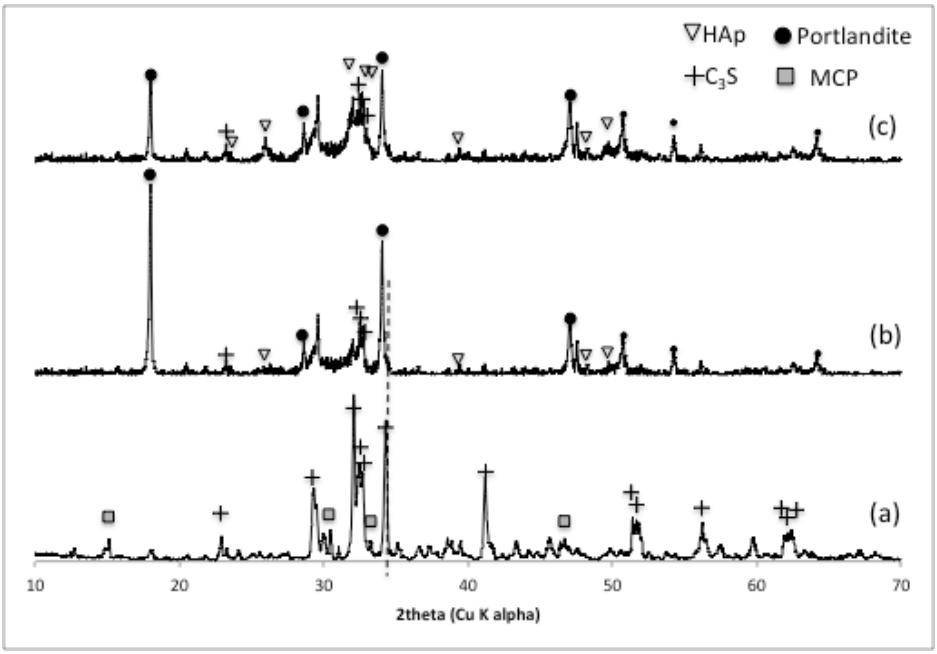

Figure 7-8- XRD pattern of (a) C_3S-10MCP powder, (b) C_3S-10MCP sample set for 10 days, (c) C_3S-10MCP sample set for 10 days and then soaked for 7 days in SBF.

7.4. pH variation within cement paste samples

To compare the pH values of C_3S-10MCP samples with C_3S samples, we used the same method to measure pH as for C3S paste (i.e. soaked fresh paste in the minimum volume of SBF

possible in our experimental setup, 6cc; (see Section 4.2.4 for details). Figure 7-9a and Figure 7-9b show results of pH variation versus time for C_3S-10MCP paste samples soaked in SBF in two scales (minutes and hours, respectively). Figure 7-9c shows pH variation for 10 day set C3S-10MCP samples, which are soaked in SBF (the horizontal axis shows the time of soaking in SBF). Table 6-1 and Figure 7-10 compare the results of C_3S-10MCP with their C_3S counterparts.

The C_3S-10MCP samples show lower pH values in both paste form and set form. There might be two reasons for this: i) Lower amount of remnant C_3S is available, as initially 10wt% of the C_3S powder were substituted by MCP. CH is one of the by-products of C_3S hydration, thus, less amount of remnant C_3S available means less amount of CH is produced by its further hydration; ii) Lower amount of CH is available to leach and dissolve in the SBF, as some of the CH has reacted with MCP to produce HAp; MCP is the most acidic member of calcium phosphate family. The reaction between MCP and CH (Equation 2-3) describes an acid/base reaction, resulting in formation of a salt (HAp) and water molecules. Therefore, addition of MCP lowers the concentration of OH^- ions and consequently lowers the pH.

C_3S-10MCP paste samples had significantly higher pH than the set samples (e.g. more than 2 pH units after 7 days soaking in SBF). However, the pH values for the paste samples are high because of the low amount of solution used for measurement. As mentioned before, by using the minimum amount of solution possible for the paste samples, the confined space inside of the crack is simulated to study the local pH changes. It should be considered that the pH values for paste samples are expected to be lower in a setup with higher amount of solution (i.e. instead of using 6cc, using 50cc SBF, same as the setup for the set samples) than the presented data.

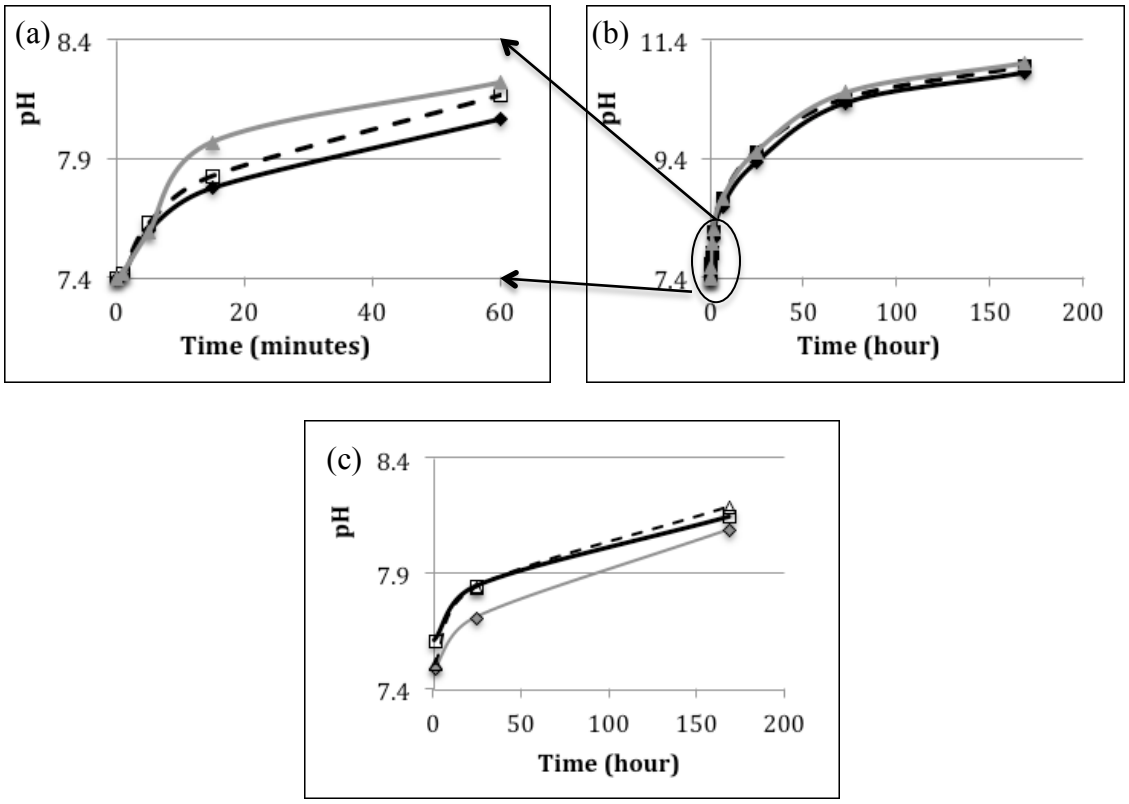

Figure 7-9- pH results of (a) and (b) C_3S-10MCP-paste soaked in SBF, different scale (3 lines for 3 different samples).

Table 7-1- pH values of C_3S-10MCP-paste soaked in SBF

Soaking time in SBF	1 hour	1 day	7 days
C_3S-10MCP paste soaked in 6 cc SBF	8.2	9.5	10.9
C_3S paste soaked in 6 cc SBF	8.3	10.3	11.9
C_3S-10MCP set sample soaked in 50 cc SBF	7.5	7.8	8.1
C_3S set sample soaked in 50 cc SBF	7.7	8.3	9.2

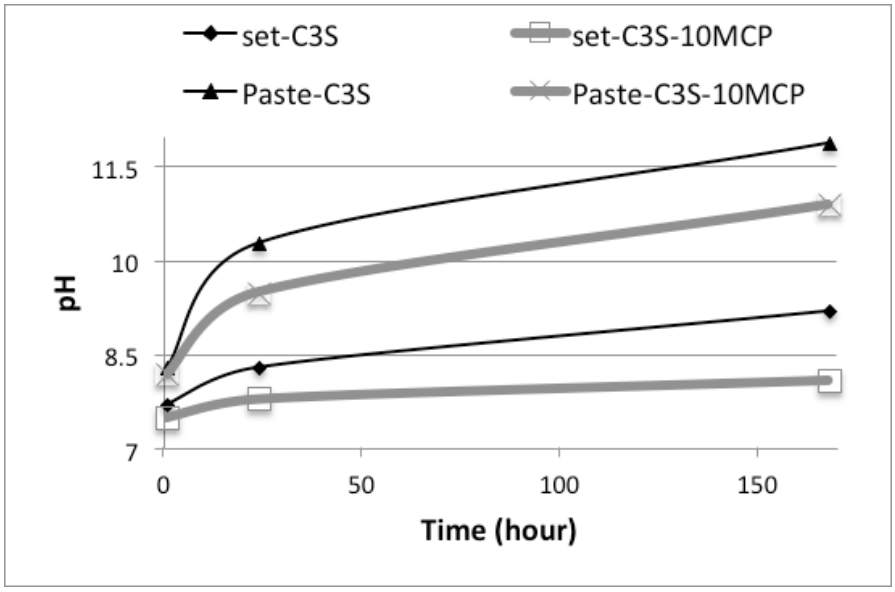

Figure 7-10- Summary of pH values for C_3S and C_3S-10MCP paste and 10-day-set samples soaked in SBF.

7.5. Summary

The load-bearing capacity of the damaged (pre-cracked) C_3S-10MCP-PVA samples after soaking in distilled water was close to the point that the test was stopped for the original, non-healed samples (Figure 7-1). Their average healing index (*H*) was therefore relatively small, i.e. -3.4%. In Chapter 6 we observed that for the pre-cracked C_3S-PVA samples, the load-bearing capacity after soaking 7 days in water was significantly lower than the stop point for the original, non-healed samples and their average *H* value was -47%. One of the reasons for deterioration of these C_3S cements could be the leaching (dissolution) of CH into water, which increases the porosity and subsequently decreases their load-bearing capacity. The other reason could be the precipitation of calcium carbonate inside of the cracks. As the transformation of CH to calcium carbonate leads to 4% volume increase, stress concentration at the tip of the crack could cause deterioration in the load-bearing capacity of the samples. It seems that the addition of 10wt%

MCP to the composite cements prevented such deterioration. As mentioned earlier, MCP can react with CH to produce HAp and thus strengthen the structure of the composite (as CH is considered as the "weak link" of set hydraulic cements [2]). Therefore, less CH is leaching into the water for these materials. We anticipate that by increasing the MCP content in the cements, this healing mechanism could be also enhanced. Also, heavily pre-cracked C_3S-10MCP-PVA samples maintained their load-bearing capacity after soaking in water for 7 days. Therefore, it might be possible that they would heal in lower-strain pre-cracked samples. The recommended future research on this topic can be found in Chapter 9.

Pre-cracked C_3S-10MCP-PVA samples showed self-healing ability when soaked in SBF for 7 days (Figure 7-2). Their average healing index (*H*) value was 80%, which is considerably higher than for the C_3S-PVA samples (*H*=49%). However, as the calculation of *H* is only semi-quantitative, more precise quantitative studies are required to compare the healing abilities of the different cementitious composites. The proposed mechanism for crack self-healing of C_3S-PVA samples in SBF (Section 6.5) might be active and effective for C_3S-10MCP-PVA samples as well. The pH of the paste samples, simulating the inside environment of the crack, is 10.9 (i.e. one unit lower than for the C_3S, 11.9). The SBF solution has access to unreacted C3S exposed through the damage process during sample loading. Thus, inside of the crack is a favourable site for the nucleation of the calcium phosphate phases and most probably also for HAp. As shown by XRD analysis (Figure 7-8), some HAp is present in the C_3S-10MCP-PVA samples set for 10 days in water, and higher amount of HAp is available in the set sample soaked for 7 days in SBF (Figure 7-8b,c). The HAp available in the set sample could also act as seeds for formation of new HAp phase after soaking in SBF.

According to the EDX mapping results for C_3S-10MCP-PVA samples soaked in SBF, unlike C_3S samples, phosphorus concentration is not higher at the cracks edges. The calcium carbonate precipitation was observed on the whole surface of C_3S-10MCP-PVA samples; while in C_3S-PVA samples it precipitated around the edges of the cracks (where higher concentration of phosphor was available). Therefore, we might conclude that the phosphate containing sites on the surface of the sample (e.g. HAp) might act as nucleation sites and provide favourable substrate for calcium carbonate precipitation. Another possibility is precipitation of carbonated apatite instead of stoichiometric apatite on the surface of the samples. Further studies are required to evaluate such possibility.

In summary, C_3S-10MCP-PVA samples showed the healing ability *in vitro*, resulting in restoration of the load-bearing capacity in 3PB with the healing index of about 80%. They have higher self-healing ability after exposure to SBF and less deterioration of the load-bearing capacity after exposure to water, compared to C_3S-PVA samples. They have also lower pH values in SBF and have higher content of HAp in their structure after soaking in SBF for 7 days. These results are in accordance with other studies about higher biocompatibility and bioactivity of C_3S-10MCP samples [81]. These new research results on the healing ability of ceramic composite bio-cements suggest new fields of studies for self-healing calcium silicate phosphate bone cements, for restoration of their superior mechanical and biological properties. On the other hand, these findings could be also implemented in construction industry for inducement and enhancement of self-healing of fiber reinforced concrete structures for underwater applications. Suggestions for such future research, as well as further required investigations to explain the self-healing phenomena of C_3S-10MCP-PVA samples in SBF, are presented in Chapter 9.

8. Conclusions

The following conclusions are drawn from the presented research results:

1. The self-healing behavior of bioceramic cements in the Simulated Body Fluid (SBF) environment has been investigated in this thesis for the first time. In particular, the partially-damaged (cracked) composite C3S-PVA samples showed self-healing behavior when soaked in SBF. After 7 days of soaking in SBF at 37 °C, most of the cracks were visually (i.e. when observed from sample surface) eliminated. Supporting evidence of the healing was demonstrated through the partial restoration of the load-bearing capacity of the cements in three-point-bending tests. The test results also disclosed the fact that reference cement samples soaked in water show lower degree of crack healing and their load-bearing capacity is deteriorated. However, this is a pioneering research and further studies including statistical analysis are required to extend these results to practical applications.

2. The crack self-healing mechanism is proposed to include Calcium Phosphate (CaP) precipitation preferentially on the crack edges and inside of the cracks, thus re-bonding the cracks surfaces. It has been observed that during the healing treatment CaP precipitates grow on both surfaces of the crack, then connect and "stitch" the crack. Subsequently, calcium carbonate precipitates mostly on the CaP substrate. The preferential precipitation of CaP at edges and inside of the cracks might be caused by:

i) Access to the fresh (un-hydrated) C_3S particles exposed to the micro-environment inside of the crack; such particles are exposed by the propagating crack and while

hydrating they temporarily elevate the local pH values to pH>11, which promotes local CaP precipitation. In that sense we could hypothesize a "smart" behaviour of such composite cement, i.e. the healing process focuses preferentially on the damaged sections of the material.

ii) Higher supersaturation in confined space inside of the cracks. It has been observed that the cracks of width lower than ~50 μm healed nearly entirely, while the larger cracks (50-150 μm) healed only partially. This might emphasize the role of the short-range diffusion and lack of convection inside of the smaller cracks. While the effect of crack width on the healing progress was well recorded, elucidation of the underlying mechanisms needs to be pursued in future work (Chapter 9).

iii) Higher roughness of the freshly-fractured surface increasing the rate of heterogeneous nucleation of CaP.

3. The partially damaged composite C_3S-PVA reference samples soaked in water did not show CaP precipitates within the cracks, but did show substantial deposits of calcite in the cracks vicinity. The loss of load-bearing capacity of these reference samples might be explained by the volume increase due to calcite precipitation, in absence of CaP "stitching" precipitates. Such behaviour might emphasize more on the constructive role of CaP in healing of such composites.

4. The reference composite cements with the addition of Mono Calcium Phosphate (C_3S-10MCP-PVA samples, prepared and tested the same way as C_3S-PVA) also showed self-healing

behavior when soaked in SBF. After 7 days of soaking in SBF at 37 °C, most of the cracks were visually eliminated and the load-bearing capacity in three-point-bend tests was partially restored. The reference C_3S-10MCP-PVA samples soaked in water did not show any deterioration in their load-bearing capacity, which might indicate the constructive effect of CaP in the healing mechanism of calcium silicate based composites.

5. Semi-quantitative analysis of the degree of self-healing calculated based on the restoration of load-bearing capacity and was expressed through a dimensionless "healing index". The C_3S-10MCP-PVA samples showed higher degree of restoration of load carrying capacity than the C_3S-PVA samples (healing index of 80% vs 49%). The C_3S-10MCP-PVA samples soaked in water showed much smaller loss of load-bearing capacity as compared to C_3S-PVA (i.e. healing index of -3.5% vs -47% respectively). It is anticipated that the MCP component of the composite cements provided some degree of healing through MCP dissolution leading to CaP re-precipitation inside the cracks with high local pH.

6. The higher healing index of C_3S-10MCP-PVA in SBF and their much lower healing index deterioration in water, as compared to C_3S-PVA, elucidates the important role of calcium phosphates in the healing abilities of bioceramic cement composites. We conclude that providing calcium phosphate either in form of ions available in SBF or dispersed particles inside the paste (MCP) improves the healing behavior of the composites. This observation could be extended to other cementitious composites, including structural cement materials containing e.g. dispersed MCP particles, and promises a potential for accelerated self-healing of cementitious materials in

the presence of calcium phosphate phases. These pioneering results indicate a great opportunity for both biological and non-biological applications of such composites and require more quantitative and statistical analysis to clarify the extent of available benefits in each application.

7. To our knowledge, this is the first report on mechanical properties of fiber reinforced Calcium Phosphate-Silicate Cements, in particular C_3S-10MCP-PVA, as compared to C_3S-PVA. PVA fiber reinforcement was extremely effective in increasing toughness of both C_3S-PVA and C_3S-10MCP-PVA. The fracture energy absorbed before failure, measured by the area under the load-displacements curves of three-point-bend tests, was ~60 times higher in C_3S-PVA samples than plain (unreinforced) C_3S samples. In C_3S-10MCP samples, the energy absorbed before failure was ~80 times higher than that for the plain C_3S-10MCP samples.

In three-point-bend tests, C_3S-10MCP-PVA samples reached higher displacement (proportional to strain) before failure than C_3S-PVA samples. Damage tolerance is one of the important characteristics of the natural tissues such as bone, and provides delayed or non-catastrophic failure. In addition, such significant improvement in toughness enabled producing of heavily cracked sample for the self-healing studies. As confirmed by the microstructural analysis, such toughening was attained by fiber-bridging, fiber-pull-out and deformation of the fibers. Fiber reinforcement also significantly increased the load-bearing capacity of the cements in bending and compression.

9. Future Work

This work presents pioneering observations on the self-healing behavior of composite bioceramic cements in laboratory environment. It is however recognized that the process and responsible mechanisms understanding is only preliminary and largely hypothetical. Moreover, no attempt was made to extend the investigation to *in-vitro* and *in-vivo* environments at this stage. The following experiments are therefore recommended for the future studies:

- In order to achieve better understanding on the self-healing process, the process parameters should be varied (and their effects studied) in organized and systematic way. Some of these parameters include different sizes/concentrations of the PVA fibers (including systematic change both in diameter and length); different concentration of the available phosphate ions by either increasing the calcium phosphate content or refreshing the SBF or using 2xSBF (doubling the ion concentrations); the effect of other available ions in SBF such as Mg, Na, Cl and K; using specific concentration of CO_2 to mimic the *in vivo* environment during the healing treatments.
- Evaluation of the healing behaviour of the samples in low strain pre-cracking (i.e. limited damage conditions). In ECCs, for low strain pre-cracked samples soaked in water, the healing is still effective (e.g. ~0.3% strain instead of 3% used in this work). The possibility of healing in low strain pre-cracked samples could lead to substantial self-healing in water and possibly total restoration of the load carrying capacity of the cements in SBF. However, such studies require producing samples with less variation in the maximum load-bearing capacity. Increasing the number of specimens, improved methods of sample preparation,

and statistical analysis on mechanical properties can improve quantifying the restoration of the mechanical properties.

- Quantifying the dependency of the crack healing on the crack width. Predefined crack width, such as 5, 20, 50, 100, 150, 200 μm, could be produced e.g. through variable-load indentation; study their healing behavior in water and SBF.
- Biological evaluation of the self-healing should include *in vitro* cell culture studies. As the bacteria showed accelerated effect on the healing mechanism for ECCs due to the effect of their metabolites, the animal cells might show similar accelerating effects. If positive results are obtained from the cell culture tests, *in vivo* tests should follow. For orthopaedic applications, if the cracks widths are larger than 100 μm, it will allow bone ingrowth. If the cracks are smaller, the composite will be healed through mineral precipitation. Therefore, we anticipate healing would be enhanced *in vivo*.
- Degradation behaviour studies of the healed samples, in SBF or PBS, serum and water. Determine the weight loss, congruent or incongruent dissolution by measuring concentration of the different ions in the solution.
- Long-term evaluation of the load carrying capacity of the healed cements. As CSCs and CPSCs in orthopaedic applications would remain in the body for a long time, one of their characteristics that might be of great interest is their ability to increase their strength over time.
- The proposed healing process in the presence of phosphate ions might be considered and studied further for structural applications, e.g. in the construction industry. In such studies Portland cement based composites and scaled-up samples should be evaluated to determine

the effects of adding calcium phosphates or self-healing behavior in phosphate containing solutions (such as waste waters).

- Considering that the loads in nature are usually cyclic, it is of paramount importance to study the effect of cyclic loading and fatigue on the self-healing behavior of calcium silicate and calcium phosphate silicate composites for bone cements and bone substitute applications. The number of the cycles, the maximum strain/load, and the length of the cycles are considered some of the factors affecting the healing ability of these composites. Therefore, Such results can provide vital information for the final applications.

A number of limitations of the reported studies were encountered, which may be addressed in the future work. This includes operator dependency of the sample preparations and lack of statistical analysis due to the pioneering nature of the research, new systems for processing, analyzing and quantifying and fixed timing. The composites for the purpose of present work were processed through hand mixing. This is a simple method, but results in variations in sample properties and requires achieving expertise to reproduce the samples. Another limitation is the size of the samples in regards to the size of the fibers. The cross-section of the three-point-bend samples studied here was 3x4mm, while the PVA fibers are 6 mm long. Although homogeneous distribution of the fibers in the cements in 2D was examined, 3D distribution of the fibers in the matrix was not possible to achieve.

References

[1] JP Brockes. Amphibian limb regeneration: rebuilding a complex structure. Science. 1997;276:81-7.

[2] H Jonkers. Self healing concrete: a biological approach. Self Healing Materials. 2008:195-204.

[3] M Li, VC Li. Cracking and Healing of Engineered Cementitious Composites under Chloride Environment. ACI Mater J. 2011;108:333.

[4] VC Li, C Wu, S Wang, A Ogawa, T Saito. Interface tailoring for strain-hardening polyvinyl alcohol-engineered cementitious composite (PVA-ECC). ACI Materials Journal-American Concrete Institute. 2002;99:463-72.

[5] VC Li, E Yang. Self healing in concrete materials. SPRINGER SERIES IN MATERIALS SCIENCE. 2007;100:161.

[6] S Qian, J Zhou, M De Rooij, E Schlangen, G Ye, K Van Breugel. Self-healing behavior of strain hardening cementitious composites incorporating local waste materials. Cement and Concrete Composites. 2009;31:613-21.

[7] P Termkhajornkit, T Nawa, Y Yamashiro, T Saito. Self-healing ability of fly ash-cement systems. Cement and Concrete Composites. 2009;31:195-203.

[8] KS Toohey, NR Sottos, JA Lewis, JS Moore, SR White. Self-healing materials with microvascular networks. Nat Mater. 2007;6:581-5.

[9] M Wu, B Johannesson, M Geiker. A review: Self-healing in cementitious materials and engineered cementitious composite as a self-healing material. Constr Build Mater. 2012;28:571-83.

[10] JH Yu, W Chen, MX Yu, YE Hua. The microstructure of self-healed PVA ECC under wet and dry cycles. Materials Research. 2010;13:225-31.

[11] VC Li. Bendable Composites—ductile concrete for structures. Structure Magazine. 2006;45.

[12] VC Li, EH Yang. Engineered self healing cementitious composites. U.S. Patent No. 7,572,501. 11 Aug. 2009.

[13] TC Mauldin, JD Rule, NR Sottos, SR White, JS Moore. Self-healing kinetics and the stereoisomers of dicyclopentadiene. Journal of The Royal Society Interface. 2007;4:389-93.

[14] J Luo, DM Skrzypiec, P Pollintine, MA Adams, DJ Annesley-Williams, P Dolan. Mechanical efficacy of vertebroplasty: influence of cement type, BMD, fracture severity, and disc degeneration. Bone. 2007;40:1110-9.

[15] W Zhao, J Chang, J Wang, W Zhai, Z Wang. In vitro bioactivity of novel tricalcium silicate ceramics. J Mater Sci Mater Med. 2007;18:917-23.

[16] NJ Coleman, K Awosanya, JW Nicholson. Aspects of the in vitro bioactivity of hydraulic calcium (alumino) silicate cement. Journal of Biomedical Materials Research Part A. 2009;90:166-74.

[17] T Kokubo, H Takadama. How useful is SBF in predicting in vivo bone bioactivity?. Biomaterials. 2006;27:2907-15.

[18] AM Kenny, KM Prestwood. OSTEOPOROSIS:: Pathogenesis, Diagnosis, and Treatment in Older Adults. Rheumatic Disease Clinics of North America. 2000;26:569-91.

[19] MK Heran, GM Legiehn, PL Munk. Current concepts and techniques in percutaneous vertebroplasty. Orthop Clin North Am. 2006;37:409,34.

[20] LL Hench, JR Jones. Biomaterials, artificial organs and tissue engineering CRC Press; 2005.

[21] A Bernhardt, A Lode, S Boxberger, W Pompe, M Gelinsky. Mineralised collagen—an artificial, extracellular bone matrix—improves osteogenic differentiation of bone marrow stromal cells. J Mater Sci Mater Med. 2008;19:269-75.

[22] JB Park. Biomaterials science and engineering Plenum Press New York; 1984.

[23] ID Learmonth, C Young, C Rorabeck. The operation of the century: total hip replacement. The Lancet. 2007;370:1508-19.

[24] JF Shackelford. Bioceramics CRC Press; 1999.

[25] J Charnley. The bonding of prostheses to bone by cement. J Bone Joint Surg Br. 1964;46:518-29.

[26] MJ Yaszemski. Biomaterials in orthopedics CRC Press; 2004.

[27] YH An, RA Draughn. Mechanical testing of bone and the bone-implant interface CRC; 2000.

[28] S Masala, M Mammucari, G Angelopoulos, R Fiori, F Massari, S Faria, G Simonetti. Percutaneous vertebroplasty in the Management of vertebral osteoporotic fractures. Short-term, mid-term and long-term follow-up of 285 patients. Skeletal Radiol. 2009;38:863-9.

[29] HJ Cloft, DN Easton, ME Jensen, DF Kallmes, JE Dion. Exposure of medical personnel to methylmethacrylate vapor during percutaneous vertebroplasty. Am J Neuroradiol. 1999;20:352-3.

[30] G Lewis. Injectable bone cements for use in vertebroplasty and kyphoplasty: State‐of‐the‐art review. Journal of Biomedical Materials Research Part B: Applied Biomaterials. 2006;76:456-68.

[31] P Habibovic, U Gbureck, CJ Doillon, DC Bassett, CA van Blitterswijk, JE Barralet. Osteoconduction and osteoinduction of low-temperature 3D printed bioceramic implants. Biomaterials. 2008;29:944-53.

[32] R Huiskes, R Ruimerman, GH Van Lenthe, JD Janssen. Effects of mechanical forces on maintenance and adaptation of form in trabecular bone. Nature. 2000;405:704-6.

[33] A Lee. Properties of Bone Cement: The mechanical properties of PMMA Bone Cement. Breusch SJ, Malchau H, Edrs.The Well-Cemented Total Hip Arthroplasty.Heidelburg: Springer. 2005:60-6.

[34] W Higgs, P Lucksanasombool, R Higgs, M Swain. Comparison of the material properties of PMMA and glass-ionomer based cements for use in orthopaedic surgery. J Mater Sci Mater Med. 2001;12:453-60.

[35] C Wang, R Pilliar. Fracture toughness of acrylic bone cements. J Mater Sci. 1989;24:3725-38.

[36] R Murugan, S Ramakrishna. Development of nanocomposites for bone grafting. Composites Sci Technol. 2005;65:2385-406.

[37] G Chiara, F Letizia, F Lorenzo, S Edoardo, S Diego, S Stefano, B Eriberto, Z Barbara. Nanostructured Biomaterials for Tissue Engineered Bone Tissue Reconstruction. International journal of molecular sciences. 2012;13:737-5.

[38] J Black. Biological performance of materials: fundamentals of biocompatibility CRC Press; 2006.

[39] SJ Ding, MY Shie, CY Wang. Novel fast-setting calcium silicate bone cements with high bioactivity and enhanced osteogenesis in vitro. J.Mater.Chem. 2009;19:1183-90.

[40] JD Bronzino. The biomedical engineering handbook CRC Pr I Llc; 2000.

[41] S Fujibayashi, M Neo, HM Kim, T Kokubo, T Nakamura. Osteoinduction of porous bioactive titanium metal. Biomaterials. 2004;25:443-50.

[42] N Sarkar, R Caicedo, P Ritwik, R Moiseyeva, I Kawashima. Physicochemical basis of the biologic properties of mineral trioxide aggregate. J Endod. 2005;31:97-100.

[43] H Zhong, L Wang, Y Fan, L He, K Lin, W Jiang, J Chang, L Chen. Mechanical properties and bioactivity of [beta]-Ca2SiO4 ceramics synthesized by spark plasma sintering. Ceram Int. 2011.

[44] HH Beherei, GT El-Bassyouni, KR Mohamed. Modulation, characterization and bioactivity of new biocomposites based on apatite. Ceram Int. 2008;34:2091-7.

[45] T Kokubo. Bioactive glass ceramics: properties and applications. Biomaterials. 1991;12:155-63.

[46] M Bohner, J Lemaitre. Can bioactivity be tested in vitro with SBF solution?. Biomaterials. 2009;30:2175-9.

[47] H Pan, X Zhao, BW Darvell, WW Lu. Apatite-formation ability-Predictor of. Acta Biomaterialia. 2010;6:4181-8.

[48] Q Lin, X Lan, Y Li, Y Yu, Y Ni, C Lu, Z Xu. Anti-washout carboxymethyl chitosan modified tricalcium silicate bone cement: preparation, mechanical properties and in vitro bioactivity. J Mater Sci Mater Med. 2010:1-12.

[49] S Labbaf, O Tsigkou, KH Muller, MM Stevens, AE Porter, JR Jones. Spherical bioactive glass particles and their interaction with human mesenchymal stem cells in vitro. Biomaterials. 2010.

[50] JD Laredo, B Hamzé. Complications of percutaneous vertebroplasty and their prevention. Skeletal Radiol. 2004;33:493-505.

[51] SV Dorozhkin. Calcium orthophosphates in nature, biology and medicine. Materials. 2009;2:399-48.

[52] QQ Hoang, F Sicheri, AJ Howard, DSC Yang. Bone recognition mechanism of porcine osteocalcin from crystal structure. Nature. 2003;425:977-80.

[53] M Nakano, N Hirano, M Zukawa, K Suzuki, J Hirose, T Kimura, Y Kawaguchi. Vertebroplasty Using Calcium Phosphate Cement for Osteoporotic Vertebral Fractures: Study of Outcomes at a Minimum Follow-up of Two Years. Asian Spine Journal. 2012;6:34.

[54] M Bohner, U Gbureck, J Barralet. Technological issues for the development of more efficient calcium phosphate bone cements: a critical assessment. Biomaterials. 2005;26:6423-9.

[55] M Bohner. Calcium orthophosphates in medicine: from ceramics to calcium phosphate cements. Injury. 2000;31:D37-4.

[56] C Canal, M Ginebra. Fibre-reinforced calcium phosphate cements: A review. Journal of the Mechanical Behavior of Biomedical Materials. 2011.

[57] M Parirokh, M Torabinejad. Mineral trioxide aggregate: a comprehensive literature review--Part III: Clinical applications, drawbacks, and mechanism of action. J Endod. 2010;36:400-13.

[58] HW Roberts, JM Toth, DW Berzins, DG Charlton. Mineral trioxide aggregate material use in endodontic treatment: a review of the literature. Dental Materials. 2008;24:149-64.

[59] JF Reyes-Carmona, MS Felippe, WT Felippe. Biomineralization ability and interaction of mineral trioxide aggregate and white Portland cement with dentin in a phosphate-containing fluid. J Endod. 2009;35:731-6.

[60] I Islam, H Kheng Chng, AU Jin Yap. Comparison of the physical and mechanical properties of MTA and Portland cement. J Endod. 2006;32:193-7.

[61] M Torabinejad, T Watson, TR Pitt Ford. Sealing ability of a mineral trioxide aggregate when used as a root end filling material. J Endod. 1993;19:591-5.

[62] G Krastl, N Allgayer, P Lenherr, A Filippi, P Taneja, R Weiger. Tooth discoloration induced by endodontic materials: a literature review. Dental Traumatology. 2012.

[63] LK Bakland, JO Andreasen. Will mineral trioxide aggregate replace calcium hydroxide in treating pulpal and periodontal healing complications subsequent to dental trauma? A review. Dental Traumatology. 2012.

[64] BA Loushine, TE Bryan, SW Looney, BM Gillen, RJ Loushine, RN Weller, DH Pashley, FR Tay. Setting properties and cytotoxicity evaluation of a premixed bioceramic root canal sealer. J Endod. 2011;37:673-7.

[65] H Zhang, Y Shen, ND Ruse, M Haapasalo. Antibacterial Activity of Endodontic Sealers by Modified Direct Contact Test Against Enterococcus faecalis. J Endod. 2009;35:1051-5.

[66] W Zhang, Z Li, B Peng. Ex vivo cytotoxicity of a new calcium silicate–based canal filling material. Int Endod J. 2010;43:769-74.

[67] W Lai, J Garino, P Ducheyne. Silicon excretion from bioactive glass implanted in rabbit bone. Biomaterials. 2002;23:213-7.

[68] H Yuan, JD de Bruijn, X Zhang, CA van Blitterswijk, K de Groot. Bone induction by porous glass ceramic made from Bioglass®(45S5). J Biomed Mater Res. 2001;58:270-6.

[69] J Moura, LN Teixeira, C Ravagnani, O Peitl, ED Zanotto, MM Beloti, H Panzeri, AL Rosa, PT de Oliveira. In vitro osteogenesis on a highly bioactive glass‐ceramic (Biosilicate®). Journal of Biomedical Materials Research Part A. 2007;82:545-57.

[70] A El-Ghannam. Bone reconstruction: from bioceramics to tissue engineering. Expert review of medical devices. 2005;2:87-101.

[71] MY Shie, SJ Ding, HC Chang. The role of silicon in osteoblast-like cell proliferation and apoptosis. Acta Biomaterialia. 2011.

[72] PE Keeting, MJ Oursler, KE Wiegand, SK Bonde, TC Spelsberg, BL Riggs. Zeolite a increases proliferation, differentiation, and transforming growth factor β production in normal adult human osteoblast‐like cells in vitro. Journal of Bone and Mineral Research. 1992;7:1281-9.

[73] W Cheng, H Li, J Chang. Fabrication and characterization of β-dicalcium silicate/poly (d, l-lactic acid) composite scaffolds. Mater Lett. 2005;59:2214-8.

[74] W Zhao, J Wang, W Zhai, Z Wang, J Chang. The self-setting properties and in vitro bioactivity of tricalcium silicate. Biomaterials. 2005;26:6113-21.

[75] S Ni, J Chang, L Chou, W Zhai. Comparison of osteoblast‐like cell responses to calcium silicate and tricalcium phosphate ceramics in vitro. Journal of Biomedical Materials Research Part B: Applied Biomaterials. 2007;80:174-83.

[76] HFW Taylor. Cement chemistry Thomas Telford Services Ltd; 1997.

[77] PC Hewlett. Lea's chemistry of cement and concrete A Butterworth-Heinemann Title; 2004.

[78] Z Huan, J Chang. Study on physicochemical properties and in vitro bioactivity of tricalcium silicate–calcium carbonate composite bone cement. J Mater Sci Mater Med. 2008;19:2913-8.

[79] Z Huan, J Chang. Novel tricalcium silicate/monocalcium phosphate monohydrate composite bone cement. Journal of Biomedical Materials Research Part B: Applied Biomaterials. 2007;82:352-9.

[80] D Lu, S Zhou. High strength biological cement composition and using the same. 2009.

[81] S Zhou, J Ma, Y Shen, M Haapasalo, ND Ruse, Q Yang, T Troczynski. In vitro studies of calcium phosphate silicate bone cements. J Mater Sci Mater Med. 2013;24:355-64.

[82] SV Dorozhkin. Biphasic, triphasic and multiphasic calcium orthophosphates. Acta Biomaterialia. 2011.

[83] C Liu, Y Huang, W Shen, J Cui. Kinetics of hydroxyapatite precipitation at pH 10 to 11. Biomaterials. 2001;22:301-6.

[84] J Meyer, E Eanes. A thermodynamic analysis of the amorphous to crystalline calcium phosphate transformation. Calcif Tissue Int. 1978;25:59-68.

[85] SV Dorozhkin, M Epple. Biological and medical significance of calcium phosphates. Angewandte Chemie International Edition. 2002;41:3130-46.

[86] KP Chong, EJ Garboczi. Smart and designer structural material systems. Progress in Structural Engineering and Materials. 2002;4:417-30.

[87] Z Huan, J Chang. Calcium–phosphate–silicate composite bone cement: self-setting properties and in vitro bioactivity. J Mater Sci Mater Med. 2009;20:833-41.

[88] J Li, Z Qiu, L Zhou, T Lin, Y Wan, S Wang, S Zhang. Novel calcium silicate/calcium phosphate composites for potential applications as injectable bone cements. Biomedical Materials. 2008;3:044102.

[89] D Naus, CH Mattus, LR Dole, Oak Ridge National Laboratory, US Nuclear Regulatory Commission. Office of Nuclear Regulatory Research. Final Report, Assessment of Potential Phosphate Ion-cementitious Materials Interactions US Nuclear Regulatory Commission, Office of Nuclear Regulatory Research; 2007.

[90] JK Kim, YW Mai. Engineered interfaces in fiber reinforced composites Elsevier Science; 1998.

[91] S Peters. Handbook of composites Springer; 1997.

[92] L Chow. Next generation calcium phosphate-based biomaterials. Dent Mater J. 2009;28:1.

[93] N Gorst, Y Perrie, U Gbureck, A Hutton, M Hofmann, L Grover, J Barralet. Effects of fibre reinforcement on the mechanical properties of brushite cement. Acta Biomaterialia. 2006;2:95-102.

[94] LA Dos Santos, LC De Oliveira, EC da Silva Rigo, RG Carrodéguas, AO Boschi, AC Fonseca de Arruda. Fiber reinforced calcium phosphate cement. Artif Organs. 2000;24:212-6.

[95] R Krüger, J Groll. Fiber reinforced calcium phosphate cements–On the way to degradable load bearing bone substitutes?. Biomaterials. 2012.

[96] HHK Xu, FC Eichmiller, AA Giuseppetti. Reinforcement of a self‐setting calcium phosphate cement with different fibers. J Biomed Mater Res. 2000;52:107-14.

[97] X Wang, J Ye, Y Wang, L Chen. Reinforcement of Calcium Phosphate Cement by Bio‐Mineralized Carbon Nanotube. J Am Ceram Soc. 2007;90:962-4.

[98] KK Chew, KL Low, SH Sharif Zein, DS McPhail, LC Gerhardt, JA Roether, AR Boccaccini. Reinforcement of calcium phosphate cement with multi-walled carbon nanotubes and bovine serum albumin for injectable bone substitute applications. Journal of the mechanical behavior of biomedical materials. 2011;4:331-9.

[99] N Nezafati, F Moztarzadeh, S Hesaraki, M Mozafari. Synergistically reinforcement of a self-setting calcium phosphate cement with bioactive glass fibers. Ceram Int. 2011;37:927-34.

[100] Y Greish, P Brown. Characterization of wollastonite‐reinforced HAp–Ca polycarboxylate composites. J Biomed Mater Res. 2001;55:618-2.

[101] HHK Xu, DT Smith, CG Simon. Strong and bioactive composites containing nano-silica-fused whiskers for bone repair. Biomaterials. 2004;25:4615-26.

[102] FA Müller, U Gbureck, T Kasuga, Y Mizutani, JE Barralet, U Lohbauer. Whisker‐Reinforced Calcium Phosphate Cements. J Am Ceram Soc. 2007;90:3694-7.

[103] LA dos Santos, RG Carrodeguas, AO Boschi, AC Fonseca de Arruda. Fiber‐enriched double‐setting calcium phosphate bone cement. Journal of Biomedical Materials Research Part A. 2003;65:244-50.

[104] Y Zuo, F Yang, JGC Wolke, Y Li, JA Jansen. Incorporation of biodegradable electrospun fibers into calcium phosphate cement for bone regeneration. Acta Biomaterialia. 2010;6:1238-47.

[105] HHK Xu, JB Quinn. Calcium phosphate cement containing resorbable fibers for short-term reinforcement and macroporosity. Biomaterials. 2002;23:193-202.

[106] EF Burguera, HHK Xu, S Takagi, LC Chow. High early strength calcium phosphate bone cement: effects of dicalcium phosphate dihydrate and absorbable fibers. Journal of Biomedical Materials Research Part A. 2005;75:966-75.

[107] HHK Xu, CG Simon Jr. Self‐hardening calcium phosphate composite scaffold for bone tissue engineering. Journal of orthopaedic research. 2004;22:535-43.

[108] HHK Xu, EF Burguera, LE Carey. Strong, macroporous, and< i> in situ-setting calcium phosphate cement-layered structures. Biomaterials. 2007;28:3786-9.

[109] MD Weir, HHK Xu. Human bone marrow stem cell-encapsulating calcium phosphate scaffolds for bone repair. Acta biomaterialia. 2010;6:4118-26.

[110] Y Zhang, HHK Xu. Effects of synergistic reinforcement and absorbable fiber strength on hydroxyapatite bone cement. Journal of Biomedical Materials Research Part A. 2005;75:832-40.

[111] P Banfill, G Starrs, G Derruau, W McCarter, T Chrisp. Rheology of low carbon fibre content reinforced cement mortar. Cement and Concrete Composites. 2006;28:773-80.

[112] M Hossain, T Sakai. Flexural behavior of carbon fiber cement composites. 2006.

[113] N Banthia, J Sheng. Fracture toughness of micro-fiber reinforced cement composites. Cement and Concrete Composites. 1996;18:251-69.

[114] VC Li. On engineered cementitious composites (ECC). Journal of advanced concrete technology. 2003;1:215-30.

[115] VC Li, S Wang, C Wu. Tensile strain-hardening behavior of polyvinyl alcohol engineered cementitious composite (PVA-ECC). ACI Materials Journal-American Concrete Institute. 2001;98:483-92.

[116] VC Li, T Kanda. Engineered cementitious composites for structural applications. J Mater Civ Eng. 1998;10:66-9.

[117] VC Li, DK Mishra, AE Naaman, JK Wight, JM LaFave, HC Wu, Y Inada. On the shear behavior of engineered cementitious composites. Adv Cem Based Mater. 1994;1:142-9.

[118] MD Hager, P Greil, C Leyens, S van der Zwaag, US Schubert. Self‐Healing Materials. Adv Mater. 2010;22:5424-30.

[119] S Zwaag, AJM Schmets, G van der Zaken, L MyiLibrary. Self healing materials: an alternative approach to 20 centuries of materials science Springer; 2007.

[120] RP Wool. Self-healing materials: a review. Soft Matter. 2008;4:400-18.

[121] R Wool, K Oconnor. A theory crack healing in polymers. J Appl Phys. 1981;52:5953-6.

[122] C Lin, S Lee, K Liu. Methanol‐Induced crack healing in poly (methyl methacrylate). Polymer Engineering & Science. 1990;30:1399-406.

[123] SR White, N Sottos, P Geubelle, J Moore, MR Kessler, S Sriram, E Brown, S Viswanathan. Autonomic healing of polymer composites. Nature. 2001;409:794-7.

[124] B Blaiszik, M Caruso, D McIlroy, J Moore, S White, N Sottos. Microcapsules filled with reactive solutions for self-healing materials. Polymer. 2009;50:990-7.

[125] GO Wilson, JW Henderson, MM Caruso, BJ Blaiszik, PJ McIntire, NR Sottos, SR White, JS Moore. Evaluation of peroxide initiators for radical polymerization‐based self‐healing applications. Journal of Polymer Science Part A: Polymer Chemistry. 2010;48:2698-70.

[126] R Trask, I Bond. Biomimetic self-healing of advanced composite structures using hollow glass fibres. Smart Mater Struct. 2006;15:704.

[127] J Pang, IP Bond. 'Bleeding composites'—damage detection and self-repair using a biomimetic approach. Composites Part A: Applied Science and Manufacturing. 2005;36:183-8.

[128] SJ Kalista Jr, TC Ward, Z Oyetunji. Self-healing of poly (ethylene-co-methacrylic acid) copolymers following projectile puncture. Mechanics of advanced materials and structures. 2007;14:391-7.

[129] NR Sottos, JS Moore. Materials chemistry: Spot-on healing. Nature. 2011;472:299-300.

[130] P Biggs, L Jones, B Wellborn, G Lewis. A Self-healing PMMA Bone Cement: Influence of Crystal Size of Grubbs' Catalyst. 2009:147-50.

[131] C Dry. Matrix cracking repair and filling using active and passive modes for smart timed release of chemicals from fibers into cement matrices. Smart Mater Struct. 1994;3:118.

[132] C Dry, W McMillan. Three-part methylmethacrylate adhesive system as an internal delivery system for smart responsive concrete. Smart Mater Struct. 1996;5:297.

[133] VC Li, YM Lim, YW Chan. Feasibility study of a passive smart self-healing cementitious composite. Composites Part B: Engineering. 1998;29:819-27.

[134] S van der Zwaag, N van Dijk, H Jonkers, S Mookhoek, W Sloof. Self-healing behaviour in man-made engineering materials: bioinspired but taking into account their intrinsic character. Philosophical Transactions of the Royal Society A: Mathematical, Physical and Engineering Sciences. 2009;367:1689-704.

[135] J Zhang, X Ju. Investigation on stress-crack opening relationship of engineered cementitious composites using inverse approach. Cem Concr Res. 2011.

[136] M Şahmaran, VC Li. Engineered Cementitious Composites. Transportation Research Record: Journal of the Transportation Research Board. 2010;2164:1-8.

[137] M Lepech, VC Li. Water permeability of cracked cementitious composites. 2005:20-5.

[138] M Maalej, VC Li. Introduction of strain-hardening engineered cementitious composites in design of reinforced concrete flexural members for improved durability. ACI Struct J. 1995;92.

[139] M Maalej, T Hashida, VC Li. Effect of fiber volume fraction on the off-crack-plane fracture energy in strain-hardening engineered cementitious composites. J Am Ceram Soc. 1995;78:3369-75.

[140] M Maalej, VC Li. Flexural/tensile-strength ratio in engineered cementitious composites. J Mater Civ Eng. 1994;6:513-28.

[141] S Wang, VC Li. Polyvinyl alcohol fiber reinforced engineered cementitious composites: material design and performances. 2005:65-74.

[142] S Wang, VC Li. Engineered cementitious composites with high-volume fly ash. ACI Materials Journal-American Concrete Institute. 2007;104:233-41.

[143] K Sisomphon, O Copuroglu, E Koenders. Self-healing of surface cracks in mortars with expansive additive and crystalline additive. Cement and Concrete Composites. 2012.

[144] E Boquet, A Boronat, A Ramos-Cormenzana. Production of calcite (calcium carbonate) crystals by soil bacteria is a general phenomenon. 1973.

[145] Q Chunxiang, W Jianyun, W Ruixing, C Liang. Corrosion protection of cement-based building materials by surface deposition of CaCO3 by Bacillus pasteurii. Materials Science and Engineering: C. 2009;29:1273-80.

[146] HM Jonkers, E Schlangen. Crack repair by concrete immobilized bacteria. 2007;7.

[147] H Jonkers. Bacteria-based self-healing concrete. Heron. 2011;56:1.

[148] W De Muynck, D Debrouwer, N De Belie, W Verstraete. Bacterial carbonate precipitation improves the durability of cementitious materials. Cem Concr Res. 2008;38:1005-14.

[149] W De Muynck, N De Belie, W Verstraete. Microbial carbonate precipitation in construction materials: A review. Ecol Eng. 2010;36:118-36.

[150] SS Bang, JK Galinat, V Ramakrishnan. Calcite precipitation induced by polyurethane-immobilized Bacillus pasteurii. Enzyme Microb Technol. 2001;28:404-9.

[151] HM Jonkers, A Thijssen, G Muyzer, O Copuroglu, E Schlangen. Application of bacteria as self-healing agent for the development of sustainable concrete. Ecol Eng. 2010;36:230-5.

[152] CW Yang, TS Lui. Kinetics of hydrothermal crystallization under saturated steam pressure and the self-healing effect by nanocrystallite for hydroxyapatite coatings. Acta Biomaterialia. 2009;5:2728-37.

[153] S Lamaka, M Zheludkevich, K Yasakau, R Serra, S Poznyak, M Ferreira. Nanoporous titania interlayer as reservoir of corrosion inhibitors for coatings with self-healing ability. Progress in organic coatings. 2007;58:127-35.

[154] D Lu, S Zhou. Hydraulic cement compositions and methods of making and using the same. U.S. Patent No. 8,343,271. 1 Jan. 2013.

[155] A Bentur, S Mindess. Fibre reinforced cementitious composites Taylor & Francis; 2006.

[156] C Redon, VC Li, C Wu, H Hoshiro, T Saito, A Ogawa. Measuring and modifying interface properties of PVA fibers in ECC matrix. J Mater Civ Eng. 2001;13:399-406.

[157] P Weidinger, W Blum, U Hunsche, A Hampel. The influence of friction on plastic deformation in compression tests. physica status solidi (a). 1996;156:305-1.

[158] N Ruse, T Troczynski, M MacEntee, D Feduik. Novel fracture toughness test using a notchless triangular prism (NTP) specimen. J Biomed Mater Res. 1996;31:457-63.

[159] F Bencardino. Mechanical Parameters and Post-Cracking Behaviour of HPFRC according to Three-Point and Four-Point Bending Test. Advances in Civil Engineering. ;2013.

[160] I Knets, V Krilova, R Cimdins, L Berzina, V Vitins. Stiffness and strength of composite acrylic bone cements. Journal of Achievements in Materials and Manufacturing Engineering. 2007;20:135-8.

[161] M Jarcho, C Bolen, M Thomas, J Bobick, J Kay, RH Doremus. Hydroxylapatite synthesis and characterization in dense polycrystalline form. J Mater Sci. 1976;11:2027-35.

[162] J Cao, D Chung. Carbon fiber reinforced cement mortar improved by using acrylic dispersion as an admixture. Cem Concr Res. 2001;31:1633-7.

[163] KL Scrivener, A Nonat. Hydration of cementitious materials, present and future. Cem Concr Res. 2011;41:651-65.

[164] L Raki, J Beaudoin, L Mitchell. Layered double hydroxide-like materials: nanocomposites for use in concrete. Cem Concr Res. 2004;34:1717-24.

[165] X Fu, W Lu, D Chung. Improving the bond strength between carbon fiber and cement by fiber surface treatment and polymer addition to cement mix. Cem Concr Res. 1996;26:1007-12.

[166] T Horikoshi, A Ogawa, T Saito, H Hoshiro, G Fischer, V Li. Properties of Polyvinylalcohol fiber as reinforcing materials for cementitious composites. 2006:147.

[167] M Sakai, R Bradt. Fracture toughness testing of brittle materials. International Materials Reviews. 1993;38:53-78.

[168] RE Smallman, RJ Bishop. Modern physical metallurgy and materials engineering Butterworth-Heinemann; 1999.

[169] JF Shackelford. Introduction to materials science for engineers. 2004.

[170] AP Fantilli, H Mihashi, P Vallini. Multiple cracking and strain hardening in fiber-reinforced concrete under uniaxial tension. Cem Concr Res. 2009;39:1217-29.

[171] T Kanda, S Watanabe, VC Li. Application of pseudo strain hardening cementitious composites to shear resistant structural elements. AEDIFICATIO Publishers, Fracture Mechanics of Concrete Structures,. 1998;3:1477-90.

[172] Y Yang, EH Yang, VC Li. Autogenous healing of engineered cementitious composites at early age. Cem Concr Res. 2011;41:176-83.

[173] Y Yang, MD Lepech, EH Yang, VC Li. Autogenous healing of engineered cementitious composites under wet–dry cycles. Cem Concr Res. 2009;39:382-90.

[174] R Rogue, W Lerch. Hydration of Portland cement compounds. Industrial & Engineering Chemistry. 1934;26:837-4.

[175] D Naus, CH Mattus, LR Dole, Oak Ridge National Laboratory, US Nuclear Regulatory Commission. Office of Nuclear Regulatory Research. Final Report, Assessment of Potential Phosphate Ion-cementitious Materials Interactions US Nuclear Regulatory Commission, Office of Nuclear Regulatory Research; 2007.

[176] H Imai, T Terada, T Miura, S Yamabi. Self-organized formation of porous aragonite with silicate. J Cryst Growth. 2002;244:200-5.

[177] JL Hutter, J Bechhoefer. Banded spherulitic growth in a liquid crystal. J Cryst Growth. 2000;217:332-43.

[178] L Gránásy, T Pusztai, G Tegze, JA Warren, JF Douglas. Growth and form of spherulites. Physical Review E. 2005;72:011605.

[179] JP Andreassen, R Beck, M Nergaard. Biomimetic type morphologies of calcium carbonate grown in absence of additives. Faraday Discuss. 2012.

[180] ET Stepkowska, J Perez-Rodriguez, M Sayagues, J Martinez-Blanes. Calcite, vaterite and aragonite forming on cement hydration from liquid and gaseous phase. Journal of thermal analysis and calorimetry. 2003;73:247-69.

[181] PHR Borges, JO Costa, NB Milestone, CJ Lynsdale, RE Streatfield. Carbonation of CH and C–S–H in composite cement pastes containing high amounts of BFS. Cem Concr Res. 2010;40:284-92.

[182] BD Cullity, SR Stock. Elements of X-ray Diffraction Prentice hall Upper Saddle River, NJ; 2001.

[183] S Greenberg, T Chang. The hydration of tricalcium silicate. J Phys Chem. 1965;69:553-61.

[184] M Mollah, W Yu, R Schennach, DL Cocke. A Fourier transform infrared spectroscopic investigation of the early hydration of Portland cement and the influence of sodium lignosulfonate. Cem Concr Res. 2000;30:267-73.

[185] R Panda, M Hsieh, R Chung, T Chin. FTIR, XRD, SEM and solid state NMR investigations of carbonate-containing hydroxyapatite nano-particles synthesized by hydroxide-gel technique. Journal of physics and chemistry of solids. 2003;64:193-9.

[186] E Thian, J Huang, M Vickers, S Best, Z Barber, W Bonfield. Silicon-substituted hydroxyapatite (SiHA): A novel calcium phosphate coating for biomedical applications. J Mater Sci. 2006;41:709-17.

[187] Y Liu, D Hou, G Wang. A simple wet chemical synthesis and characterization of hydroxyapatite nanorods. Mater Chem Phys. 2004;86:69-73.

[188] E Landi, A Tampieri, G Celotti, L Vichi, M Sandri. Influence of synthesis and sintering parameters on the characteristics of carbonate apatite. Biomaterials. 2004;25:1763-70.

[189] S Gunasekaran, G Anbalagan. Spectroscopic characterization of natural calcite minerals. Spectrochimica Acta Part A: Molecular and Biomolecular Spectroscopy. 2007;68:656-64.

[190] M Cao, Y Wang, C Guo, Y Qi, C Hu. Preparation of ultrahigh-aspect-ratio hydroxyapatite nanofibers in reverse micelles under hydrothermal conditions. Langmuir. 2004;20:4784-6.

[191] D Baciu, J Simitzis. Synthesis and characterization of a calcium silicate bioactive glass. Journal of optoelectronics and adavnced materials. 2007;9:3320-4.

Appendices

Appendix I - Variation in fiber distribution and its effect on composite properties

To evaluate fibers distribution in the composite, we analysed by SEM the cut, ground and polished cross-sections of the samples tested in three-point bending (parallel to the loading direction). The difference in the atomic weight of the fibers (mainly carbon) and the matrix (mainly calcium) resulted in good contrast in the SEM back scattered imaging mode. A simplified method to semi-quantify the homogeneity of the fiber distribution was used.

Evaluation of fibers distribution in composite materials is not a simple issue. For example, industry uses fluorescent marking of the fibers, following with specific methods to distinguish the fibers in the composite. Lee et al have used a fluorescent lamp to induce glowing of PVA fibers; subsequently the UV and optical pictures were superimposed on each other and image analysis was used to characterize the fibers content and distribution [A1]. For the purpose of this dissertation, we simplified the calculation by counting the fibers by manually marking them as indicated in the Fig. A1. Fibers, depending to their orientation will have different shapes of their cross sections. We used the middle point of any type of shape as a marker to count the fiber (Fig. A1). This was due to the fact that the image-processing software was not able to distinguish the pores and defects from the fibers. Then, an image processing software was used to translate the specified spots into X-Y scattering and density of the fiber calculations (Fig. A2b).

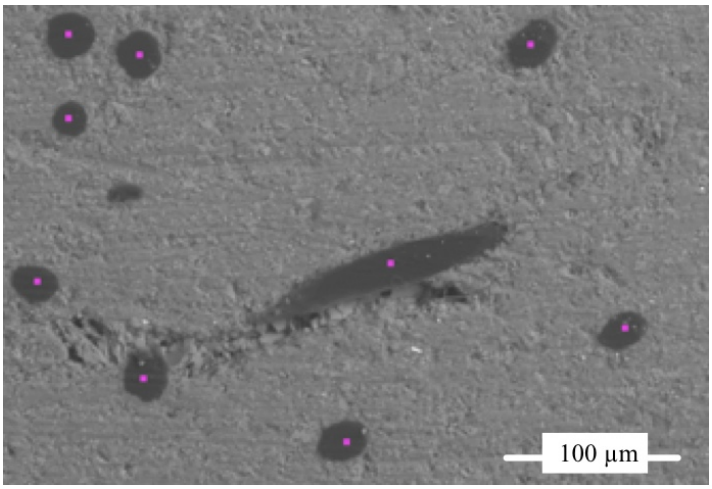

Fig. A1- Typical example of marking of the fibers to be counted.

Even in manual marking at low magnification necessary to cover sufficiently large area of the sample, there was not much contrast difference between the fibers and porosity (e.g. compare the contrast of the fiber in the center of Fig. A1 with that of the pore just below the fiber). Therefore, higher magnification pictures were used to distinguish the fibers from porosity. However, the size of the samples' cross-section compared to the size of the fibres was relatively small in our work. After marking the fibers and drawing the X-Y scatter map of them (Fig. A2c), the micrographs were divided into equal square intervals in both directions. Then, the count of the number of points in each square interval determined the fiber density for each of the squares. If the fiber densities in the squares are similar to the fiber density in the whole picture, it indicates homogenous distribution of the fibers[11]. Standard deviation of the fiber densities of the squares is a good indication of the homogeneity of the distribution of the fibers. The standard deviation of the fiber densities in the square intervals was 5.68 and the average density was 11.0

[11] - This method depends on the magnification, but was chosen as a simple and primary method. We compared same magnification for calculation of the fiber densities for different samples.

fibers per 0.48 mm^2 area. The fiber densities are illustrated in Fig. A2b and the average is shown by the horizontal line

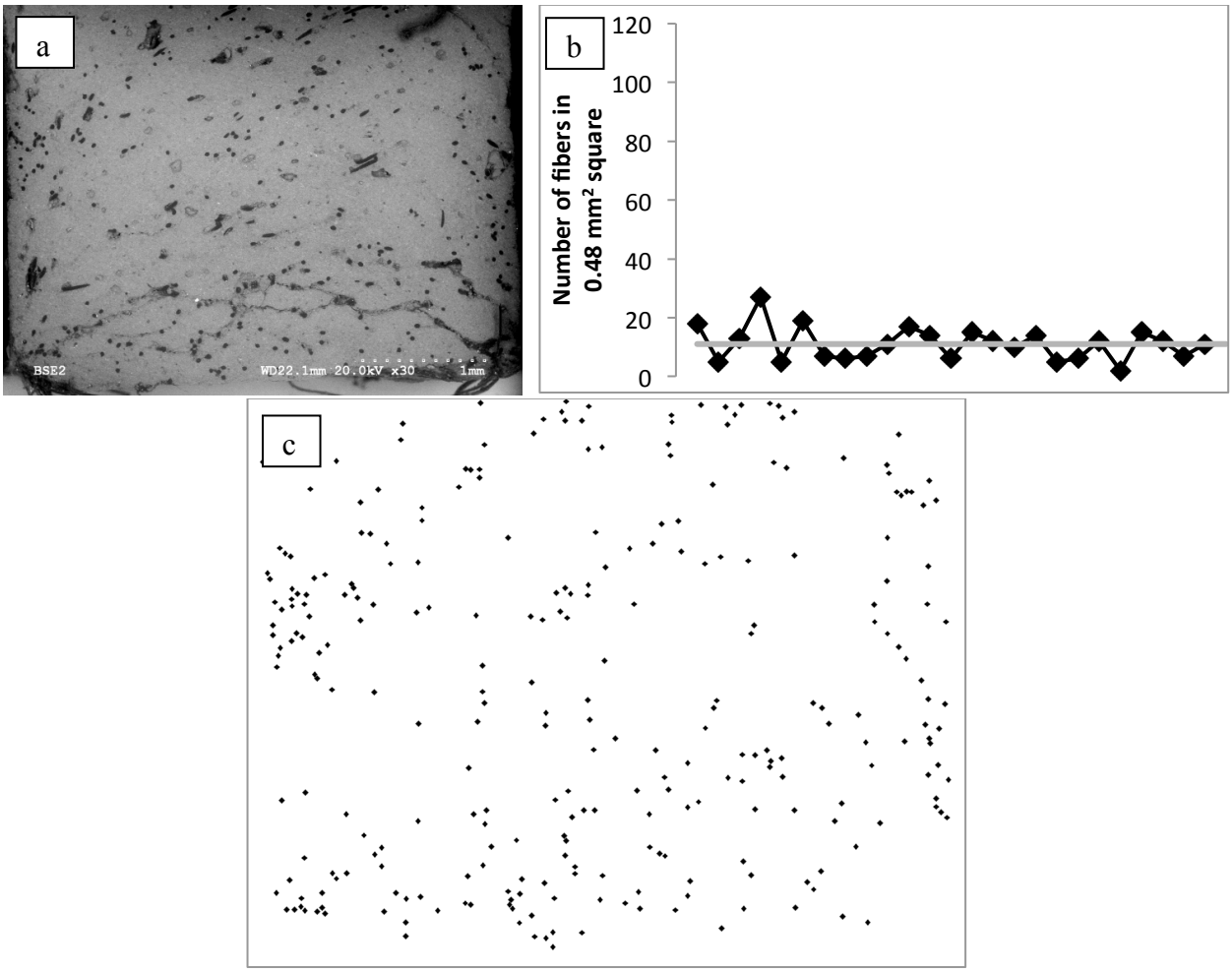

Fig. A2- a) SEM image of the C_3S-PVA fibre composite, prepared with 2.2 wt% of the fibers and PEG solution as liquid phase; b) marking the fibers count; c) marks of the fibers within all the interval subdivision squares; d) number of fibers in each interval square, (average=11.0 per 0.48 mm^2 area and standard deviation=5.68 per 0.48 mm^2).

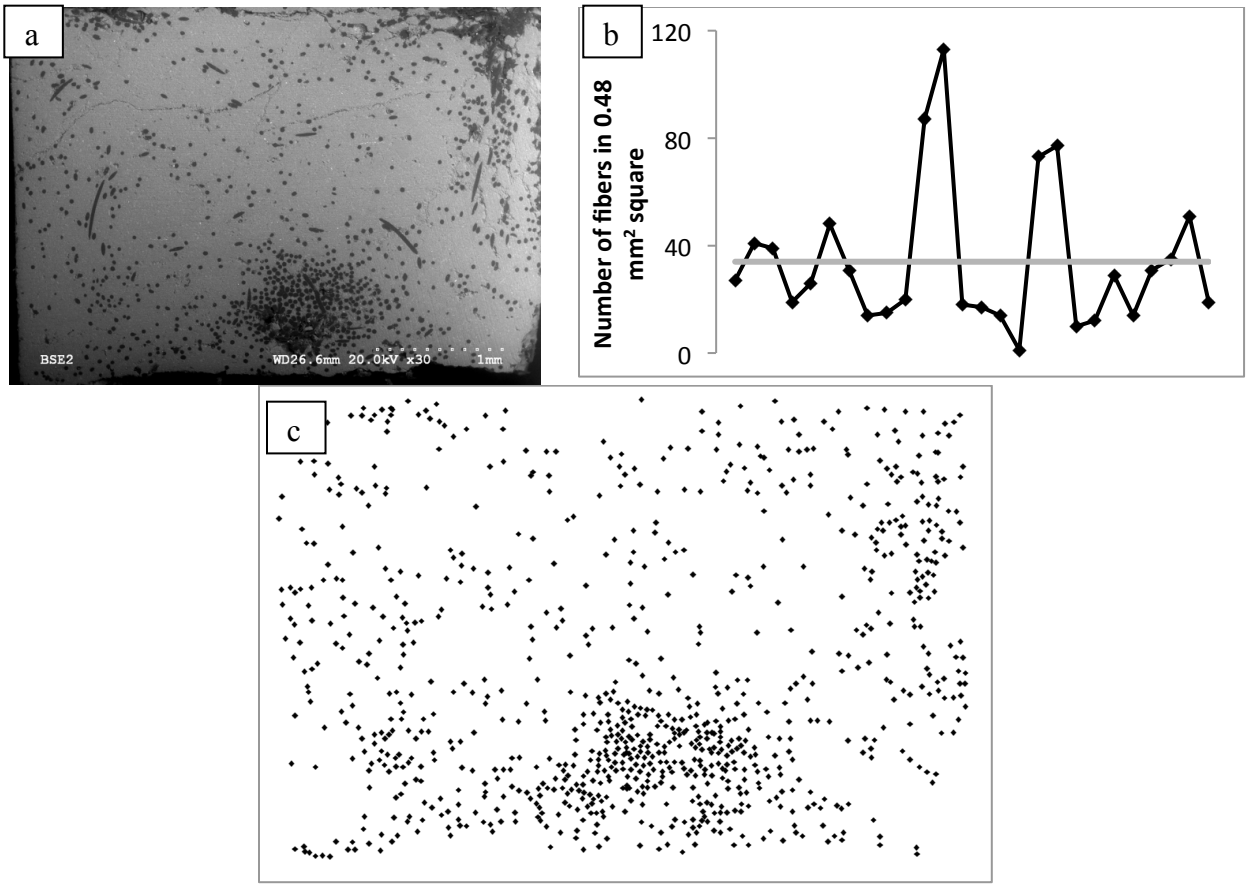

Fig. A3- a) SEM image of the C_3S-PVA fibre composite, prepared with 4 wt% fibers and PEG solution as a liquid phase; b) marks of the fibers within all the interval subdivision squares; c) higher magnification of (a); d) number of fibers in each square (average=35.9 per 0.48 mm^2, standard deviation=26.4 per 0.48 mm^2).

The cross-section of the sample with increased fiber content to 4wt% is shown in Fig. A3a,c. For this material the standard deviation is 26.4 per 0.48 mm^2 (4.6 times higher than standard deviation in Fig. A2b). This analysis shows that mixing 4wt% or higher content of fibers using the small-scale hand-mixing processing method results in rather un-homogeneous distribution of the fibers. For fiber content as high as 6wt% the workability of the paste was reduced dramatically, and it was difficult to fill the moulds with paste.

The non-homogeneous fiber distribution resulted in wide range of variation in three point bend test results. The representative load-displacement curves of seven identically prepared C_3S-4wt% PVA composite samples are shown in Fig. A4. The maximum load-bearing capacity of the seven identically prepared samples (set for 10 days in distilled water at 37°C), range between 13-43 N, with average of 28.5 N, and standard deviation of 12.2 N (where for the C_3S-2.2wt%PVA, the average = 25.6 N and standard deviation = 2.00). Therefore, C_3S-2.2wt%PVA composite was chosen for the self-healing experiments.

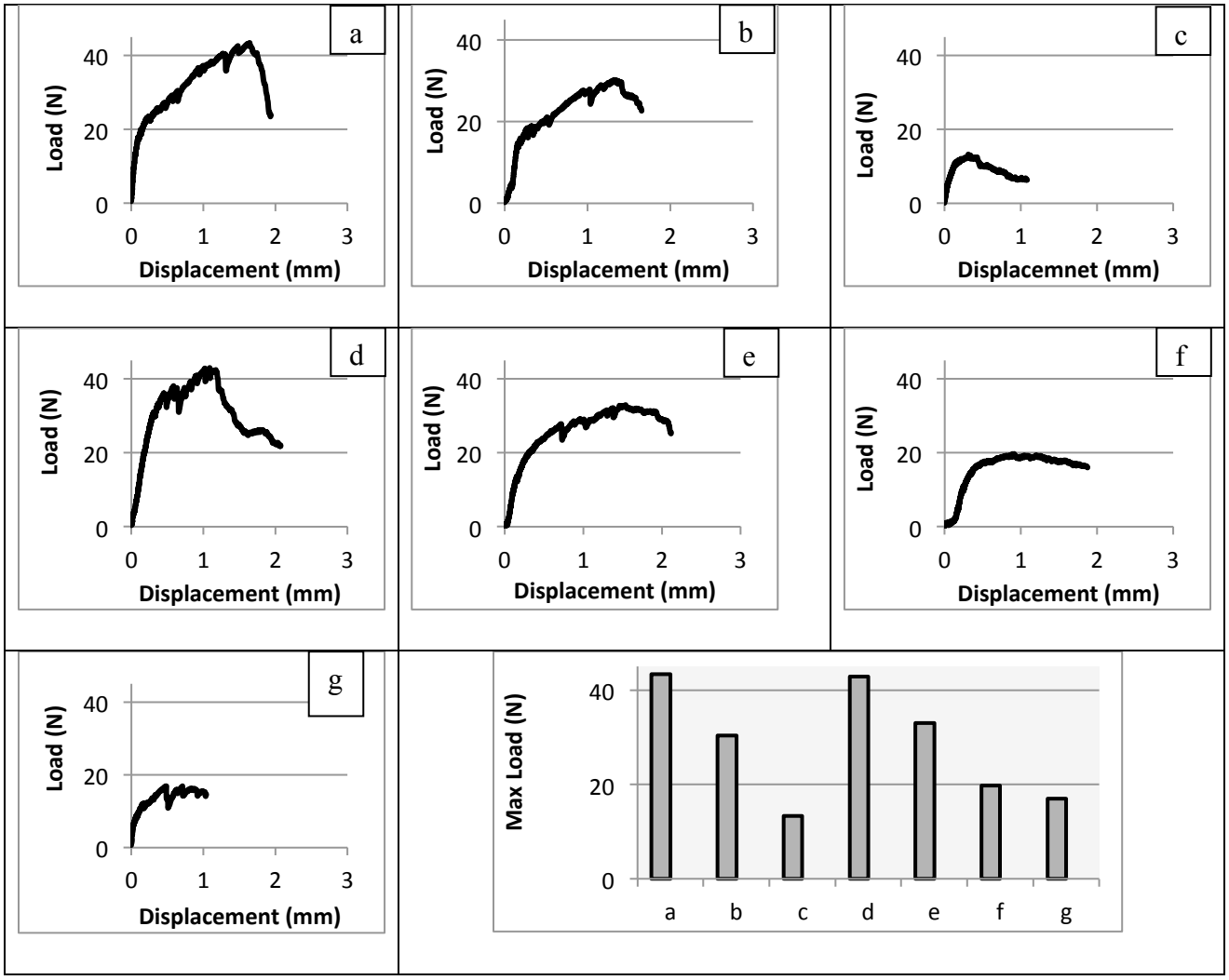

Fig. A4- Load-displacement curves of seven identically prepared C_3S-4wt%PVA samples

Appendix II- Ionic dissociation coefficients for H_3PO_4 and H_2CO_3

In this appendix the method to calculate the ionic dissociation coefficients (α) and variations of the α values versus pH graph are presented for i) H_3PO_4 and ii) H_2CO_3.

i) Phosphoric acid

Phosphoric acid is a triprotic acid and is able to donate three protons in aqueous system. Therefore, the available specie can vary with the system parameters, especially with pH. To calculate the ionic dissociation coefficients in a specific pH, first we should write down the proton production reactions for H_3PO_4:

$H_3PO_{4(s)} + H_2O_{(l)} \rightarrow H_3O^+_{(aq)} + H_2PO_4^-{}_{(aq)}$ $K\alpha_1 = 7.25\times10^{-3}$ Equation A1

$H_2PO_4^-{}_{(aq)} + H_2O_{(l)} \rightarrow H_3O^+_{(aq)} + HPO_4^{2-}{}_{(aq)}$ $K\alpha_2 = 6.31\times10^{-8}$ Equation A2

$HPO_4^{2-}{}_{(aq)} + H_2O_{(l)} \rightarrow H_3O^+_{(aq)} + PO_4^{3-}{}_{(aq)}$ $K\alpha_3 = 4.80\times10^{-13}$ Equation A3

$$\alpha_0 = \frac{[H_3O^+]^3}{[H_3O^+]^3+K_{\alpha1}[H_3O^+]^2+K_{\alpha1}K_{\alpha2}[H_3O^+]+K_{\alpha1}K_{\alpha2}K_{\alpha3}}$$ Equation A4 [A2]

$$\alpha_1 = \frac{K_{\alpha1}[H_3O^+]^2}{[H_3O^+]^3+K_{\alpha1}[H_3O^+]^2+K_{\alpha1}K_{\alpha2}[H_3O^+]+K_{\alpha1}K_{\alpha2}K_{\alpha3}}$$ Equation A5 [A2]

$$\alpha_2 = \frac{K_{\alpha1}K_{\alpha2}[H_3O^+]}{[H_3O^+]^3+K_{\alpha1}[H_3O^+]^2+K_{\alpha1}K_{\alpha2}[H_3O^+]+K_{\alpha1}K_{\alpha2}K_{\alpha3}}$$ Equation A6 [A2]

$$\alpha_3 = \frac{K_{\alpha1}K_{\alpha2}K_{\alpha3}}{[H_3O^+]^3+K_{\alpha1}[H_3O^+]^2+K_{\alpha1}K_{\alpha2}[H_3O^+]+K_{\alpha1}K_{\alpha2}K_{\alpha3}}$$ Equation A7 [A2]

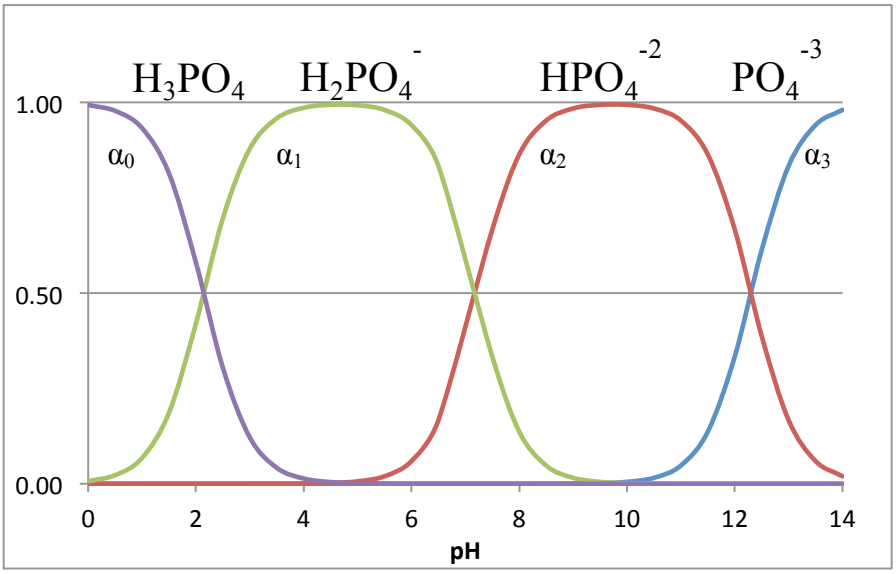

Fig. A5- Ionic dissociation coefficients for H_3PO_4 versus pH.

The α_i for each of the species can be calculated using $K\alpha_{1,2,3}$ and the $[H_3O^+]=10^{-pH}$. Substituting the $K\alpha_{1,2,3}$ from the Equations A1-A3 into the Equations A4-A7, the α_i graph can be illustrated versus pH variations [A2, A3], as shown in Fig. A5. At any given pH, the percentage of the availability of species can be calculated in aqueous solution. As an example, at pH=9.2 the dominant specie is HPO_4^{2-} and $\alpha_2=0.989$ and $\alpha_3=7.84\text{x}10^{-4}$, indicating small amount of PO_4^{3-} is available in such pH. However, if other ions would be available in the system, they can affect these reactions and consequently the α_i values and stability of the ions (more info in the summary).

ii) Carbonic acid

Carbonic acid is a diprotic acid, which can donate two protons into the aqueous system. Similar to phosphoric acid, the α_i for each of the species can be calculated using $K\alpha_{1,2}$ and the $[H_3O^+]=10^{-pH}$ by substituting $K\alpha_{1,2}$ values from Equation A8 and A9 into the Equations A10-12. Fig. A6 shows the variations of α_i versus pH. The α_i can be calculated for any specified pH, such as pH=9.2, in which the dominant specie is HCO_3^- and $\alpha_1=0.930$ and $\alpha_2=0.069$, indicating small amount of CO_3^{-2} is available.

$H_2CO_{3(s)} + H_2O_{(l)} \rightarrow H_3O^+_{(aq)} + HCO_3^-{}_{(aq)}$ $K\alpha_1= 4.45\text{x}10^{-7}$ Equation A8

$HCO_3^-{}_{(aq)} + H_2O_{(l)} \rightarrow H_3O^+_{(aq)} + CO_3^{2-}{}_{(aq)}$ $K\alpha_2= 4.69\text{x}10^{-11}$ Equation A9

$$\alpha_2 = \frac{K_{\alpha1}K_{\alpha2}}{[H_3O^+]^2+K_{\alpha1}[H_3O^+]+K_{\alpha1}K_{\alpha2}}$$ Equation A10 [A3]

$$\alpha_1 = \frac{K_{\alpha1}[H_3O^+]}{[H_3O^+]^2+K_{\alpha1}[H_3O^+]+K_{\alpha1}K_{\alpha2}}$$ Equation A11 [A3]

$$\alpha_0 = \frac{[H_3O^+]^2}{[H_3O^+]^2+K_{\alpha1}[H_3O^+]+K_{\alpha1}K_{\alpha2}}$$ Equation A12 [A3]

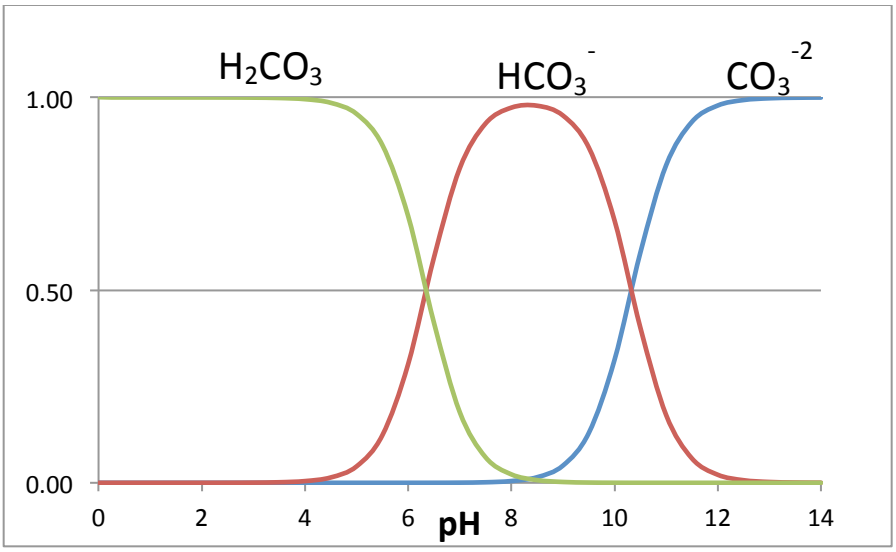

Fig. A6- Ionic dissociation coefficients for H_2CO_3 versus pH.

The above calculations and graphs could be used for predicting the availability of the different species in the system presented in this dissertation. However, the calculations were based on the $K\alpha_{i,}$ values. These values are valid in a system without presence of any other ions than the reaction products of that specific acid. Previously graphs such as Fig. A5 were used to explain precipitation of hydroxyapatite [A4]. However, availability of other cations and/or anions in the system will have a direct effect on the reactions and consequently on the α_i. Ions are electrically charged and thus interact electrostatically according to Coulomb's law. However, based on Debye–Hu¨ckel theory, since the ions are free to move in an electrolyte, they rearrange to lower the system energy forming a double layer reducing the Coulomb interaction force of that ion [A5, A6].

Considering the fact that our system consists of many other ions available in the SBF, addition of C_3S and its hydration products invalidates thermodynamic calculations with the current α_i values. For less complicated system, Lu and Leng [A7] have calculated both

theoretical thermodynamic data as well as kinetic factors to determine the Gibbs free energy of different calcium phosphate phases [A7], as there are intermediate phases forming prior to HAp precipitation. They also have mentioned that "*the theoretical analysis of Ca-P precipitation in SBF is understandably scarce because of the complexity of its chemical composition*" [A7]. Therefore, if thermodynamic calculations in a system similar to the system available in this dissertation would be of interest, it requires many extra considerations and precise measurements of the concentrations of the ions, available phases and interaction parameters.

Other complications of the above approach include:

i) Phosphate sorption by calcium carbonate;

ii) Carbonation of the calcium phosphates;

iii) Si substitution in calcium phosphates structure;

iv) P substitution in calcium silicate structure;

v) Presence of Cl^- and Na^+ ions affect the C-S-H gel structure and further hydration of the C_3S (Cl^- is an accelerator for C_3S setting).

vi) The further thermodynamic studies for such system are valid only when the equilibrium criteria are met and the exact available phases are determined. As C_3S hydration progresses over rather long time (> 1 year), therefore in less than 28 days the system cannot reach equilibrium (one vivid sign of this is the continued pH variations over time).

In summary, the thermodynamic calculations for the presented system should ideally cover the Debye–Hu¨ckel constant calculations, measuring equilibrium concentrations and nominal concentrations of each and every ion available, determining the ionic strength, as well as

kinetic considerations. As a result, such calculations and measurements are beyond the scope of this dissertation.

Appendices references:

[A1] Bang Yeon Lee, Jin-Keun Kim, Jeong-Su Kim, Yun Yong Kim, "Quantitative evaluation technique of Polyvinyl Alcohol (PVA) fiber dispersion in engineered cementitious composites", Cement and Concrete Composites, 2009, P 408–417.

[A2] http://ion.chem.usu.edu/~sbialkow/Classes/3600/alpha/alpha3.html (access date: 15/05/2013)

[A3] http://ion.chem.usu.edu/~sbialkow/Classes/3600/alpha/alpha2.html (access date: 15/05/2013)

[A4] Tanahashi, M., Kamiya, K., Suzuki, T., & Nasu, H. (1992). Fibrous hydroxyapatite grown in the gel system: effects of pH of the solution on the growth rate and morphology. Journal of materials science: Materials in medicine, 3(1), 48-53.

[A5] http://www-scf.usc.edu/~chem430a/scans/08.pdf, ©2009 C. H. Mak (aces date: 10/06/2013)

[A6] Pitzer, K. S. (1991). Activity coefficients in electrolyte solutions. CRC press.

[A7] Lu, X., & Leng, Y. (2005). Theoretical analysis of calcium phosphate precipitation in simulated body fluid. Biomaterials, 26(10), 1097-1108.